HOKKAIDO UNIVERSITY

Title	Spectroscopic investigations of photothermal and photochemical activities of electron donor-acceptor molecular dyads
Author(s)	Sasikumar, Devika
Degree Grantor	北海道大学
Degree Name	博士(環境科学)
Dissertation Number	甲第13897号
Issue Date	2020-03-25
DOI	https://doi.org/10.14943/doctoral.k13897
Doc URL	https://hdl.handle.net/2115/94515
Type	doctoral thesis
File Information	Sasikumar_Devika.pdf

Hokkaido University Collection of Scholarly and Academic Papers : HUSCAP

学 位 論 文

Spectroscopic investigations of photothermal and photochemical activities of electron donor-acceptor molecular dyads

（電子ドナー・アクセプター連結分子による光熱変換および光化学反応についての分光学的研究）

Graduate School of Environmental Science
Hokkaido University

Sasikumar Devika

March 2020

Acknowledgement

I express my sincere gratitude to my supervisor Prof. Vasudevan Pillai Biju, for the guidance and support throughout my research work. I learned how to accomplish research without exhaustion or despair and with incredible enthusiasm. I would like to thank Prof. Yuta Takano for guiding me and teaching me the basic laboratory chores. He taught me to be kind and optimistic, even in extreme circumstances. Without his support, I couldn't have achieved this goal. I thank Prof. Ken-ichi Yuyama for technical support and suggestions. He encouraged and motivated me throughout my research. I express my appreciation and thanks to the members of my laboratory for the inspirations and moral support, especially I thank Lata, and Bhagya, and Reiko Kohara. I would like to convey my gratitude to Mrs. Atsuko Fujii for helping me handling documents and official formalities. I thank Prof. Yasuhiro Kobori and Dr. Morihiko Hamada of Kobe University for providing me with the facility for electron paramagnetic resonance spectroscopic studies. I thank Prof. Hiroshi Imahori of Kyoto University and Prof. Akihiro Furube of Tokushima University for their generous support with transient absorption spectroscopic studies. I thank Nikon Imaging Center for the facilities provided to me for cell imaging. I acknowledge the financial assistance under the English Program of Environmental Earth Science for Sustainable Society program and the Japan Student Services Organization. I am thankful for the ineffable support and encouragement provided to me by my family. I thank my sister Deepika Sasikumar for inspiring me always. I thank my mother Sandhyadevi, and my father Sasikumar for motivating me to dream high.

Abstract

This thesis emphasizes on the regulation and control of photochemical and photothermal functions of simple electron Donor-Acceptor (D-A) molecular dyads. Electron transfer is one of the extensively investigated phenomena in basic science, which is by considering its vital role in natural and artificial photosynthesis. Despite, several complex electron transfer systems developed for light-harvesting by mimicking the natural photoinduced electron transfer process, simple electron transfer systems are continuously sought after for improving the efficiency of solar energy harvesting and developing molecular sensors. In this work, I design and synthesize two classes of novel electron D-A dyads; one for the efficient photothermal energy conversion, and the other for the efficient sensing of singlet oxygen ($^1O_2$) in the homogenous solution phase and in the cell microenvironment.

This thesis consists of five chapters, including the introduction to photoinduced electron transfer (chapter 1), where I summarise photoinduced electron transfer occurring in natural photosynthesis and its efficient mimicking toward the construction of various artificial solar energy harvesting systems. In the introduction chapter, I explain the classical theories of electron transfer in the designing of simple D-A dyads with efficient intramolecular electron transfer. In chapter 2, I discuss the synthesis of novel D-A systems, methods of characterization of D-A systems, and spectroscopic methods employed in the investigation of electron transfer and photothermal and sensing studies.

In chapter 3, I demonstrate the upgraded photothermal energy conversion by acridinium-based D-A dyads. Even though the conventional photothermal agents offer high energy conversion efficiency, most of them have narrow absorption bands. Therefore, broad band solar energy absorbing molecules and materials are continuously sought after. The general approach for the extension of light absorption by molecules to the entire UV-Visible-Near Infrared (UV-Vis-NIR) region is to extend the π-conjugation, which is tedious and time consuming. Thus, in this chapter, I employ a novel acridinium-based D-A dyad with highly-efficient electron transfer. The UV to blue absorbing dyad undergoes photoinduced electron transfer, followed by excited-state deprotonation to generate its betaine form. The betaine shows appreciably long half-life and extended absorption in the UV-Vis-NIR region. The photothermal energy conversion efficiency of

the dyad under blue light excitation is enhanced by illumination with long wavelength light. The dyad shows excellent photostability, making the dyad-betaine combination promising for photothermal energy conversion applications.

In chapter 4, I demonstrate the applications and principles of D-A systems to the sensing of $^1O_2$. Reactive oxygen species offer positive and negative impacts on our life-routine, among which $^1O_2$ attracts considerable attention owing to its significance to various chemical, biological, and biochemical processes. Therefore, the sensitive and efficient detection of $^1O_2$ is relevant in our daily life. The conventional fluorescence sensors of $^1O_2$ are anthracene-based electron D-A systems to which many fluorogenic sensors based on substituted anthracene are reported. However, the roles of substituents on the sensing efficiency remain largely unknown. Therefore, in chapter 4, I investigate the substituent effects on the $^1O_2$ sensing efficiency, which is with the intention to improve the efficiency and speed of $^1O_2$ detection. Here, I examine the rate of $^1O_2$ sensing by three anthracene-based electron D-A dyads, aminocoumarin-anthracene conjugates (**S1** and **S2**), a rhodamine-anthracene conjugate (**S3**) and a model compound. The second-order rate of reaction of the sensors with $^1O_2$ is an order of magnitude less than 9-methylanthracene. The reduced reactivity of **S1** suggests the role of the substituent on the rate of sensing.

During $^1O_2$ sensing studies involving **S1** as the sensor, I found an anomalous increase in the fluorescence intensity of **S1** under the illumination with UV light, which is after co-sensitization with a porphyrin molecule or Rose Bengal. This abrupt and colossal enhancement of fluorescence intensity suggests the formation of an intermediate complex which is UV-active. The intermediate complex shows stability against $^1O_2$ scavengers. To verify the existence of the intermediate complex between **S1** and $^1O_2$, I employ electron paramagnetic resonance spectroscopy (EPR) and nuclear magnetic resonance spectroscopy (NMR) and rationalize the crucial role of coumarin to form the complex. The steady-state absorption, fluorescence, EPR, and NMR studies suggest that the reaction of $^1O_2$ to **S1** leads to the trapping of $^1O_2$ inside **S1**. The UV stimulation activates the intermediate complex to form the endoperoxide efficiently and swiftly. Finally, I test the potentials of the sensors to detect the intracellular $^1O_2$ by cell imaging.

Table of Contents

Chapter 1. Introduction

1.1 Photoinduced electron transfer in natural photosynthesis 1

1.2 Significance of PET in artificial photosynthesis 2

1.3 Electron transfer dynamics dye sensitized solar cell 3

1.4 Theory of electron transfer 5

1.5 PET in fluorescence sensors 10

1.5.1 PET-based sensors of reactive oxygen species 12

1.6 The motivation and objectives of this research 16

References 18

Chapter 2. Experiments

Abstract 24

2.1 Materials 25

2.1.1 Dyads for photothermal energy conversion

2.1.2 Synthesis of 9-(2,6-dimethyl-4-hydroxyphenyl)-10-methylacridinium chloride (**Acr1**) 26

2.1.3 Preparation of 9-mesityl-10-methylacridinium chloride (**Acr2**) 29

2.1.4 Electron D-A-based fluorescence sensors of singlet oxygen 30

2.1.5 Synthesis of singlet oxygen sensors 32

2.1.5.1 Synthesis of 7-[9-(methylanthryl)amino]-4-methyl-chromen-2-one (**S1**) 32

2.1.5.2 Synthesis of 7-[9-(methylanthryl)(ethyl)amino]-4-methyl-chromen-2-one (**S2**) 33

2.1.5.3 Synthesis of 6-[9-(methylanthryl)(ethyl)amino)-9-(2-(ethoxycarbonyl)phenyl)-2,7-dimethyl-xanthen-3-ylidene)ethanaminium chloride (**S3**) 34

2.2 Methods 35

2.2.1 Nuclear magnetic resonance spectroscopy 35

2.2.2 Electrospray ionization mass spectroscopy 35

2.2.3 Fourier-transform infrared spectroscopy 36

2.2.4 Cyclic voltammetry 36

2.2.5 Density functional theory calculations 38
2.2.6 Steady-state absorption spectroscopy 38
2.2.7 Transient absorption spectroscopy 39
2.2.8 Steady-State fluorescence spectroscopy 41
2.2.9 Electron paramagnetic resonance spectroscopy 43
2.3 Optical set-up for photothermal studies. 45
References 46

Chapter 3. Intramolecular Electron Transfer for Photothermal Energy Conversion

Abstract 49
3.1 Introduction 49
3.1.1 Photothermal energy conversion in photothermal therapy 50
3.1.2 Photothermal energy conversion in light harvesting 51
3.2 Design and fundamental properties of electron donor-acceptor dyads 52
3.2.1 Density functional theory calculations 53
3.2.2 Cyclic voltammetry studies 55
3.2.3 Steady-state absorption and fluorescence studies 58
3.2.4 Determination of the efficiency of electron transfer 60
3.2.5 Determination of pKa of **Acr1** 60
3.3 Transient absorption studies 61
3.4 pH-Dependent photothermal effect by dual photoexcitation 64
3.5. Calculation of photothermal conversion efficiency of **Acr1** 67
3.6. The effect of the excitation power of the blue light on the photothermal effect of **Acr1** 69
3.7 pH-Dependent photostability studies 70
3.8 The mechanism of pH-dependent photothermal effect and dual photoexcitation induced enhanced thermal response 72
3.9 Conclusions 74
References 75

Chapter 4. Intramolecular Electron Transfer for Singlet Oxygen Sensing

Abstract 78

4.1. Introduction 78

4.1.1 Reactive oxygen species 78

4.1.2 Singlet oxygen ($^1O_2$) 79

4.1.3 Singlet oxygen sensitization 81

4.1.4 The significance of singlet oxygen 83

4.1.5 Singlet oxygen sensing 84

4.1.5.1 Phosphorescence detection 84

4.1.5.2 Electron paramagnetic detection 84

4.1.5.3 Fluorescence detection 85

4.2 Design and ground-state electronic interaction studies of sensors 87

4.3 Kinetics of singlet oxygen sensing using 9-substituted anthracene derivatives 89

4.3.1 Singlet oxygen sensing using **S1** 89

4.3.1.2 Mechanism of singlet oxygen mediated photooxidation of **S1** 91

4.3.1.3 Kinetics of singlet oxygen sensing by **S1** 93

4.3.2 Kinetics of singlet oxygen mediated oxidation of **A1** 94

4.3.3 Kinetics of singlet oxygen sensing by **S2** 96

4.3.4 Kinetics of singlet oxygen sensing by **S3** 98

4.4 Conclusions 99

References 100

Chapter 5. Mechanism of Singlet Oxygen Reaction

Abstract 104

5.1 Introduction 105

5.2 UV-induced fluorescence enhancement during singlet oxygen sensing 106

5.3 The effect of singlet oxygen scavenger on UV-induced fluorescence enhancement 108

5.4 The stability of the intermediate complex 110

5.5.1 The role of substituent on the UV-induced fluorescence enhancement 111
5.5.2 Examination of UV effect on Rhodamine 6G-anthracene conjugate 112
5.6 EPR studies of UV activated reaction of singlet oxygen and **S1** 113
5.7 NMR studies of the UV-activated reaction of **S1** 119
5.8 The possible mechanism of UV-activated reaction of **S1** with singlet oxygen 122
5.9 The application of singlet oxygen sensors 125
5.10 Conclusions 127
References 128
Summary and perspectives 131

List of publications 133
List of presentations 134

List of abbreviations

A	
Acr1	9-(2,6-dimethyl-4-hydroxyphenyl)-10-methylacridinium chloride
Acr1-betaine	Deprotonated form of Acr1
Acr2	9-mesityl-10-methylacridinium chloride
Acr2-CS	Charge separated state of Acr2
Acr3	10-methylacridinium perchlorate
ASG	Arhus sensor green
B	
BODIPY	Boron-dipyrromethene
bpy	Bipyridine
C	
CS	Charge separated
CT	Charge transfer
CV	Cyclic voltammetry
D	
D-A	Donor-acceptor
DCM	Dichloromethane
DFT	Density functional theory
DMF	*N,N*-Dimethylformamide
DNA	Deoxyribonucleic acid
DPAX	(9-[2-(3-carboxy-9,10-diphenyl)anthryl]-6-hydroxy-3H-xanthen-3-one)
DPIBF	1,3-diphenylisobenzofuran
DPV	Differential pulse voltammetry
DSSC	Dye sensitized solar cell
E	
EPR	Electron paramagnetic resonance
ESI-MS	Electrospray ionization-mass spectroscopy
F	
Fc/Fc^+	Ferrocene/ferrocenium couple
FNR	Ferredoxin-NADP reductase
FTIR	Fourier-transform infrared spectroscopy
H	
HBSS	Hank's balanced salt solution
HOMO	Highest occupied molecular orbital

L

LED	Light emitting diode
LSPR	Localized surface plasmon resonance
LUMO	Lowest occupied molecular orbital

M

MNPs	Metal nanoparticles

N

NADP	Nicotinamide adenine dinucleotide phosphate
NMR	Nuclear magnetic resonance

P

PCy	Plastocyanin
PDT	Photodynamic therapy
PET	Photoinduced electron transfer
PpXI	Protoporphyrin
PS	Photosensitizer
PSI	Photosystem I
PSII	Photosystem II
PTE	Photothermal effect
PTT	Photothermal therapy

R

RB	Rose Bengal
ROS	Reactive oxygen species

S

S1	Sensor 1 (aminocoumarin-anthracene conjugate)
S2	Sensor 2 (*N*-alkylated aminocoumarin-anthracene conjugate)
S3	Sensor 3 (Rhodamine 6G-anthracene conjugate)
Si-DMA	Silicon-contain Rhodamine-anthracene conjugate
SOSG	Singlet oxygen sensor green

T

TA	Transient absorption
TCPP	Tetrakis (4-carboxyphenyl) porphyrin
TEMP	2,2,6,6-tetramethylpiperidine
TEMPO	2,2,6,6-tetramethylpiperidine-1-oxyl
THF	Tetrahydrofuran
TiE	Nikon inverted microscope

U

UV	Ultraviolet

Chapter 1

Introduction

Light is inevitable for subsistence of life on the planet earth. Thus, light-induced chemical reactions (photochemical reactions) always gained the attention of scientists.[1] Photoinduced electron transfer (PET) attract significant attention in the field of photochemical reactions.[2] PET has been largely explored for solar energy harvesting applications. Natural photosynthetic reaction center is the best example for understanding the fundamental principles of PET.[3] The structure of natural photosynthetic reaction center, and the thermodynamics and the kinetics of natural electron transfer are the basis of artificial photosynthesis including solar cells.[4]

1.1 Photoinduced electron transfer in natural photosynthesis

The natural photosynthesis occurring in the chloroplast thylakoid membrane converts light energy into chemical energy. The photosynthetic process proceeds through a series of photochemical reactions as shown in Figure 1.1.[5]

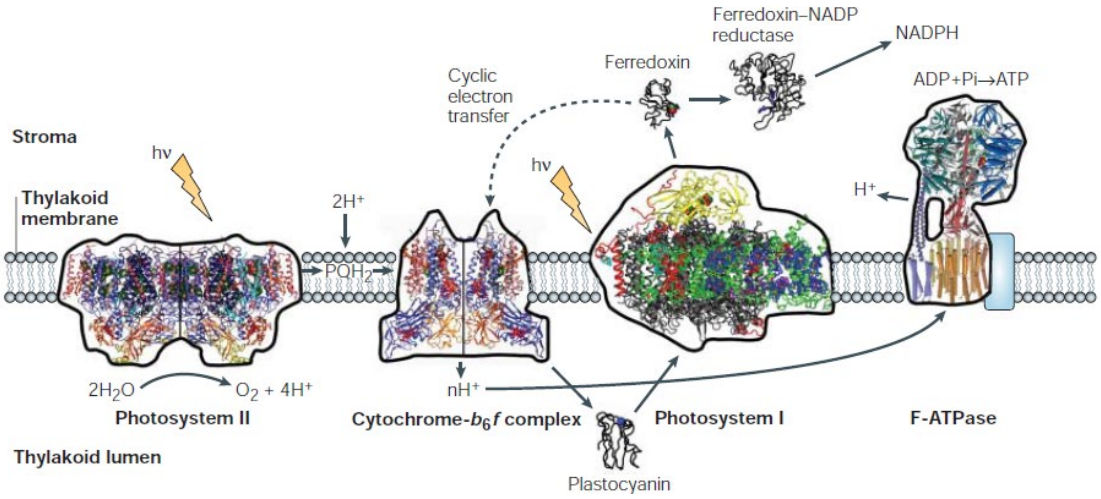

Figure 1.1. A schematic representation of the distribution of photosynthetic reaction centers in the thylakoid membranes of chloroplasts. Reprinted from Ref 5.

The thylakoid membranes of chloroplasts consist two reaction centers, Photosystem I (PSI) and Photosystem II (PSII), both constitutes complex proteins and cofactors. The photosynthesis starts with absorption of light by the reaction center core

of PSII, P680 (Chlorophyll) and leads to translocation of the electron across thylakoid membrane through cofactors to the final electron acceptor, plastocyanin (PC). The redox potential of $P680^{\cdot+}$ is high enough to drive the oxidation of water, and electrons are transferred from water to the oxidized $P680^{\cdot+}$. In PSII, a light driven abstraction of 4 electrons from 2 water molecules is facilitated by P680 and releases 4 protons and an oxygen molecule. The low energy electrons in the terminal acceptor of PSII is boosted by the photoexcitation of the reaction center core in PSI, P700 and then sequential electron transfer occurs and finally, the electron is transferred to ferredoxin-NADP reductase (FNR) to reduce nicotinamide adenine dinucleotide phosphate ($NADP^+$) to NADPH. The electrochemical transmembrane potential generated due to the establishment of charge separated state creates a proton concentration difference across thylakoid membrane and ATP synthase takes advantage of the proton gradient for synthesis of adenosine triphosphate (ATP). Thus, two energetically enriched molecules (NADPH and ATP) are produced in photosynthesis. PSI and PSII functions with a high quantum yield of 1.0 and 0.85 respectively.[3,5-9]

1.2 Significance of PET in artificial photosynthesis

Based on the structure and the principles of natural electron transfer systems, scientists developed various electron donor-acceptor (D-A) molecules. A significant effort has been made to mimic the natural leaf to create an artificial leaf since the demand for alternative to fossil fuels is growingly indispensable. However, making an efficient biomimetic system has been highly challenging. The natural photosynthesis is accomplished through several complicated steps involving vast number of giant biomolecules such as proteins. Thus, only minimal number of artificial systems are known to efficiently mimic the natural leaf to simultaneously establish oxygen evolution and hydrogen evolution. The selection of the photosensitizer is based on the superior properties such as strong absorption of the light in the visible region, long-living excited state and high photostability along with high oxidation potential. One of the most distinguished candidates is Ruthenium complexes, for example, $[Ru(bpy)_3]^{2+}$. A sacrificial electron acceptor (SEA) is used to replace the electron acceptor in natural photosynthesis ($NADP^+$). The photoexcitation of $[Ru(bpy)_3]^{2+}$ generates the excited state species $[Ru(bpy)_3]^{2+*}$, which can efficiently transfer electron to SEA such as $[Co(NH_3)_5]^{2+}$. The

oxidized form of the complex drives the oxidation of water.[4,7,10,11] Covalently linked electron D-A molecules constitute a class of artificial electron transfer systems. Among these, porphyrin-based covalently-linked systems attracted much attention owing to the strong absorption of visible light, rational redox potential, and the long-living excited state. Fullerenes are versatile electron acceptors due to their small reorganization energy, rigid geometry and the ability to stabilize in the reduced state with one or more electrons. The porphyrin-fullerene combination has been widely applied in artificial photosynthesis to create a long-living charge-separated (CS) state. However, the synthesis of complex supramolecular systems to facilitate multistep electron transfer is time consuming. Thus, significant effort has been employed to develop simple electron D-A dyads. The rational design of simple D-A dyads by controlling the redox potentials, geometry, D to A distance helped to achieve long-lived CS state. [4,7] 9-position substituted acridinium ions are typical examples.[12] The efficient electron transfer in acridinium-based systems motivated me to design a new D-A dyad and explore its photothermal applications.

1.3 Electron transfer dynamics dye sensitized solar cell (DSSC)

Photovoltaic devices have been developed for the efficient harvesting of sunlight by converting the light energy to electrical energy. Silicon-based solar cell constitutes the forefront spectrum of commercial solar panels. New photovoltaic devices have been emerged with the exploitation of cost-effective materials such as dyes, organic polymers, inorganic materials, quantum dots, and perovskites.[13-21] DSSC has been evolved as a potential alternative to Si-based solar cells. One form of DSSC made from such molecules or nanomaterials is a photoelectrochemical solar cell. The main component of such DSSC is the photosensitizer, which extracts the photons from the sunlight. Therefore, a significant amount of effort has been dedicated to improve the light harvesting efficiency by the broadening of the absorption spectra and improving the efficiency of electron transfer. The conventional sensitizers comprise ruthenium-based complexes, porphyrin, diketopyrrolopyrrole, and borondipyrromethene (BODIPY) derivatives.

The basic configuration of a photoelectrochemical DSSC setup comprises a photosensitizer adsorbed on the semiconductor titanium dioxide (TiO_2) nanoparticles and an iodide/triiodide redox electrolyte. The working of DSSC starts with the absorption of

photons by the photosensitizer dye and followed by initial CS. The charge is stabilized by a fast injection of an electron to the conduction band of TiO_2. The dye is regenerated by the receiving electron from iodide.[21] The kinetics of DSSC function is represented in Figure 1.2. The efficiency of the device is largely governed by the electron transfer dynamics in the two CS. One is the injection of the electron from excited dye to the metal oxide electrode, and the other is the regeneration of dye by the redox electrolyte.[21,25] It is important to control the undesired decay of the excited state dye and charge recombination of the injected electron. Thus, efficient metal free organic D-A dyes have been developed with long lifetime and lower optical band gap along with sufficient electronic coupling between the lowest unoccupied molecular orbital (LUMO) of the dye and the electron accepting energy levels of TiO_2.[21,25,26]

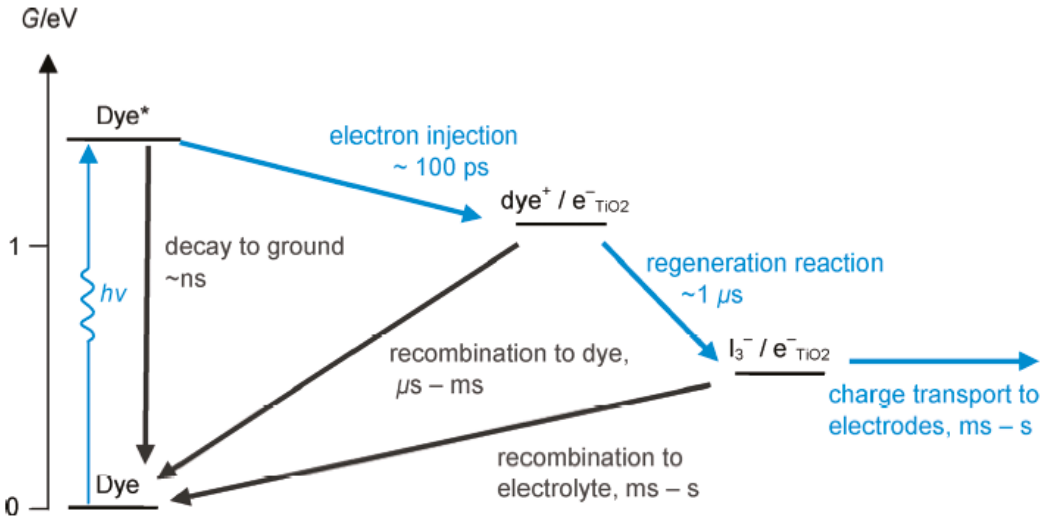

Figure 1.2. A diagram of electron transfer dynamics in a DSSC. Reprinted from Ref 21.

1.4 Theory of electron transfer

In this work, PET is used as a regulating factor for tuning the photothermal and fluorescence properties of D-A systems. In the course of the construction of novel electron D-A systems, it is essential to predict the free energy change of electron transfer to verify the thermodynamic feasibility of electron transfer. There are several factors that affect the efficiency of electron transfer needed to be considered while designing electron D-A systems. To this purpose, adequate knowledge in fundamental electron transfer theories is essential. PET exhibits higher efficiency compared to electron transfer reactions occurring in the dark since, the redox potential of the excited state species are different from ground-state. The electron transfer process leads to the formation of radical ion pair (Figure 1.3 A). A molecule can act as a better oxidant or reductant in the photoexcited state due to the higher electron affinity and lower ionization potential compared to the ground state (Figure 1.3 B).

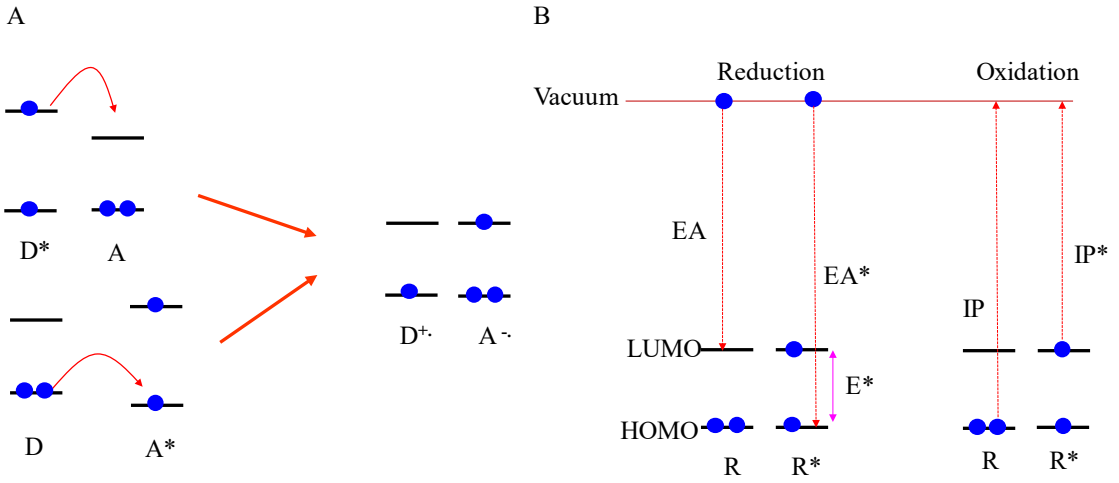

Figure 1.3. (A) A schematic representation of PET in electron D-A systems. (B) The orbital representation of oxidation and reduction process in ground-state (R) and excited state (R*).

Rehm and Weller established a correlation between the electron transfer mediated quenching of the excited state with excitation energy of the donor or acceptor, and redox potential of the redox partners.[27,28] They formulated an equation (1) to predict the free energy of electron transfer in terms of redox potential, excitation energy, and coulombic interaction.[27]

$$\Delta G_{et} = E(D^+/D) \ - E(A/A^-) - E_{00} - \frac{e^2}{\varepsilon d} \quad (1)$$

Where, $E(D^+/D)$ and $E(A/A^-)$ are the respective oxidation and reduction potential of donor and acceptor in the ground-state. E_{00} is the optical transition energy between vibrationally relaxed excited state and ground-state of the donor or acceptor. The last term in the equation corresponds to the coulombic stabilization energy associated with the electrostatic attraction between the radical ion pair at an encounter distance 'd' in a solvent with dielectric constant ε .

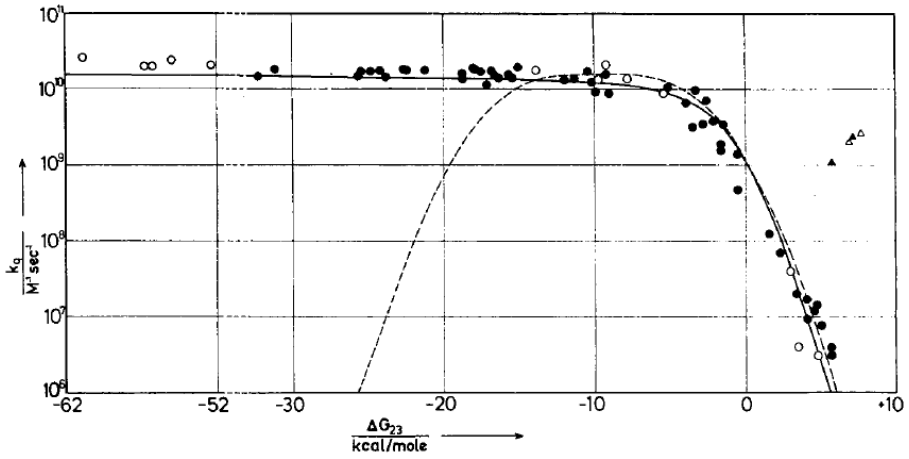

Figure 1.4. A) A plot of fluorescence quenching rate constant mediated by electron transfer vs. exothermicity of the reaction. Reprinted from Ref 27.

Rehm and Weller studied, ca. 60 different electron donor-acceptor systems to interpret the relationship between the rate constant for electron transfer mediated fluorescence quenching and free energy of electron transfer. The plot of k_{et} vs. ΔG_{et} shows a steep decrease in the endothermic region with positive ΔG_{et} values. Although the rate constant increases with increasing the exothermicity (ΔG_{et} <0) interestingly, the rate constant reaches a plateau value of ca. 2×10^{10} $M^{-1}s^{-1}$, and the rate constant shows unvarying behavior while increasing the exothermicity of the electron transfer reaction, as shown in Figure 1.4. However, for the maximum achievable negative value of ΔG_{et}, the rate of electron transfer remains diffusion-controlled in their studies.[27] In other words, the absolute rate constant for electron transfer cannot be measured in the plateau region where, diffusion is the rate-limiting step instead of electron transfer. Although, in a recent

study, E. Vauthey and co-workers revisited the Rehm-Weller behaviour using 14 electron donor-acceptor pairs and tried to study diffusion free, intrinsic electron transfer rate constant. And finally, they rationalized the driving force dependence in terms of Marcus theory.[29]

The early contributions to electron transfer research are from Taube, Libby, and Marcus.[30-35] The theoretical aspects of electron transfer in the condensed phase were emphasized by the efforts of Franck and Libby. Libby proposed the applicability of the Franck-Condon principle in not only light-induced vertical transitions but also in nonradiative electron transfer occurring in the dark. The electron transfer research started from self-exchange reactions and later developed into cross-reactions. Libby found that electron transfer involving in larger cations in aqueous solution is faster than the one that occurs in smaller ions. According to Libby, the bimolecular electron transfer leads to the formation of a new set of ions in a wrong environment of solvent molecules since, during the fast electron jump, the nuclei neither obtain considerable time for the reorganization of the nuclear coordinates and nor the solvent molecules gets time for reorientation. In Libby's analogy, the electron jump happens in a vertical manner, and the change in solvent structure happens after the electron jump. However, the reaction under the investigation was occurring in the dark, the conservation of energy was amiss in his studies. Furthermore, this assumption led to the formulation of the Marcus theory of electron transfer. Marcus stated that sudden jump of electron prior to the reorganization of the reactants and the surrounding solvent medium is only possible with the absorption of a photon. In the case of a dark reaction, it is necessary to facilitate fluctuations in the nuclear coordinates and orientation of the solvent molecule to reach an equilibrium isoenergic state in order to satisfy the conservation of energy and to permit electron transfer in the dark.[32-34]

Marcus used potential energy surfaces and statistical mechanics in the light of transition state theory to explain the electron transfer process occurring in a condensed medium. The electron transfer reaction starts with the diffusion of electron donor and acceptor, and during which, the random motion of the molecules leads to the collision to form a precursor complex. During the lifetime of this complex, the structural changes, the reorganization of the nuclear coordinates, and the orbital changes occurs to achieve the

transition state where electron transfer proceeds to form a successor complex. Then the solvent separation leads to free ions production. The electron transfer proceedings are explained using the parabolic Gibbs free energy curves as a function of reaction coordinates, as shown in Figure 1.5. The energy difference between the two minima of the curves represents the free energy of electron transfer (ΔG^0). The energy difference between the minimum of the reactant curve and the crossing point of the two parabolas represents the activation energy (ΔG^*). The vertical energy difference between the minimum of the reactant curve and the overlap region gives the reorganization energy (λ). During the electron transfer, the reactants rearrange and passes through the reaction coordinates to the crossing point, which is known as the transition state where both product and reactant have matching the nuclear configuration and equal potential energy, and thus electron transfer occurs.[37,38]

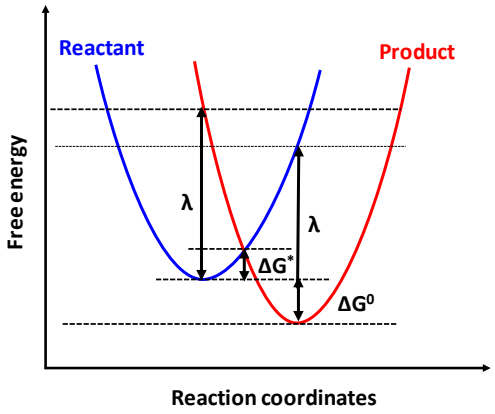

Figure 1.5. The schematic representation of one-dimensional profile of free energy surface in nonadiabatic electron transfer reactions.

According to Marcus model, the rate of electron transfer,

$$k = A\, exp\left[\frac{-\Delta G^*}{k_B T}\right] \tag{2}$$

The activation energy is given by

$$\Delta G^* = \frac{\lambda}{4}\left[1 + \frac{-\Delta G^0}{\lambda}\right]^2 \tag{3}$$

The pre-factor A in equation 2 depends on nature of electron transfer (bimolecular or intramolecular). The reorganization energy term can be expressed as the energy required to change the reactants to the equilibrium configuration in order to elicit electron transfer. This term includes the contribution from the orientation and polarization of solvent molecule, outer-sphere reorganization energy (λ_0), and the nuclear reorganization comprising a change in bond length, and molecular orientation, and inner-sphere reorganization energy (λ_i).

$$\lambda = \lambda_0 + \lambda_i \tag{4}$$

The inner-sphere reorganization energy is given by

$$\lambda_i = \frac{1}{2}\sum_i f_i \left(r_R^{eq} - r_P^{eq}\right)^2 \tag{5}$$

Where, r_R^{eq} and r_P^{eq} are the equilibrium bond length in reactants and product states and f_i corresponds to the reduced force constant of i^{th} vibration and sum of all the molecular vibrations are considered in eq. 5. The outer-sphere reorganization energy is given as

$$\lambda_0 = (\Delta e^2) \left[\frac{1}{2a_1} + \frac{1}{2a_2} - \frac{1}{R}\right] \left[\frac{1}{D_{op}} - \frac{1}{D_s}\right] \tag{6}$$

Where a_1, a_2, and R are the radii of electron donor and acceptor and distance between the center of the donor sphere and acceptor sphere, respectively. D_{op} and D_s are the optical and static dielectric constant of the solvent. $(\Delta e)^2$ is the amount of charge transferred.[34] Marcus expressed the correlation between the rate of electron transfer and reorganization energy and the free energy of electron transfer using the parabola model as in three regimes, as shown in Figure 1.6.[38]

There is a quadratic relationship between ΔG^0 and k_{ET}.The relationship can be explained in three exergonicity region, as shown in Figure 1.6. While increasing the ΔG^0 value, the activation barrier decreased, elevating the rate of electron transfer in the regular regime ($\Delta G^0 < \lambda$). In the activationless region where $\Delta G^0 = \lambda$ and the activation barrier becomes zero lead to the maximum rate of electron transfer. However, in the exergonic region, the ΔG^0 becomes more negative, and the intersection of the energy surface of reactants and products moves towards left, causing re-appearance of the activation barrier,

which slows down the electron transfer. This region is known as the Marcus inverted region.[39.40] Although the inverted region effect is efficiently utilized for conversion of photon energy to chemical energy by establishing a long-living charge-separated state in a manner of keeping the energy-wasting back electron transfer in the inverted region.[41,42]

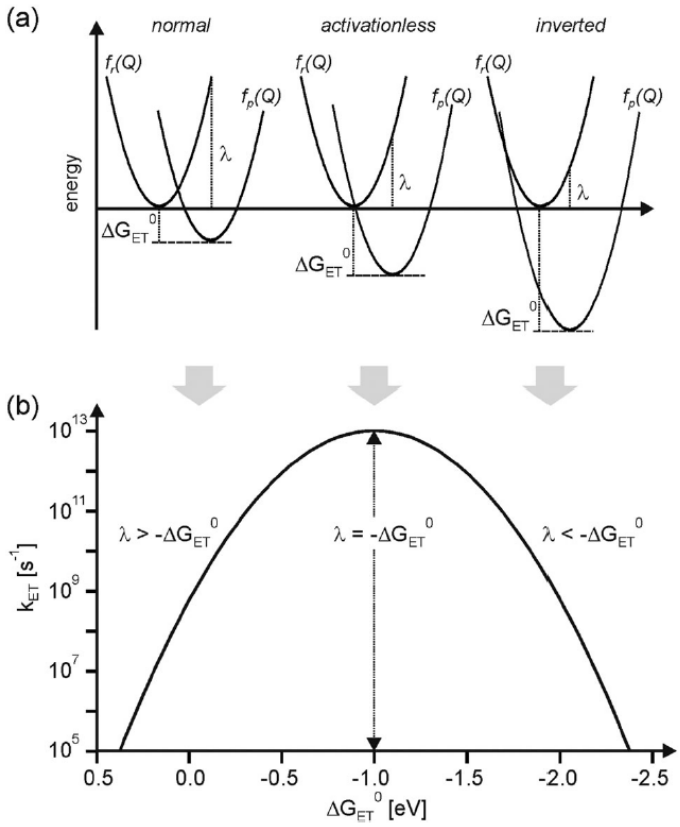

Figure 1.6. (a) Reactant (fr(Q)) and product potential energy wells (fp(Q)) for electron transfer in three different regimes; (b) dependence of electron transfer rates (k_{ET}) on reaction free energy (ΔG^0_{ET}). A reorganization energy (λ) of 1.0 eV was arbitrarily chosen. Reprinted from Ref 38.

1.5 PET in fluorescence sensors

Fluorescence sensors have been largely applied in analytical chemistry and clinical settings due to the excellent features such as high sensitivity, selectivity, cost-effectiveness, and fast response. A broad range of fluorogenic sensors works on the principle of PET, and such sensors show fluorescence *off to on* response in the presence

of the analyte. The basic design of such sensors is fluorophore-spacer-receptor as shown in Figure 1.7. The photoinduced intramolecular electron transfer from the receptor to excited state fluorophore makes the sensor nonfluorescent. The interaction of the analyte with the receptor part leads to its chemical modification or formation of a complex which consequently block the PET to give the fluorescence signal.[44-46]

While designing a sensor, several factors are extensively evaluated. Firstly, the selection of the receptor. The receptors are recommended to show high selectivity and sensitivity to the analyte. The sensing efficiency highly relies on the interaction between the receptor and analyte. The selection of the fluorophore is the next step. The fluorophores are chosen based on the color of signal; for instance, red emitting molecules are preferred for biological sensing. The rational choice of the receptor and fluorophore is very important since the feasibility of the electron transfer is governed by the redox potentials of the electron donor and acceptor counterparts and the electronic transition energy to satisfy the Rehm-Weller thermodynamic condition.

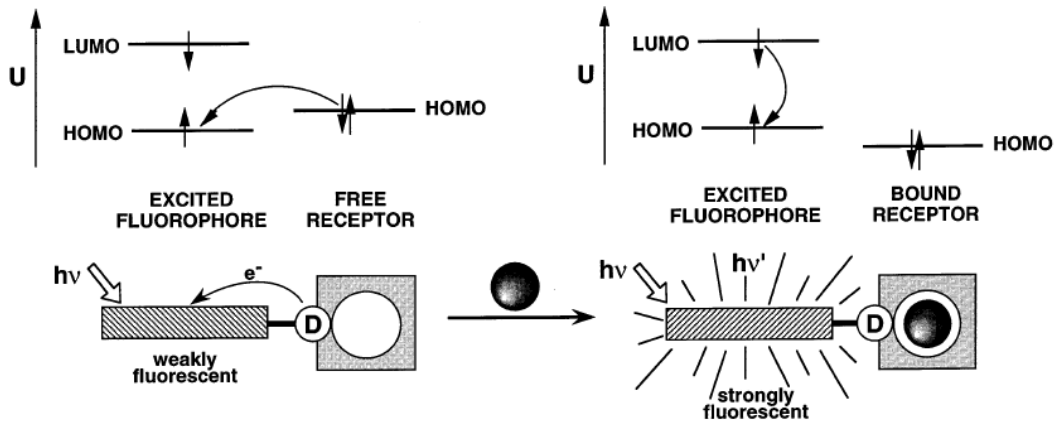

Figure 1.7. Molecular orbital diagram of the fluorophore-receptor combination in the presence and absence of the analyte and the schematic representation of the fundamental design of a fluorescence sensor. The sensor is in a fluorescence off state in the pristine form by PET and in the presence of the analyte, the PET is blocked, leading to fluorescence on state. Reprinted from Ref 46.

The mechanism of sensing can be explained using the molecular orbital energy diagrams, as shown in Figure 1.7. The highest occupied molecular orbital (HOMO) of the

receptor resides above the HOMO of the fluorophore. The electron transfer takes place to the vacant HOMO of the photoexcited fluorophore from the high-lying HOMO of the receptor to quench the fluorescence. The binding of the analyte to the receptors lowers the energy of the HOMO, which consequently suppress the PET to turn on the fluorescence. [44-46]

Mainly fluorescence sensors are employed for pH sensing, detection of metal ions, anions, water, sensing of biomolecules as proteins, enzymes, nucleic acids, and detection of reactive oxygen species (ROS). For the detection of metal ions, different types of recognition moieties are used to trap the metal ions, for example, crown ethers, cryptants, podands, and chelating agents. The conventional fluorescence signalling moieties are anthracenes, rhodamine and coumarins.[46] On the other hand, for the detection of anions chemo sensors with receptors such as calix[4]pyrroles, quinoxaline, polyamines are used. [47]

1.5.1 PET based sensors for reactive oxygen species

ROS impose both positive and negative impacts on the biological systems. The overproduction of ROS in the biological system and the imbalance in the antioxidant defence mechanisms leads to oxidative stress which causes tissue damage and various diseases such as diabetes, cancer, Alzheimer's, Parkinson's disease.[48] Therefore, assessment of oxidative stress is vital for the prevention of such diseases. There are various techniques employed for detection of reactive oxygen species, which include electrochemical methods and spectroscopic techniques. Among the spectroscopic techniques, fluorescence sensing is simpler and faster. In 2007, Nagano and co-workers reported a rhodamine-based fluorescence sensor to detect highly reactive oxygen species (hROS) such as hydroxy radical, peroxynitrile, and hypochlorite. The probes, MitoAR/MitoHR are composed of rhodamine structure conjugated to 4-amino phenyl ether or 4-hydroxy phenyl ether, respectively. The probe is nonfluorescent due to PET. In the presence of hROS, the electron donor, 4-amino phenyl ether, or 4-hydroxy phenyl ether detach from the rhodamine part to release the fluorescence (Figure 1.8).[49]

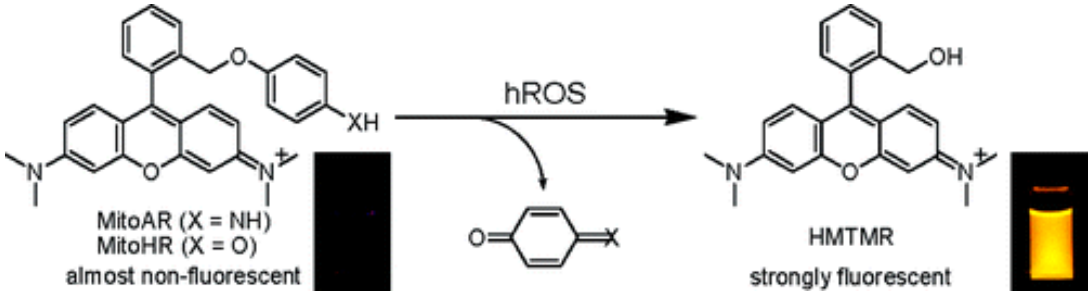

Figure 1.8. The scheme for fluorescence sensing of hROS by MitoAr/MitoHR. Reprinted from Ref 49.

Later, Xiao et al. reported fluorescence sensors based on lanthanide complexes for hROS. The probe comprises Europium or Terbium ions chelated to a dual functional ligand, [4′-(p-aminophenoxy)methylene-2,2′:6′,2″-terpyridine-6,6″-diyl]-bis(methylenenitrilo)tetrakis(acetic acid). The PET between aminophenyl part and terpyridine-lanthanide part makes the complex nonfluorescent. hROS reacts with the probe to cleave the aminophenyl ether group to generate highly fluorescent complexes of Terbium or Europium (Figure 1.9).[50]

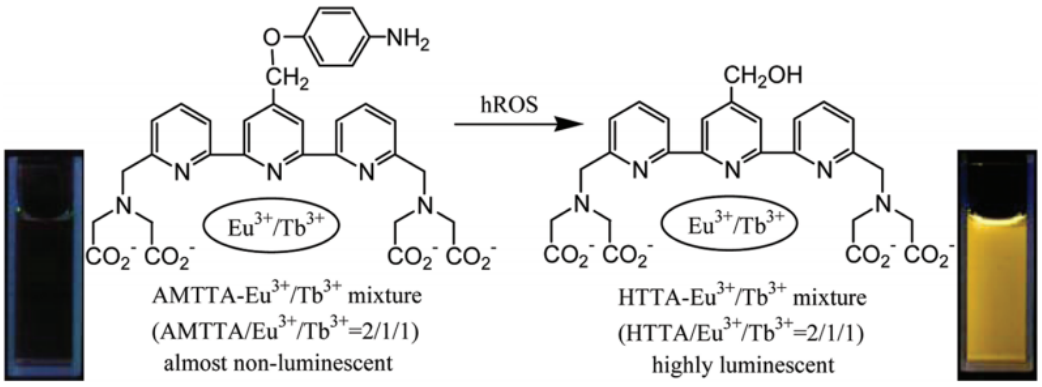

Figure 1.9. The scheme for fluorescence sensing of highly reactive oxygen species by the lanthanide complexes. Reprinted from Ref 50.

For the selective detection of the hydroxyl radical, Qu et al. designed an electron D-A based sensor which is composed of a triphenylphosphine conjugated BODIPY. PET from the phosphorus atom of triarylphosphine to the BODIPY is suppressed due to

oxidation of triarylphosphine to triarylphosphine oxide by hydroxyl radical, which unlocks the NIR fluorescence of BODIPY (Figure 1.10).[51]

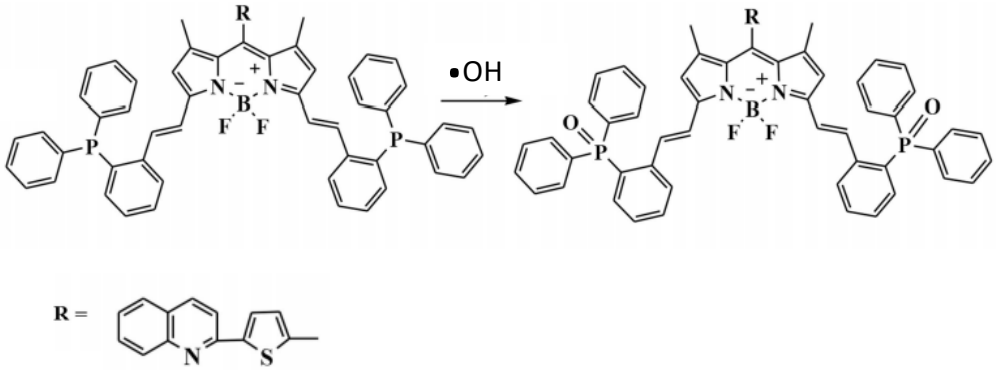

Figure 1.10. The scheme for fluorescence sensing of hydroxyl radical by the probe 2b. Reprinted from Ref 51.

For the selective detection of peroxynitrite in aqueous solution, Li et al. developed an electron D-A dyad based on 1,8-naphthalimide a-methyl(4-hydroxyphenyl)amino conjugate (NP). The reaction with peroxynitrile leads to N-dearylation to release the fluorophore, naphthalimide (Figure 1.11).[52]

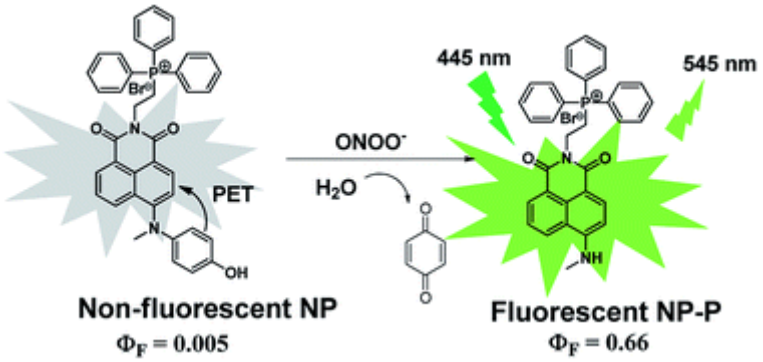

Figure 1.11. The scheme for fluorescence sensing of peroxynitrile by the probe NP. Reprinted from Ref 52.

Soni et al. reported a phenothiazine–borondipyrromethene D-A dyad for selective detection of hypochlorite (Probe 1). Probe 1 undergo oxidation in the presence hypochlorite to form the sulfoxide to block the PET to unlock the green fluorescence (Figure 1.12).[53]

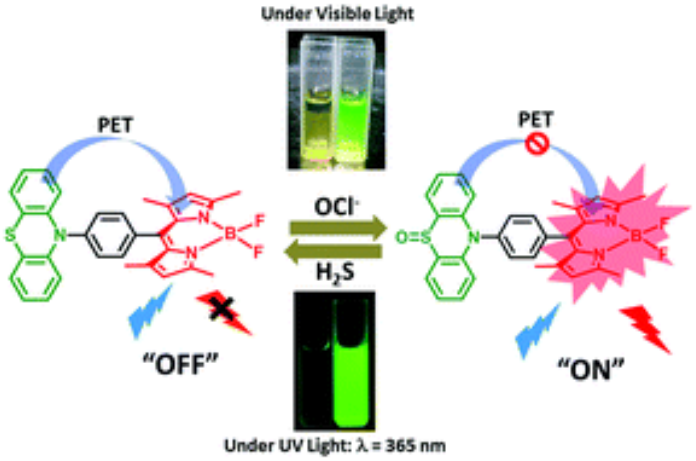

Figure 1.12. The scheme for fluorescence sensing of hypochlorite by the probe 1. Reprinted from Ref 53.

Singlet oxygen ($^1O_2$) is an important member in the ROS family due to its participation in cell signalling and photodynamic therapy. Thereby, various fluorescence sensors for $^1O_2$ have been developed. The sensors can be characterized based on the receptor moieties. For example, anthracene can undergo a [4+2] cycloaddition reaction with $^1O_2$ to produce endoperoxide. Therefore, anthracene-based D-A dyad fluorescence sensors are developed. The frequently used chromophores are xanthene derivatives (Figure 1.13).[54] The sensor molecule is designed to possess intramolecular electron transfer which gets blocked under oxidation by $^1O_2$.[54-60]

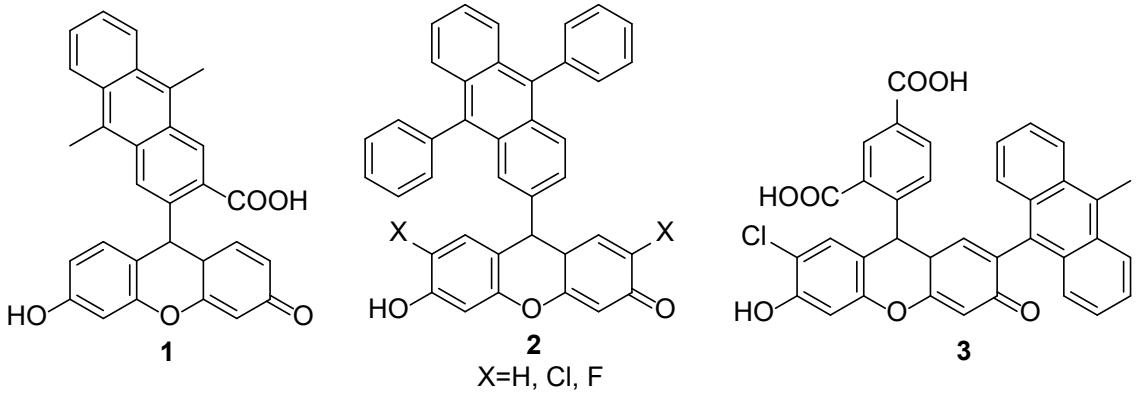

Figure 1.13. The structures of fluorescence sensors of $^1O_2$ based on anthracene-xanthene conjugates.

Another class of fluorescence sensor is composed of histidine as the $^1O_2$ receptor. For example, Xu et al. reported a histidine-cyanine conjugate. The cycloaddition reaction between the imidazole part of histidine blocks the PET to unlock the cyanine fluorescence.[61]

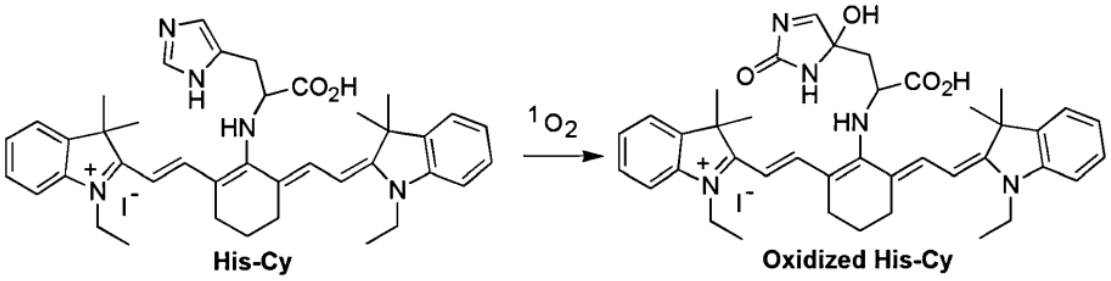

Figure 1.14. The scheme for fluorescence sensing of $^1O_2$ by the probe **His-Cy**. Reprinted from Ref 61.

1.6 Motivation and objectives of this research

The theory of electron transfer helped me to design electron D-A systems with efficient intramolecular electron transfer. The thermodynamic feasibility of the electron transfer is predicted by estimating the free energy change of electron transfer. The value of ΔG^0 is tuned by using appropriate electron donor and acceptor candidates with suitable redox potentials. Therefore, in this study, the redox potentials and the distance between the donor and acceptor, which in turn controlled by the covalent spacer, was carefully selected to make sure the thermodynamic feasibility of electron transfer using eq.1. The geometries and distance between the electron donor and acceptor have a crucial role in controlling the efficiency of electron transfer since the electronic coupling between reactants is largely affected by the center to center distance (R). Therefore, I used short covalent spacers to connect the donors and acceptors to establish efficient electronic coupling, and, the electron transfer efficiency is improved by exerting the possibility of through-bond electron transfer avoiding the rate-limiting diffusion process. I carefully selected individual electron donors and acceptors to make a compact D-A system to minimize the reorganization energy to facilitate efficient electron transfer.[43]

In this work, I designed and synthesized different electron D-A dyads with efficient electron transfer, and the photothermal and photochemical activities of these

molecules are extensively studied. The photothermal conversion of light is a less explored area which demands further attention. Therefore, I used acridinium based electron D-A dyads to efficiently harvest light to convert it into heat energy. On the other hand, PET has been largely exploited in fluorescence sensing. Among the biological sensors, the fluorescence sensors of singlet oxygen ($^1O_2$) attracted significant attention owing to the therapeutic applications of $^1O_2$ in photodynamic therapy (PDT). The promising fluorescence sensors of $^1O_2$ are anthracene-based electron D-A systems. An electron D-A dyad is constructed to establish efficient electron transfer between anthracene and a fluorescence reporter molecule.[44] Despite there are a large number of fluorescence sensors reported, the correlation study of structure and sensitivity of the sensor demands further attention and such study will help to improve the sensitivity of fluorescence sensing.[44-49] Therefore, in this work, I study the role of substituents on anthracene in the rate of $^1O_2$ sensing to improve the sensitivity of $^1O_2$ detection.

The synthesis and characterization of the electron D-A dyads along with the instrumentation techniques used to examine their properties are provided in chapter 2. In chapter 3, the photothermal energy conversion by acridinium based electron D-A dyads is extensively studied. In chapter 4, I study the kinetics of $^1O_2$ sensing by anthracene-based electron D-A dyads. In chapter 5, the mechanism of $^1O_2$ reaction is studied. The summary of the whole thesis is provided in chapter 5.

References

1. Suppan, P. *Chemistry and light*. Royal Society of Chemistry, **1994**.
2. Kuznetsov, A.M.; Ulstrup, J. *Electron transfer in chemistry and biology;* Wiley: Chichester, **1999**.
3. Hou, H. J. M.; Najafpour, M. M.; Moore, G. F.; Allakhverdiev, S. I. *Photosynthesis: Structures, Mechanisms, and Applications*; Springer, **2017**.
4. Berardi, S.; Drouet, S.; Francàs, L.; Gimbert-Suriñach, C.; Guttentag, M.; Richmond, C.; Stoll, T.; Llobet, A. Molecular Artificial Photosynthesis. *Chem. Soc. Rev.* **2014**, *43* (22), 7501–7519.
5. Nelson, N.; Ben-Shem, A. The Complex Architecture of Oxygenic Photosynthesis. *Nat. Rev. Mol. Cell. Biol.* **2004**, *5* (12), 971–982.
6. Olson, J. M.; Blankenship, R. E. Thinking about the Evolution of Photosynthesis. *Photosynth. Res.* **2004**, *80* (1–3), 373–386.
7. El-Khouly, M. E.; El-Mohsnawy, E.; Fukuzumi, S. Solar Energy Conversion: From Natural to Artificial Photosynthesis. *J. Photochem. Photobiol. C Photochem. Rev.* **2017**, *31*, 36–83.
8. Nugent, J. H. A. Oxygenic Photosynthesis Electron Transfer in Photosystem I and Photosystem II. *Eur. J. Biochem.* **1996**, *237* (3), 519–531.
9. Cheng, Y.-C.; Fleming, G. R. Dynamics of Light Harvesting in Photosynthesis. *Annu. Rev. Phys. Chem.* **2009**, *60* (1), 241–262.
10. Listorti, A.; Durrant, J.; Barber, J. Artificial Photosynthesis: Solar to Fuel. *Nat. Mater.* **2009**, *8* (12), 929–930.
11. Barber, J.; Tran, P. D. From Natural to Artificial Photosynthesis. *J. R. Soc. Interface* **2013**, *10* (81), 20120984.
12. Fukuzumi, S.; Ohkubo, K.; Suenobu, T. Long-Lived Charge Separation and Applications in Artificial Photosynthesis. *Acc. Chem. Res.* **2014**, *47* (5), 1455–1464.
13. Hersch, P.; Zweibel, K. Basic photovoltaic principles and methods. Solar Energy Research Inst, Golden, **1982**.
14. Tiedje, T. O. M.; Yablonovitch, E. L. I.; Cody, G. D.; Brooks, B. G. Limiting Efficiency of Silicon Solar Cells, **1984**, 711–716.

15. Morgera, A. F.; Lughi, V. Frontiers of Photovoltaic Technology: A Review. *5th Int. Conf. Clean Electr. Power Renew. Energy Resour. Impact, ICCEP 2015*. **2015**, 115–121.
16. Goetzberger, A.; Luther, J.; Willeke, G. Solar Cells: Past, Present, Future. **2002**, *74*, 1–11.
17. Brown, G. F.; Wu, J. Third Generation Photovoltaics. *Laser Photonics Rev.* **2009**, *3* (4), 394–405.
18. Liu, J.; Yao, M.; Shen, L. Third Generation Photovoltaic Cells Based on Photonic Crystals. *J. Mater. Chem. C* **2019**, *7* (11), 3121–3145.
19. Green, M. A.; Ho-Baillie, A.; Snaith, H. J. The Emergence of Perovskite Solar Cells. *Nat. Photonics* **2014**, *8* (7), 506–514.
20. Ye, M.; Wen, X.; Wang, M.; Iocozzia, J.; Zhang, N.; Lin, C.; Lin, Z. Recent Advances in Dye-Sensitized Solar Cells: From Photoanodes, Sensitizers and Electrolytes to Counter Electrodes. *Mater. Today* **2015**, *18* (3), 155–162.
21. Listorti, A.; O'Regan, B.; Durrant, J. R. Electron Transfer Dynamics in Dye-Sensitized Solar Cells. *Chem. Mater.* **2011**, *23* (15), 3381–3399.
22. Yen, Y. S.; Chou, H. H.; Chen, Y. C.; Hsu, C. Y.; Lin, J. T. Recent Developments in Molecule-Based Organic Materials for Dye-Sensitized Solar Cells. *J. Mater. Chem.* **2012**, *22* (18), 8734–8747.
23. Kurumisawa, Y.; Higashino, T.; Nimura, S.; Tsuji, Y.; Iiyama, H.; Imahori, H. Renaissance of Fused Porphyrins: Substituted Methylene-Bridged Thiophene-Fused Strategy for High-Performance Dye-Sensitized Solar Cells. *J. Am. Chem. Soc.* **2019**, *141*, 9910–9919.
24. Sharma, K.; Sharma, V.; Sharma, S. S. Dye-Sensitized Solar Cells: Fundamentals and Current Status. *Nanoscale Res. Lett.* **2018**, *13*.
25. Hardin, B. E.; Snaith, H. J.; McGehee, M. D. The Renaissance of Dye-Sensitized Solar Cells. *Nat. Photonics* **2012**, *6* (3), 162–169.
26. Mishra, A.; Fischer, M. K. R.; Büuerle, P. Metal-Free Organic Dyes for Dye-Sensitized Solar Cells: From Structure: Property Relationships to Design Rules. *Angew. Chemie - Int. Ed.* **2009**, *48* (14), 2474–2499.
27. Rehm, D.; Weller, A. Kinetics of fluorescence quenching by electron and H-atom transfer. *Isr. J. Chem*. **1970**, 8(2), 259–271.

28. Weller, A. Electron-Transfer and Complex Formation in the Excited State. *Pure Appl. Chem.* **1968**, *16* (1), 115–124.
29. Rosspeintner, A.; Angulo, G.; Vauthey, E. Bimolecular Photoinduced Electron Transfer beyond the Diffusion Limit: The Rehm-Weller Experiment Revisited with Femtosecond Time Resolution. *J. Am. Chem. Soc.* **2014**, *136* (5), 2026–2032.
30. Taube, H. Electron transfer between metal complexes- a retrospective view (Nobel lecture). *Angew. Chem. Int. Ed. Engl.* **1984**, 23(5), 329–339.
31. Marcus, R. A.; Sutin, N. Electron Transfers in Chemistry and Biology. *BBA Rev. Bioenerg.* **1985**, *811* (3), 265–322.
32. Libby, W. F. Theory of Electron Exchange Reactions in Aqueous Solution. *J. Phys. Chem.* **1952**, *56* (7), 863–868.
33. Marcus, R. A. Chemical and Electrochemical Electron-Transfer Theory. *Annu. Rev. Phys. Chem.* **1964**, *15* (1), 155.
34. Marcus, R.A. Electron transfer reactions in chemistry theory and experiment. *J. Electroanal. Chem*.**1997**, 438(1), 251–259.
35. Sutin, N. Electron transfer reactions in solution: A historical perspective. Advances in Chemical Physics: Electron Transfer—from Isolated Molecules to Biomolecules. Part 1, **1999**,106, 7–33.
36. Kavarnos, G. J.; Turro, N. J. Photosensitization by Reversible Electron Transfer: Theories, Experimental Evidence, and Examples. *Chem. Rev.* **1986**, *86* (2), 401–449.
37. Bolton, J.R. and Archer, M.D. Basic electron-transfer theory. Electron Transfer in Inorganic, Organic, and Biological Systems, **1991**, 228, 7–23.
38. Kuss-Petermann, M.; Wenger, O. S. Unusual Distance Dependences of Electron Transfer Rates. *Phys. Chem. Chem. Phys.* **2016**, *18* (28), 18657–18664.
39. Closs, G. L.; Calcaterra, L. T.; Green, N. J.; Penfield, K. W.; Miller, J. R. Distance, Stereoelectronic Effects, and the Marcus Inverted Region in Intramolecular Electron Transfer in Organic Radical Anions. *J. Phys. Chem.* **1986**, *90* (16), 3673–3683.
40. Gould, I. R.; Ege, D.; Moser, J. E.; Farid, S. Efficiencies of Photoinduced Electron-Transfer Reactions: Role of the Marcus Inverted Region in Return

Electron Transfer within Geminate Radical-Ion Pairs. *J. Am. Chem. Soc.* **1990**, *112* (11), 4290–4301.

41. Connolly, J.S.; and Bolton, J.R. Intramolecular electron transfer: History and some implications for artificial photosynthesis. *Photoinduced electron transfer, part D,* **1988**, 303–393.
42. Miller, J. R.; Beitz, J. V.; Huddleston, R. K. Effect of Free Energy on Rates of Electron Transfer between Molecules. *J. Am. Chem. Soc.* **1984**, *106* (18), 5057–5068.
43. Gupta, S.; Matyushov, D. V. Effect of Solvent and Solute Polarizability on the Reorganization Energy of Electron Transfer. *J. Phys. Chem. A* **2004**, *108* (11), 2087–2096.
44. De Silva, A. P.; Moody, T. S.; Wright, G. D. Fluorescent PET (Photoinduced Electron Transfer) Sensors as Potent Analytical Tools. *Analyst* **2009**, *134* (12), 2385–2393.
45. Chatterjee, A.; Suzuki, T. M.; Takahashi, Y.; Pacheco Tanaka, D. A. A Density Functional Study to Choose the Best Fluorophore for Photon-Induced Electron-Transfer (PET) Sensors. *Chem. - A Eur. J.* **2003**, *9* (16), 3920–3929.
46. Valeur, B.; Leray, I. Design Principles of Fluorescent Molecular Sensors for Cation Recognition. *Coord. Chem. Rev.* **2000**, *205* (1), 3–40.
47. Gunnlaugsson, T.; Davis, A. P.; Glynn, M. Fluorescent Photoinduced Electron Transfer (PET) Sensing of Anions Using Charge Neutral Chemosensors. *Chem. Commun.* **2001**, *1* (24), 2556–2557.
48. Betteridge, D. J. What Is Oxidative Stress? *Metabolism.* **2000**, *49* (2 SUPPL. 1), 3–8.
49. Koide, Y.; Urano, Y.; Kenmoku, S.; Kojima, H.; Nagano, T. Design and Synthesis of Fluorescent Probes for Selective Detection of Highly Reactive Oxygen Species in Mitochondria of Living Cells. *J. Am. Chem. Soc.* **2007**, *129* (34), 10324–10325.
50. Xiao, Y.; Ye, Z.; Wang, G.; Yuan, J. A Ratiometric Luminescence Probe for Highly Reactive Oxygen Species Based on Lanthanide Complexes. *Inorg. Chem.* **2012**, *51* (5), 2940–2946.

51. Qu, X.; Song, W.; Shen, Z. A Highly Selective NIR Fluorescent Turn-on Probe for Hydroxyl Radical and Its Application in Living Cell Images. *Front. Chem.* **2019**, *7* (August), 1–8.
52. Li, X.; Hou, J.; Peng, C.; Chen, L.; Liu, W.; Liu, Y. A 1,8-Naphthalimide-Based Fluorescent Probe for Selective and Sensitive Detection of Peroxynitrite and Its Applications in Living Cell Imaging. *RSC Adv.* **2017**, *7* (54), 34287–34292.
53. Soni, D.; Gangada, S.; Duvva, N.; Roy, T. K.; Nimesh, S.; Arya, G.; Giribabu, L.; Chitta, R. Hypochlorite-Promoted Inhibition of Photo-Induced Electron Transfer in Phenothiazine-Borondipyrromethene Donor-Acceptor Dyad: A Cost-Effective and Metal-Free "Turn-on" Fluorescent Chemosensor for Hypochlorite. *New J. Chem.* **2017**, *41* (13), 5322–5333.
54. You, Y.; Nam, W. Designing Photoluminescent Molecular Probes for Singlet Oxygen, Hydroxyl Radical, and Iron-Oxygen Species. *Chem. Sci.* **2014**, *5* (11), 4123–4135.
55. Tanaka, K.; Miura, T.; Umezawa, N.; Urano, Y.; Kikuchi, K.; Higuchi, T.; Nagano, T. Rational Design of Fluorescein-Based Fluorescence Probes. Mechanism-Based Design of a Maximum Fluorescence Probe for Singlet Oxygen. *J. Am. Chem. Soc.* **2001**, *123* (11), 2530–2536.
56. Kim, S.; Tachikawa, T.; Fujitsuka, M.; Majima, T. Far-Red Fluorescence Probe for Monitoring $^1O_2$ during Photodynamic Therapy. *J. Am. Chem. Soc.* **2014**, *136* (33), 11707–11715.
57. Flors, C.; Fryer, M. J.; Waring, J.; Reeder, B.; Bechtold, U.; Mullineaux, P. M.; Nonell, S.; Wilson, M. T.; Baker, N. R. Imaging the Production of $^1O_2$ in Vivo Using a New Fluorescent Sensor, $^1O_2$ Sensor Green®. *J. Exp. Bot.* **2006**, *57* (8), 1725–1734.
58. Pedersen, S. K.; Holmehave, J.; Blaikie, F. H.; Gollmer, A.; Breitenbach, T.; Jensen, H. H.; Ogilby, P. R. Aarhus Sensor Green: A Fluorescent Probe for 1O2. *J. Org. Chem.* **2014**, *79* (7), 3079–3087.
59. Kohara, R.; Yuyama, K.; Shigeri, Y.; Biju, V. Blue-Emitting Electron-Donor / Acceptor Dyads for Naked- Eye Fluorescence Detection of Singlet Oxygen. *ChemPhotoChem*. **2017**, 1(7), 299–303.

60. Sun, M.; Krishnakumar, S.; Zhang, Y.; Liang, D.; Yang, X.; Wong, M. W.; Wang, S.; Huang, D. Singlet Oxygen Probes Made Simple: Anthracenylmethyl Substituted Fluorophores as Reaction-Based Probes for Detection and Imaging of Cellular $^1O_2$. *Sensors Actuators, B Chem.* **2018**, *271* (May), 346–352.
61. Xu, K.; Wang, L.; Qiang, M.; Wang, L.; Li, P.; Tang, B. A Selective Near-Infrared Fluorescent Probe for Singlet Oxygen in Living Cells. *Chem. Commun.* **2011**, *47* (26), 7386–7388.

Chapter 2

Experiments

Abstract: Electron transfer is studied and explored in chemistry and biology.[1] Simple electron transfer systems allow one to study the kinetics and the thermodynamics of electron transfer. Nevertheless, the careful selection of the donor and the acceptor moieties can make the electron transfer system promising for various applications.[2,3] Conventional D-A systems like pyrene- amine and anthracene-amine have helped to understand the mechanistic and kinetic aspects of electron transfer.[4] Such studies have ultimately paved the way to develop ideal electron D-A systems for light-harvesting applications such as in dye-sensitized solar cells.[5] Whether or not an electron D-A systems acts as a photothermal agent or a fluorophore depends upon the efficiency of inter-band nonradiative relaxation. Those with high efficiency non radiative relaxation generate heat, while those with low efficiency show high fluorescence efficiency. Thus, the D-A systems can be either a photothermal agent or a fluorescence sensor.

In this work, I study the photothermal and fluorescence sensing properties of electron D-A dyads. To this purpose, I synthesize acridinium-based electron D-A dyads for photothermal generation and anthracene-based D-A dyads for fluorescence sensing applications. For the synthesis of D-A dyads, I use different linking chemistry such as Grignard reactions and base catalysed nucleophilic substitution reactions to covalently connect the electron donors and acceptors. The compounds are characterized using nuclear magnetic resonance spectroscopy, electrospray ionization mass analysis and Fourier-transform infrared spectroscopy. The optical properties of the compound are examined using steady-state absorption and fluorescence spectroscopy.

2.1 Materials

All chemicals used in this research were analytical grade and used as received unless otherwise stated. 2-bromo-1,3-dimethylphenol, bromopropane, magnesium turnings, potassium carbonate (K_2CO_3), potassium iodide (KI), magnesium sulphate anhydrous ($MgSO_4$), sodium sulphate anhydrous (Na_2SO_4), sodium chloride (NaCl), sodium hydroxide (NaOH), potassium hydroxide (KOH), hydrochloric acid (HCl), sodium azide (NaN_3), and sodium phosphate monobasic were obtained from FUJIFILM Wako Pure Chemical Corporation, Japan. 10-methylacridone, 7-amino-4-methylcoumarin,7-ethylamino-4-methylcoumarin, 9-chloromethylanthracene, Rhodamine 6G, (Rh-6G), 9-mesityl-10-methylacridinium perchlorate, 10-methylacridinium perchlorate, tetrakis(4-carboxyphenyl)porphyrin (TCPP) and Rose Bengal (RB) were obtained from Tokyo Chemical Industry (TCI), Japan. Boron tribromide, 2,2,6,6-tetramethylpiperidine (TEMP) and 2,2,6,6-tetramethylpiperidine-1-oxyl, (TEMPO) were obtained from Sigma Aldrich, USA, Sodium phosphate dibasic was obtained from MP biomedicals, France. All the solvents in reagent grade *N,N*-dimethylformamide (DMF), tetrahydrofuran (THF), dichloromethane (DCM), methanol, chloroform, ethyl acetate, hexane, toluene, distilled water were obtained from FUJIFILM Wako Pure Chemical Corporation, Japan.

2.1.1 Dyads for photothermal energy conversion

Photothermal conversion of light energy is one of the conventional approaches of energy harvesting. There are several reports on various photothermal agents. The metal nanoparticles and graphene-based materials are the leading-edge gamut of photothermal generators. Rigid organic molecules are selected to be a proficient alternative owing to the diminished toxicity and high biocompatibility.[6] Several organic dyes such as cyanine, diketopyrrolopyrroles, and squaraines are developed into active photothermal agents. However, most of the conventional photothermal agents are designed to absorb NIR light to use for biological applications. [7] Thus, there is a need for novel molecules which can efficiently harvest the entire solar spectrum. For this purpose, acridinium-based molecules are designed and synthesized in this study.

2.1.2 Synthesis of 9-(2,6-dimethyl-4-hydroxyphenyl)-10-methylacridinium chloride (Acr1)

In this study, 9-(2,6-dimethyl-4-hydroxyphenyl)-10-methylacridinium chloride (**Acr1**) was designed and synthesized, which shows excellent water solubility and photostability. The synthesis comprises three stages. Initially, the protection of the active -OH group of the donor moiety (4-bromo-1,3-dimethylphenol) with bromopropane. In the next step, I prepared the Grignard reagent, which was followed by the reaction of the Grignard reagent with 10-methylacridone. Finally, the deprotection procedure was applied to replace the propoxy group with hydroxy group, which provided **Acr1**.

Step1. Protection of the active -OH group

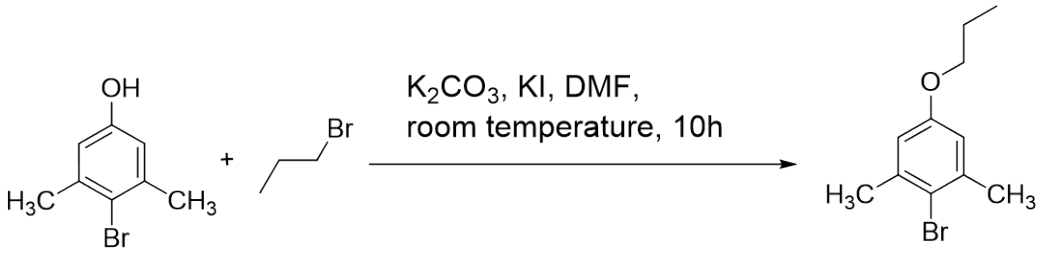

Scheme 2.1. A scheme for the preparation of 2-bromo-1,3-dimethyl-5-propoxybenzene.

To a DMF solution of 4-bromo-3,5-dimethylphenol (4.00 g, 19.89 mmol), bromopropane (8.16 g, 47.03 mmol), K_2CO_3 (6.50 g, 47.0 mmol), and a catalytic amount of KI were added. The reaction was stirred for 10 h at room temperature. The reaction mixture was poured into water (50 mL) and extracted with ethyl acetate (3×50). The organic layer was dried over Na_2SO_4. The product was purified by column chromatography on silica gel (200 mesh) using a mixture a of ethyl acetate and hexane (1:20, v/v) as the eluent to provide a colourless liquid as the product (4.2 g, 87.5 %). The compound was characterized by recording the ^{1}H NMR spectrum.

^{1}H NMR ($CDCl_3$) 500 MHz

δ= 6.62 (s, 2H; Ar-H), 3.83-3.85 (t, 2H; CH_2), 2.35 (s, 6H; CH_3), 1.74-1.79 (m, 2H; CH_2), 0.99-1.02 (t, 3H; CH_3).

Step 2. Grignard reaction

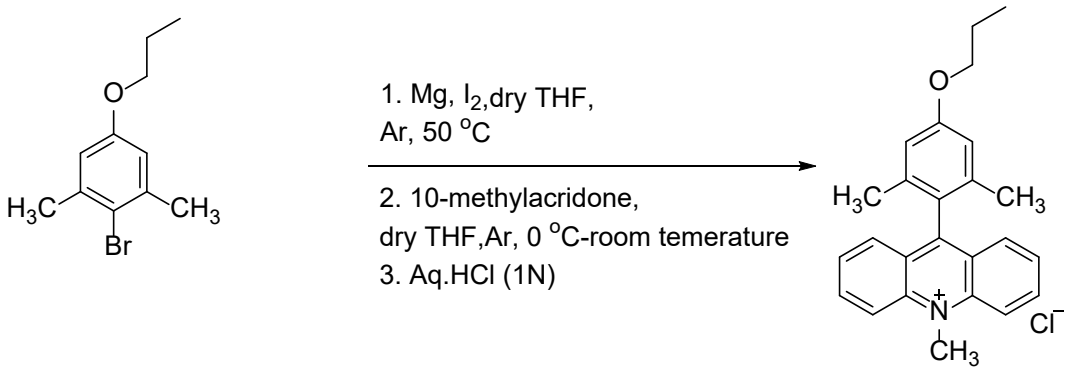

Scheme 2.2. A scheme for the preparation of 9-(2,6-dimethyl-4-propoxyphenyl)-10-methylacridinium chloride.

First, a three neck round bottom flask was charged with 2-bromo-1,3-dimethyl-5-propoxybenzene (800 mg, 3.29 mmol), magnesium turnings (95 mg, 3.94 mmol), catalytic amount of Iodine and dry THF (10 mL). The resulted solution was heated up to 50 °C in the Argon atmosphere, during which the brown colour of the solution was disappeared, and the solution turned into white. The Grignard reagent formed was transferred into a solution of 10-methylacridone (756 mg, 3.61 mmol) in dry THF kept at 0 °C. The reaction solution was stirred for 24 h at room temperature in the Argon atmosphere. After 24 h, aq. HCl was added to maintain the neutral pH at 7. The reaction mixture was extracted using dichloromethane (4×50), the organic layer was dried over $MgSO_4$ and the compound was purified by silica-gel chromatography using a mixture (1:20, v/v) of methanol and dichloromethane as the eluent. 9-(2,6-dimethyl-4-propoxyphenyl)-10-methylacridinium chloride was obtained as a dark brown solid (yield: 489 mg, 38 %). The compound was characterized by recording the ^{1}H NMR spectrum.

^{1}H NMR (methanol-d4) 500 MHz

δ= 8.81-8.85 (d, 2H; Ar-H), 8.43-8.47 (t, 2H; Ar-H), 7.90-7.96 (m, 4H; Ar-H), 6.99 (s, 2H; Ar-H), 5 (s, 3H; CH_3), 4.08-4.11 (t, 2H; CH_2), 1.87-1.91 (m, 2H; CH_2), 1.75 (s, 6H; CH_3), 1.11-1.14 (t, 3H; CH_3).

Step 3. Deprotection with BBr_3

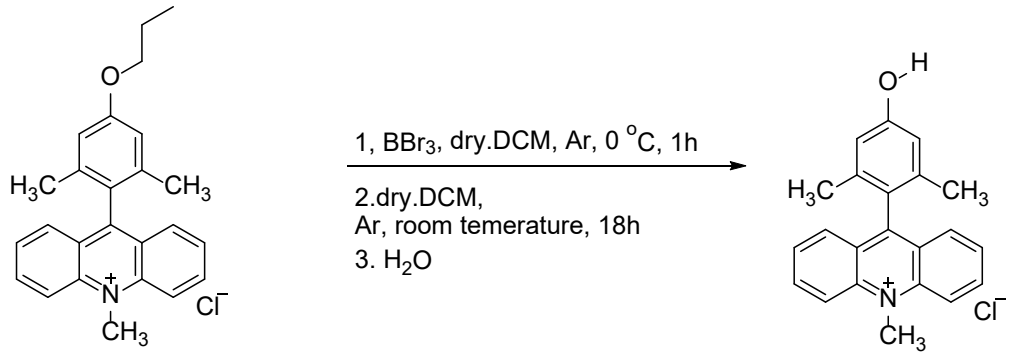

Scheme 2.3. A scheme for preparation **Acr1.**

9-(2,6-dimethyl-4-propoxyphenyl)-10-methylacridinium chloride (122 mg, 0.31 mmol) was dissolved in dry DCM (5 mL) in the Argon atmosphere. This reaction mixture was cooled to 0 °C, boron tribromide (233.73 mg, 0.93 mmol) was added dropwise and the reaction mixture was stirred for 18 h at room temperature. Then an excess of water was added and a yellow precipitate formed, which was filtered and washed with DCM (yield: 80 mg, 73 %). The target compound, **Acr1** was characterized by recording ^{1}H,^{13}C NMR spectra, ESI-MS, FT-IR spectroscopy, UV-Vis absorption spectrum, and fluorescence spectrum.

^{1}H NMR (methanol-d4) 500 MHz

δ= 8.79-8.81 (d, 2H; Ar-H), 8.42-8.46(t, 2H; Ar-H), 7.96-7.98 (t, 2H; Ar-H), 7.90-7.93 (d, 2H; Ar-H), 6.85 (s, 2H; Ar-H), 4.99 (s, 3H; CH_3), 1.70 (s, 6H; CH_3).

^{13}C NMR (methanol-d4) 500 MHz

δ= 164.40 (C-CH), 160.47 (C-CH), 143.24 (C-CH), 140.24 (C-CH), 138.95(C-C), 130.38 (C-CH), 129.60 (C-CH), 128.07 (C-CH), 124.80 (C-CH), 120.41(C-CH), 116.23(C-CH), 39.62 (s; CH_3), 20.34 (s; CH_3).

FTIR (KBr): *v*= 3055 (vs) cm^{-1} (-OH) , 2281 cm^{-1} (s), 1609 cm^{-1} (vs), 1547 cm^{-1} (s), 1442 cm^{-1} (s), 1387 cm^{-1} (s), 1316 (s) cm^{-1}, 1196 cm^{-1}, 1159 (s) cm^{-1}, 875 (s) cm^{-1}, 757 (s) cm^{-1}

HRMS (ESI): *m/z* -mass calculated for $C22H20NO^{+}$: 314.1539 $[M]^{+}$; found 314.1538.

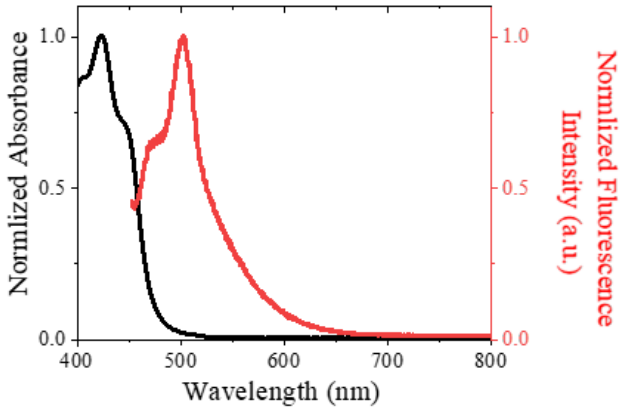

Figure 2.1. The normalized absorption and fluorescence (λ_{ex}: 430 nm) spectra of aqueous solution of **Acr1**.

2.1.3 Preparation of 9-mesityl-10-methylacridinium chloride (Acr2)

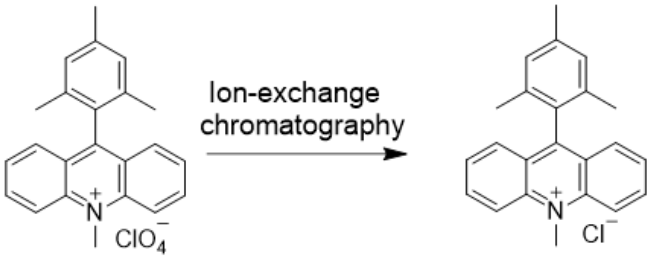

Scheme 2.4. A scheme for the preparation of **Acr2**.

Acr2 was prepared according to a reported procedure.[8] Ion exchange chromatography was applied to change the counterion to chloride. An ion-exchange column in chloride cycle (Amberlite-IRA 410; pre-rinsed overnight) was washed with methanol: acetonitrile (1:1 v/v) mixture. The washing procedure was repeated once again. 9-mesityl-10-methylacridinium perchlorate (200 mg) was dissolved in 1:1 methanol, acetonitrile mixture and loaded on the column. The same solvent was used for the elusion. Then, the solvent was evaporated to afford yellow solid (162 mg, 80 %) as product.

2.1.4 Electron donor-acceptor based fluorescence sensors of singlet oxygen

The most promising fluorescence sensors of singlet oxygen ($^1O_2$) are electron D-A dyads showing low fluorescence quantum efficiency in the native form and high fluorescence quantum efficiency after oxidation by $^1O_2$. Substituted anthracenes occupy the mainstream of $^1O_2$ fluorescence sensors. In 1999, Umezawa et al. reported the first fluorescein-anthracene conjugate, **DPAX** (9-[2-(3-carboxy-9,10-diphenyl)anthryl]-6-hydroxy-3H-xanthen-3-one).[9] Later in 2001, the same group reported a modified sensor, **DMAX** by replacing the phenyl groups in the anthracene part to improve the speed of detection.[10]

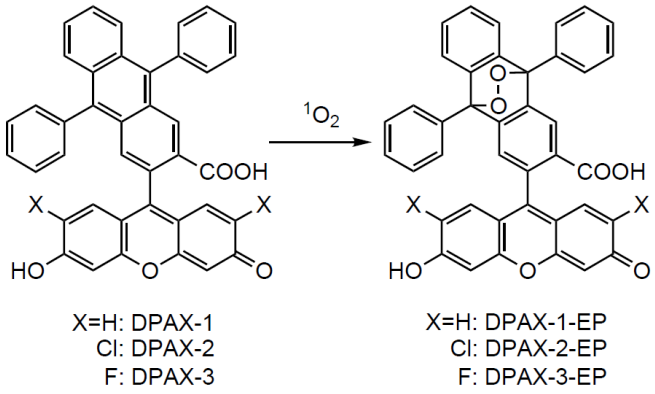

Figure 2.2. The $^1O_2$ sensing by fluorescein-anthracene conjugates. Reprinted from Ref 9.

The commercially available $^1O_2$ sensor, Singlet Oxygen Sensor Green (SOSG), showed appreciable selectivity and sensitivity.

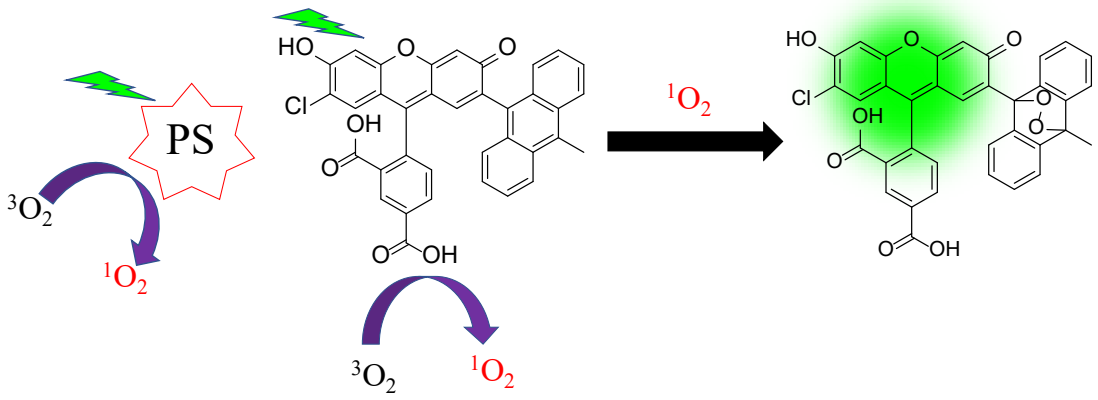

Figure 2.3. The structure of SOSG, and fluorescence uncaging of SOSG by the reaction with $^1O_2$ generated by either photoactivated photosensitizer (PS) or self-sensitization.

Nevertheless, the UV-vis exposure caused auto sensitization causing overestimation of the result, limiting the reliability of the sensing action.[11] In order to lift the limitation of auto-sensitization, Kim et al. introduced a new sensor, Si-DMA (silicon-containing Rhodamine-Anthracene conjugate). This sensor showed not only high sensitivity and selectivity but also attractive biocompatibility, and as the result used for invitro-sensing during photodynamic therapy. However, lengthy and tedious synthesis and the overlap of absorption of Si-DMA with common photosensitizers limit the application of this probe.[12]

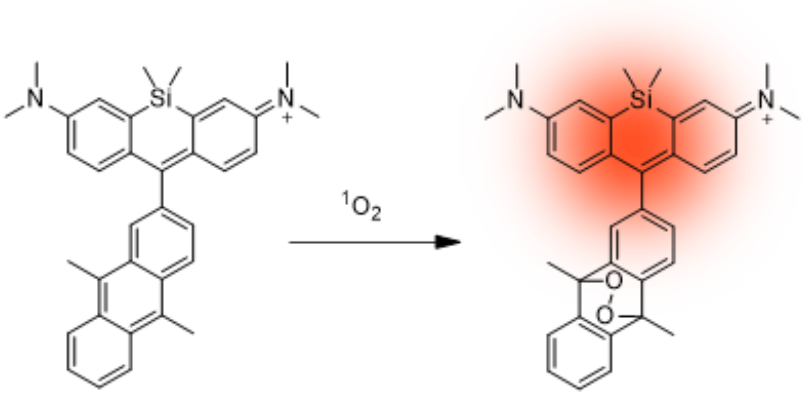

Figure 2.4. The schematic representation of $^1O_2$ sensing by Si-DMA.

Later, our research group reported a novel singlet oxygen sensor, S**1**, which is a coumarin-anthracene conjugate.

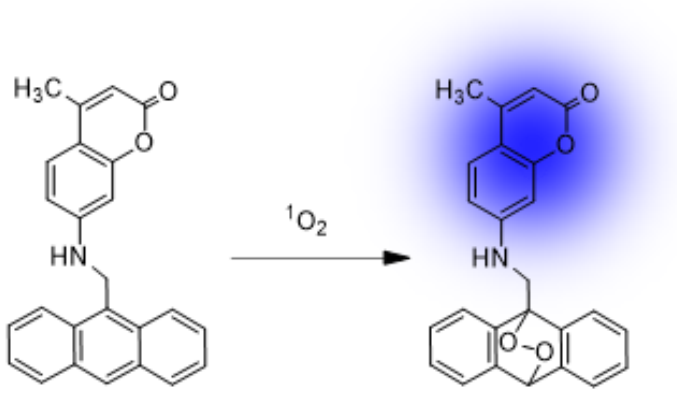

Figure 2.5. The schematic representation of $^1O_2$ sensing by **S1**.

The sensor was prepared in a single step reaction. The $^1O_2$ sensing by **S1** enables the naked-eye detection of the blue fluorescence of oxidized form of **S1**. One of the advantages of **S1** is the selective excitation in the presence of common photosensitizers.[13]

2.1.5 Synthesis of singlet oxygen sensors

2.1.5.1 Synthesis of 7-[9-(methylanthryl)amino]-4-methyl-chromen-2-one (S1)

S1 was prepared using a procedure different from the reported one. [13]

I dissolved 7-Amino-4-methylcoumarin (0.10 g, 0.57 mmol) and 9-chloromethylanthracene (0.12 mg, 0.57 mmol) in 10 mL of DMF. Then, K_2CO_3 (78 mg, 5.7 mmol) and KI (5 mg, 0.03 mmol) were added to the solution, and this reaction mixture was stirred at 85 ^oC for 5 h. The reaction mixture was cooled to room temperature, and excess water was added, which provided a pale-yellow residue. The pH of the solution was adjusted to 6-7 using aq. HCl. The residue was filtered and dried. The powder was re-dissolved in hot THF and then reprecipitated by adding excess of acetone, and the residue was filtered and washed with acetone to give a white powder (0.14 g, 70%).

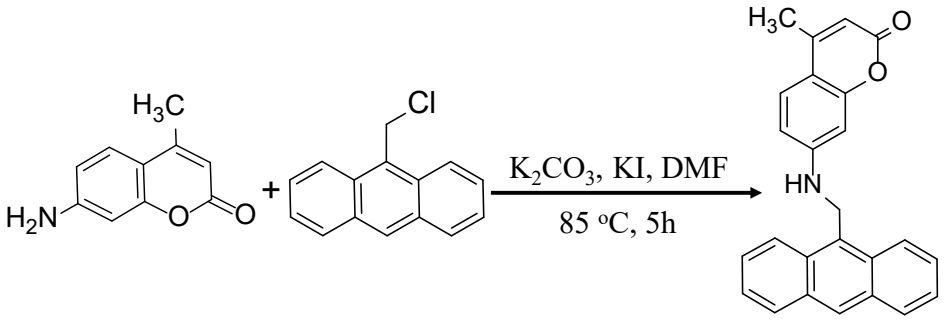

Scheme 2.5. A scheme for synthesis of **S1**.

The compound was characterized by recording the ^1H NMR spectrum in dmf-d7.

^1H NMR (DMF -d7) 500 MHz

δ= 8.89 (s, 1H; Ar-H), 8.58 (d, 2H; Ar-H), 8.36 (d, 2H; Ar-H), 7.74-7.81 (m, 5H; Ar-H), 7.09-7.11 (dd, 1H; Ar-H), 7.05-7.06 (d, 1H; Ar-H), 7.02-7.04 (t, 1H; N-H), 6.18 (s, 1H; allylic), 5.51-5.52 (d, 2H; N-CH_2), 2.61 (s, 3H; CH_3).

2.1.5.2 Synthesis of 7-[9-(methylanthryl)(ethyl)amino]-4-methyl-chromen-2-one (S2)

I dissolved 7-(Ethylamino)-4-methylcoumarin (0.10 g, 0.49 mmol) and 9-chloromethylanthracene (0.16 mg, 0.73 mmol) in 10 mL of DMF. Then, K_2CO_3 (47 mg, 2.9 mmol) and potassium iodide (5 mg, 0.03 mmol) were added to the solution, and this reaction mixture was stirred at 85 °C for 5 h. The reaction mixture was cooled to room temperature, and excess water was added, which provided a yellow residue. The pH of the solution was adjusted to ~6-7 using aq. HCl. The residue was filtered and dried. The yellow powder was re-dissolved in hot THF and then reprecipitated by adding an excess of toluene, and the residue was filtered and washed with toluene and then with acetone to give a pale-yellow powder (0.1 g, 51 %).

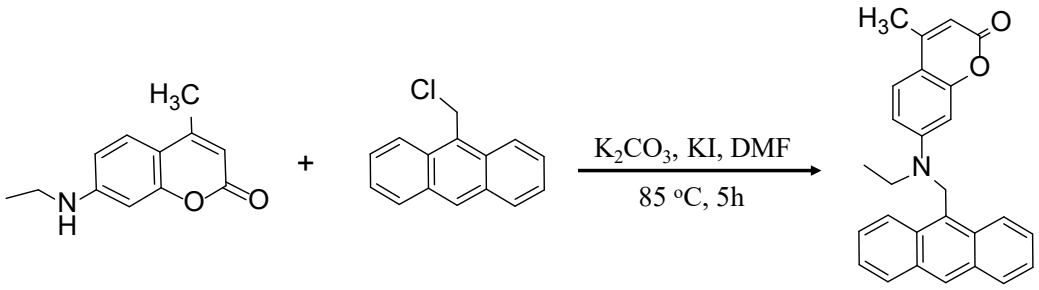

Scheme 2.6. A scheme for synthesis of **S2**.

The compound was characterized by recording the ^{1}H NMR spectrum in $CDCl_3$.

^{1}H NMR ($CDCl_3$) 500 MHz

δ= 8.52 (s, 1H; Ar-H), 8.14-8.16 (d, 2H; Ar-H), 8.05-8.07 (d, 2H; Ar-H), 7.55-7.48 (m, 5H; Ar-H), 6.95-6.98 (dd, 1H; Ar-H), 6.91-6.92 (d, 1H; Ar-H), 6.05 (s, 1H; allylic), 5.37 (s, 2H; N-CH_2), 3.06-3.10 (q, 2H; N-CH_2), 2.42 (s, 3H; CH_3), 0.77-0.80 (t, 3H; CH_3)

2.1.5.3 Synthesis of 6-[9-(methylanthryl)(ethyl)amino)-9-(ethoxycarbonyl)phenyl)-2,7-dimethyl-xanthen-3-ylidene)ethanaminium chloride (S3)

Rhodamine 6G-Anthracene conjugate, **S3** was reported as an efficient fluorescence sensor for $^1O_2$.[14] I prepared **S3** by a simple reaction.

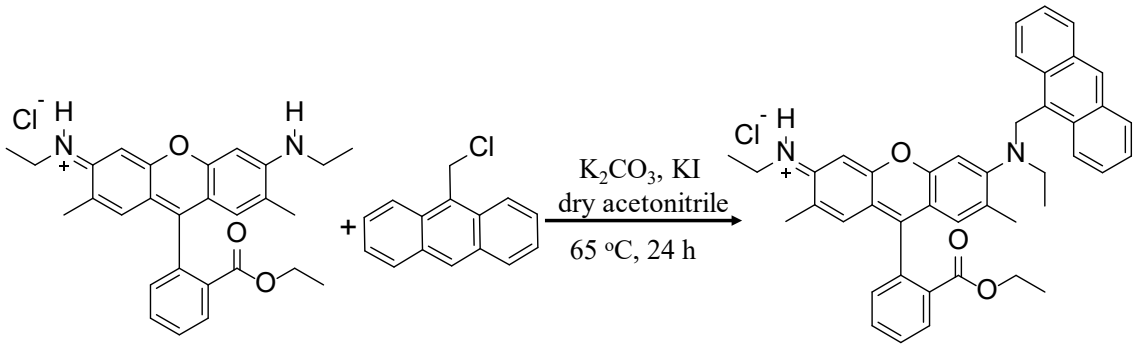

Scheme 2.7. Synthetic scheme of **S3**.

I dissolved Rhodamine 6G (1 g, 2 mmol) and 9-chloromethylanthracene (0.47 mg, 2 mmol) in 300 mL of dry acetonitrile. Then, K_2CO_3 (2.7 g, 20 mmol) and KI (1g, 6 mmol) were added to the solution, and this reaction mixture was stirred at 65 °C for 24 h. The reaction mixture was cooled to room temperature and excess water was added. The reaction mixture was extracted using dichloromethane (4×50). The organic layer was dried over $MgSO_4$ and the solvent was evaporated. The product was purified by silica-gel chromatography using a mixture (1:20, v/v) of methanol and chloroform as the eluent. **S3** was obtained as a purple powder. (100 mg, 7 %). **S3** was characterized by recording the ^{1}H NMR spectrum.

^{1}H NMR (dimethylsulphoxide-d6) 500 MHz

δ= 8.65 (s, 1H; Ar-H), 8.40-8.38 (d, 2H; Ar-H), 8.27-8.29 (d, 1H; Ar-H), 8.12-8.13 (d, 2H; Ar-H), 7.93-7.96 (t, 1H; Ar-H), 7.85-7.89 (t, 1H; Ar-H), 7.79 (s, 1H; Ar-H), 7.52-7.58 (m, 5H; Ar-H), 7.05 (s, 1H; Ar-H),), 6.98 (s, 1H; Ar-H), 6.95 (s, 1H; Ar-H), 5.56-5.64 (q, 2H; N-CH_2) , 3.95-4.01 (q, 2H; O-CH_2), 3.59-3.63 (q, 2H; N-CH_2), 3.00-3.06 (q, 2H; N-CH_2), 2.17 (d, 6H; CH_3), 1.28-1.31 (t, 3H; CH_3), 0.87-0.90 (t, 3H; CH_3). 0.82-0.85 (t, 3H; CH_3).

2.2 Methods

2.2.1 Nuclear magnetic resonance spectroscopy (NMR)

NMR spectroscopy is a common spectroscopic characterization technique used to elucidate the structure of organic compounds. The working principle of NMR spectroscopy is based on the absorption of radiofrequency by nondegenerate nuclear spin levels. In the presence of an applied magnetic field, the spin states of the nuclei are not equal. When an external magnetic field is applied, the nucleus with a spin angular momentum attempts to precess about its own axis with an angular frequency called *Larmor frequency*, which is linearly proportional to the strength of the applied magnetic field. This precession creates an oscillating electric field with the same frequency. The radio waves with the same frequency can stimulate absorption in the spin energy levels. This resonance condition is monitored by sweeping the magnetic field in the NMR spectrometer.[15] In this work, NMR measurements were performed using an Agilent Unity INOVA 500 spectrometer.

2.2.2 Electrospray ionization mass spectroscopy (ESI-MS)

ESI-MS is the most convenient method performed for characterization of a broad spectrum of chemicals. In ESI-MS studies, the sample dissolved in a polar solvent is sprayed through an electrospray needle maintained at a high electrical potential. The droplets are introduced to a high vacuum region through an orifice or a skimmer. In case of positive ion mode, the electrospray needle is maintained at a high positive potential with respect to the vacuum orifice. The anionic species are attracted to the needle and cationic species cumulate at the meniscus surface. When the positive charge at the surface starts repelling, the liquid surface will expand apart from the orifice surface, forming a cone-shaped liquid surface. Collision induced dissociation helps in breaking up solvent clusters and formation of the fragment ions, which is subsequently detected.[16] In this work, ThermoFisher Scientific Exactive was used for mass analysis.

2.2.3 Fourier-transform infrared (FTIR) spectroscopy

Infrared spectroscopy is an eminent spectroscopic tool predominantly used for the structural elucidation by monitoring the molecular vibration pattern. The absorption of infrared radiation with a specific wavelength causes the excitation of molecules to higher vibrational states. IR spectroscopy exploits the vibrational transitions in molecules caused by the absorption of infrared frequency. By analyzing the corresponding IR absorption region, information regarding stretching and bending vibrational motions of bonds can be acquired. The IR radiation from the source is allowed to pass through an interferometer. The radiations expelled from the interferometer is allowed to pass through the sample. The sample can either transmit or reflect the light which is subsequently detected by the detector. The signals are amplified and converted into the digital format and transferred for Fourier transformation. [17] In this work, I used a JEOL FT/IR 660Plus spectrometer for IR spectroscopic studies.

2.2.4 Cyclic voltammetry (CV)

Cyclic voltammetry is a simple and extensively used electrochemical technique for comprehensive analysis of a redox process. Generally, this technique is adopted to determine redox potential, electrochemical reversibility of an electroactive analyte and the information regarding the kinetic and thermodynamic parameters, and the effect of the media on the redox activity. A simple potentiostat setup with a three-electrode system immersed in the analyte solution containing non-reactive electrolyte has been used for the cyclic voltammetry analysis. The electrochemical reaction occurs at the electrochemically inert *working electrode*. In order to prevent the polarization of the electrode, the dimension of the electrode usually kept at a lower dimension. A reference electrode maintains the calibration of the applied potential. The potential at the *working electrode* is continuously monitored with respect to the *reference electrode*. A *counter electrode* is used to complete the electrical circuit with the working electrode, and the current between these two electrodes is systematically measured.

The basic principle of this technique comprises evaluation of the current response triggered as the result of a linear potential sweep applied to the working electrode. The potential is swept linearly with time from a starting potential where the analyte is stable.

Due to the action of potential, a current flow through the working electrode causes either oxidation or reduction of the electroactive species. Subsequently, the potential is swept back, causing electron transfer in the opposite direction, to obtain the analyte in the initial form. The potential window is recommended to maintain below the decomposition potential of the electrolyte used. A cyclic voltammogram can be created by plotting the potential versus the current response. Analysis of the cyclic voltammogram provides information such as the redox potential and the electrochemical reversibility/irreversibility of the analyte species during the potential sweep.[18] Differential pulse voltammetry is another electrochemical analytical method in which the time varying potential is applied in pulses. This technique is largely performed in electrochemical qualitative analysis owing to the improved sensitivity.

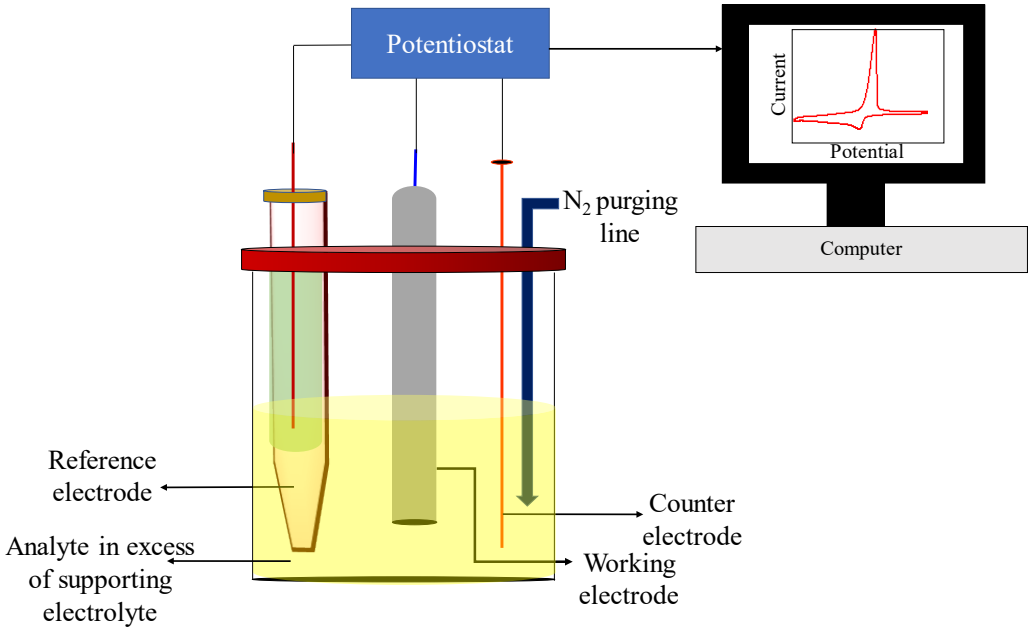

Figure 2.6. The schematic representation of the instrumentation of cyclic voltammetry/ differential pulse voltammetry set-up.

In this work, I used a three-electrode electrochemical cell setup coupled to a BAS CV50W electrochemical analyzer. A glassy carbon electrode was used as the working electrode. A platinum wire was employed as the counter electrode. The reference electrode was Ag/AgCl (sat. KCl) electrode. 0.1 M (*n*- Bu)$_4$NPF$_6$ (TBAPF$_6$) dissolved in dry DMF or 0.1 M phosphate buffer was used as the supporting electrolyte. All potentials are referenced to the ferrocene/ferrocenium couple (Fc/Fc$^+$) as the internal standard. CVs

were recorded at the scan rate of 0.1 V/s, and DPVs were monitored at the pulse amplitude of 0.05 V, the pulse width of 0.05 s, and the pulse period of 0.2 s. All solutions were deaerated for 15 min by nitrogen gas purging prior to the electrochemical measurements.

2.2.5 Density functional theory calculations

DFT is one of the extensively used *ab initio* calculation technique for studying the structure of atoms, molecules and crystals, and predicting the electronic energy levels, electron density and quantum mechanical states of a periodic system. This method finds enormous applications in the field of geoscience, computational physics, computational chemistry.[19] In this work, geometries of the molecules were optimized using the Gaussian 09 Revision D.01 program[20] with the B3LYP [21] functional with the D3 version of Grimme's dispersion with the original D3 damping function[22]. The 6-31G(d) [23] basis set was used for the simulations.

2.2.6 Steady-state absorption spectroscopy

Absorption spectroscopy is a non-destructive spectroscopic technique, largely employed in chemistry and biology. The common use of this technique comprises the determination of the concentration and spectral parameters of an analyte. The photon absorption in the UV-Vis region in a light-absorbing material, a chromophore, proceeds with the excitation of an electron from the highest occupied molecular orbital (HOMO) to the lowest unoccupied molecular orbital (LUMO). The photon absorption is also associated with the involvement of rotational and vibrational energy levels. Thus, the total energy absorbed by the molecule is considered to be the sum of the individual contribution. According to the Franck-Condon principle, the electronic excitation occurs in ultrafast time scale impelling change in the geometry during the optical excitation (molecular vibrational motion is very slow). In other words, the internuclear distance remains intact during the electronic relocation event. Hence, the electronic transitions are always represented as a straight line, which is termed as vertical or Frank-Condon transition. The intensity of photon absorption relies on the population of the excited state, which in turn depends on the Frank-Condon factor.

The absorption spectrometer is developed based on the Beer-Lambert-Bouguer Law. According to the Beer-Lambert-Bouguer Law, the absorbance of a compound in a

solution is linearly related to the concentration and thickness of the solution. $A = c \varepsilon l$. Where, c is the concentration of the analyte (mol L^{-1}), l is the optical pathlength in centimetre and ε is the molar extinction coefficient (M^{-1} cm^{-1}). Absorption spectroscopy is extensively used for both qualitative and quantitative analysis. This technique is largely applied for detection of the impurities, structural elucidation, chemical kinetics and in pharmaceutics.

The basic construction of the absorption spectrometer is given in Figure 2.7. Generally, a combination of Deuterium lamp and a Tungsten lamp covering 190-900 nm wavelength region is used as the light source. When the sample solution is sequentially excited with monochromatic radiation, the light-absorbing material in the solution, partly absorb the light and the spectrometer will record the transmitted light. The transmittance is recorded as the ratio of transmitted light over incident light. [24] In this research work, I used an EVOLUTION220 (Thermo Fisher Scientific) UV-Visible absorption spectrometer for steady-state absorption measurements.

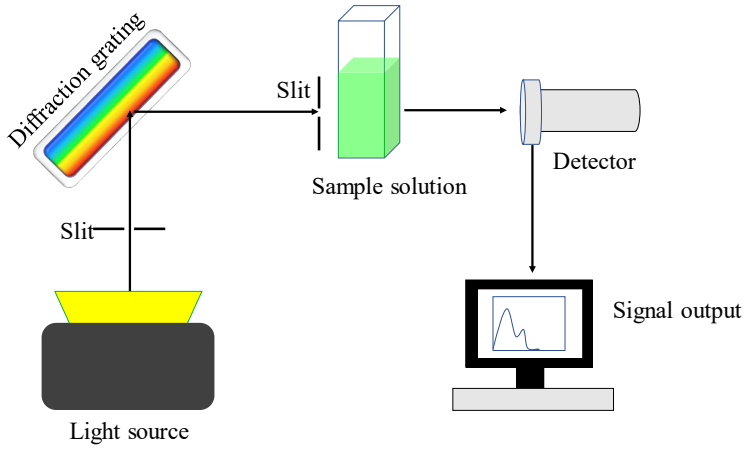

Figure 2.7. A diagram representing the basic configuration of an absorption spectrometer.

2.2.7 Transient absorption spectroscopy

Transient absorption spectroscopy is a time-resolved technique used to study ultrafast excited-state processes. Both the kinetic as well as mechanistic features of a photoinitiated process can be extracted using this method. This spectroscopic technique is also known as pump-prob spectroscopy owing to utilization of two sets of pulses of radiations. This technique is largely applied to study the photosynthesis-related phenomenon and kinetics

of enormous ultrafast photoinitiated activities. The analysis is initiated with the pump pulse; a fraction of molecules is excited to the higher energy state. Subsequently, the transient state formed by the action of pump pulse is irradiated by the probe pulse (with comparatively less intensity) with a delay time τ. The pulse width of the pump pulse is recommended to be shorter than the lifetime of the transient species. Here, a difference absorption spectrum is constructed. In other words, the difference in absorbance of excited state and the ground state species is calculated, and the ΔOD obtained is plotted as a function of τ and wavelength, λ.

TA spectrum is usually composed of three types of signals. First one is ground state bleach. The action of pump pulse causes the excitation of a fraction of molecules causing a deficiency in the number of ground-state species producing a negative signal in the TA spectrum, which is commonly referred to as *ground-state bleach*. There is a possibility of depopulation of the excited-state species when the probe pulse is passed through the sample solution giving a negative signal termed as *stimulated emission*. The stimulated emission spectral features resemble the fluorescence spectrum of the sample. The action of pump pulse leads to the excitation of excited state species to higher energy levels. The action of a certain wavelength triggers the absorption as mentioned above. The positive signal obtained is called as *excited-state absorption* or *induced absorption.*[25]

In this research work, the nanosecond time-resolved transient absorption measurements were carried out using the laser system NanoSpeK TSP-2000 (Unisoku Co., Ltd., Osaka, Japan). A solution containing a sample was excited by a Panther OPO pumped by a Nd:YAG laser (Continuum SLII-10, 4-6 ns fwhm), and the photodynamics were monitored by continuous exposure to a Xenon lamp (150 W) as a probe light and a photomultiplier tube (Hamamatsu 2949) as a detector. The instrument response function (IRF) for this system is less than 10 ns (ca. 9 ns).

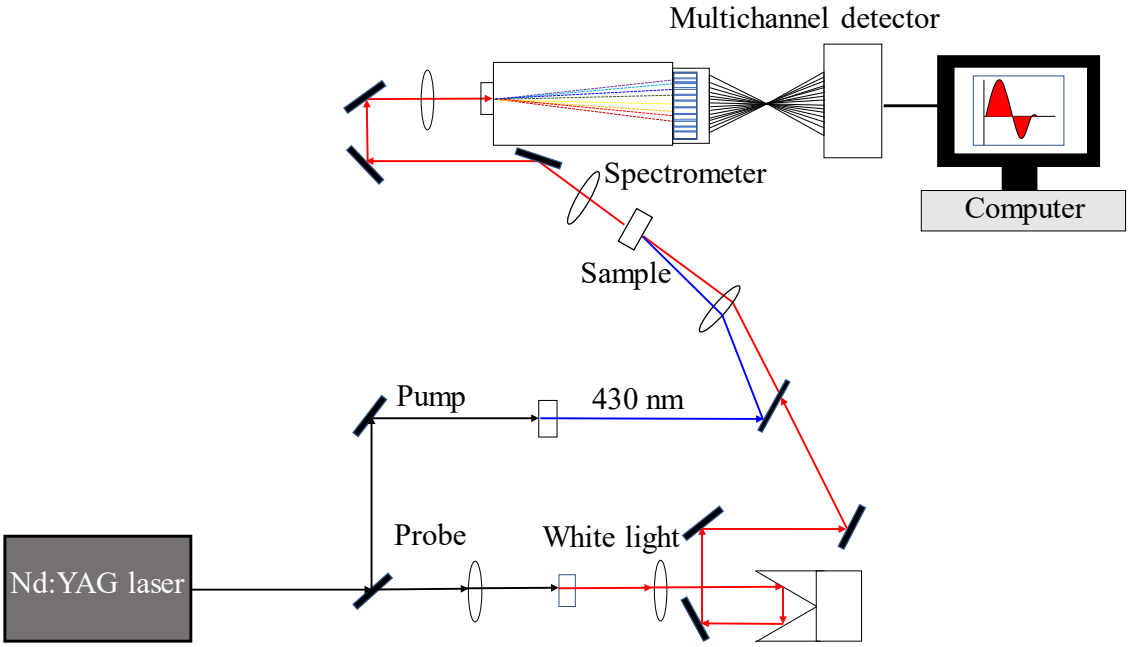

Figure 2.8. A diagram of the basic configuration of the transient absorption spectroscopic set-up.

2.2.8 Steady-state fluorescence spectroscopy

Fluorescence spectroscopy is a simple and sophisticated spectroscopic technique broadly used for characterization and detection of analytes and studying their molecular environment. Scientists largely extracted the advantage of this method in chemistry, biology, medical science, and forensic science. Here, the sample is excited with a continuous beam of light to the higher excited state, and the emission from the fluorophore is recorded. The excited state phenomena can be comprehensively explained based on Jablonski diagram.

According to Boltzmann distribution, most of the molecules lie in the lowest vibrational state in the ground state. The photon absorption promotes the electron to higher excited electronic states, and this process typically happens in 10^{-15} - 10^{-16} s. The excited electron eventually tries to dissipate the excitation energy. There are two modes of relaxation, radiative and non-radiative decay. Vibrational relaxation and internal conversion are the non-radiative modes. During vibrational relaxation, the molecule will reach to the lowest vibrational level of a particular excited electronic state by dissipating the excitation energy to its vibrational modes or to the adjacent molecules. This kind of

relaxation occurs within ~10^{-14}-10^{-12} s time scale. The electron in the higher electronic level can relax into the lower one with the same spin multiplicity by internal conversion within ~ 10^{-12} s. Internal conversions are escalated when there is appreciable overlap between the vibrational levels of two electronic states. The intersystem crossing involves a transition between the isoenergetic vibrational level of one electronic level to another with different spin multiplicity. This transition is stated as spin forbidden due to lack of conservation of the spin angular momentum, making the transition much slower (~10^{-8} s). However, the presence of heavy-atoms can enhance the spin-orbit coupling, thereby improving the rate of the intersystem crossing.

The excitation energy can be expelled by emitting a photon in a radiative manner. The radiative relaxation from the excited singlet state to the different vibrational levels of the ground state is termed as fluorescence (~10^{-11}-10^{-8} s). According to Kasha's rule, the luminescence occurs from the lowest vibrational state of the excited electronic level, causing Stokes-shift. The internal conversions and vibrational relaxations are responsible for this energy loss.[26, 27]

The general configuration of a fluorescence spectrometer is given in Figure 2.9. An ozone-free Xenon lamp is used as the light source. The UV and visible continuum of from the light source is passed through a monochromator to avail the required wavelength for exciting the sample. The two slits situated along with the monochromator at the entrance and exit is to control the bandwidth and the slit width of the light. After the irradiation of the sample, there would be subsequent fluorescence which is directed to the emission monochromator placed at 90^{o} and finally reaches the detector. In this research, Hitachi F4500 fluorescence spectrometer was used for the fluorescence studies.

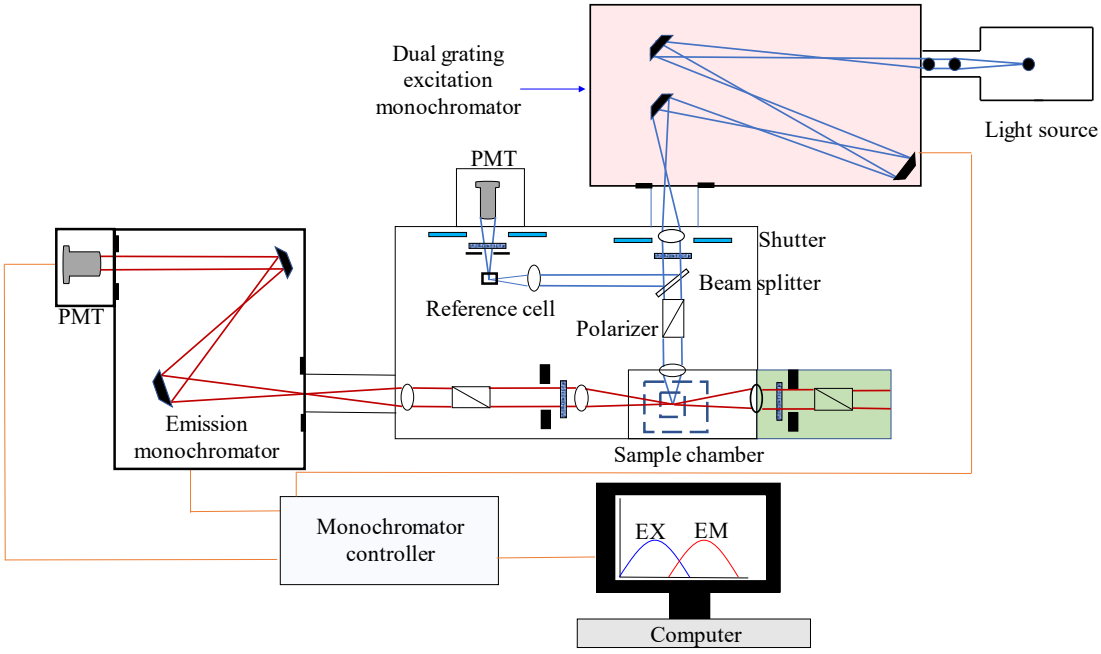

Figure 2.9. A diagram of the configuration of a fluorescence spectrometer. The diagram is constructed according to Ref 27.

2.2.9 Electron paramagnetic resonance (EPR) spectroscopy

Electron paramagnetic resonance spectroscopy is a well-sophisticated technique applied in inspecting the environment of the unpaired electron in various chemical species, for instance, organic free radicals or unpaired electron in a transition metal complex. EPR spectroscopy finds extensive applications to the study of the electronic structure, the triplet states, defects in semiconductors and reaction kinetics and mechanism. This method is based on the absorption electromagnetic radiation by a chemical species with an unpaired spin in the presence of an applied magnetic field.

When an electron is placed in a magnetic field, the projection of the magnetic moment on the axis is governed by this external magnetic field, and it assumes two discrete values $m_s = +1/2$ and $m_s = -1/2$. The energy gap between these levels are governed by the strength of the applied magnetic field, and when an electromagnetic field with the photon energy corresponds to the energy gap between the two discrete spin energy levels is applied, the transition between the two spin-state occurs. The interaction between the magnetic dipoles of the unpaired electron and the neighboring nuclei causes the splitting of the

single EPR line to multiple lines due to the *hyperfine splitting,* and this interaction helps to get information regarding the types and numbers of the interacting nuclei.

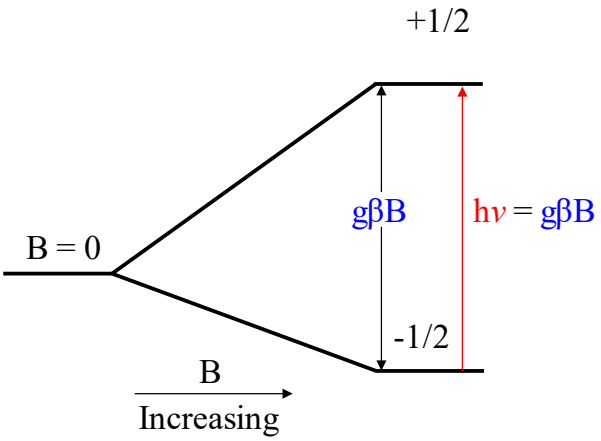

Figure 2.10. A diagram showing the Zeeman energy level splitting induced by an external magnetic field and the transition between the discrete energy levels triggered by microwave radiation. β is the Bohr Magneton, g is a characteristic value for a species, and B is the strength of the applied magnetic field.

The fundamental configuration of an EPR spectrometer is shown in Figure 2.11. The microwave system comprises a source and resonator and a detector. The magnetic system encompassed the power supply and the field controller. The modulation and the phase-sensitive detection system is connected to the data display and manipulation system.

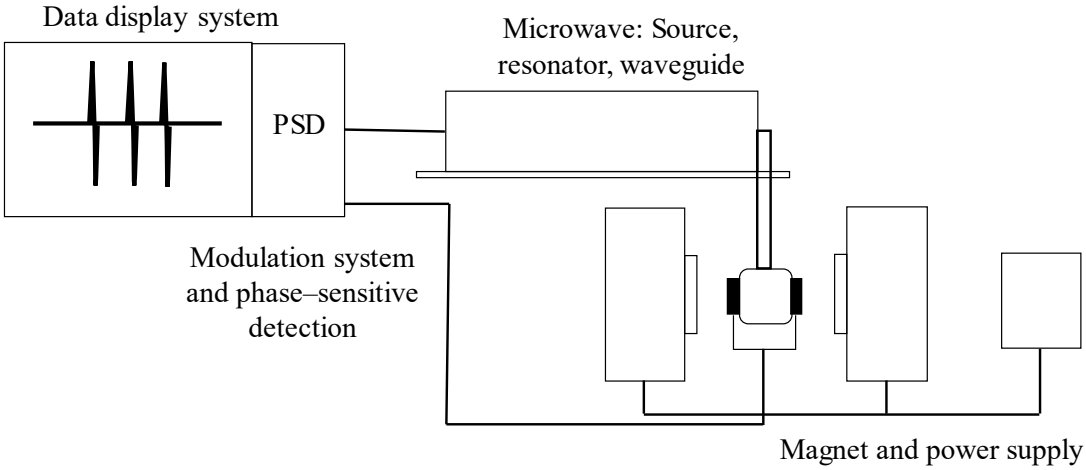

Figure 2.11. A diagram of fundamental design of a CW- EPR spectrometer. The diagram is constructed according to Ref 28.

The most frequently used EPR set up is of X band with a microwave frequency of ~9.5 GHz and applied magnetic field of 0.3T.[28] In this research work, continuous-wave-EPR measurements were carried out using a Bruker EMXplus spectrometer.

2.3 Optical set-up for photothermal effect studies

Photothermal effect (PTE) exhibited by 9-substituted acridinium compounds was evaluated using a homemade optical set-up. The light sources were a Xenon lamp with a long pass filter (>480 nm nm at 440 mW cm^{-2}) and a blue light emitting diode (LED) (420-440 nm, 140 mW cm^{-2}). The absorbancies of the sample solutions were set to 1.00 at 430 nm and taken in a 2 mm-path glass cuvette. Sample solutions were irradiated by the individual light or by simultaneously both the light sources on the same face of the cuvette to achieve synchronous excitation of the molecule by both the blue and yellow lights. A digital thermometer was used to analyze the temperature response, and the sensor was dipped in the sample solution meticulously by avoiding the direct illumination. The temperature response during the photo illumination was recorded for each 15 s. Each experiment was repeated 4 times to avail the standard deviation.

References

1. Kuznetsov, A.M.; Ulstrup, J. *Electron transfer in chemistry and biology;* Wiley: Chichester, **1999**.
2. De Silva, A. P.; Moody, T. S.; Wright, G. D. Fluorescent PET (Photoinduced Electron Transfer) Sensors as Potent Analytical Tools. *Analyst.* **2009**, *134* (12), 2385–2393.
3. Hardin, B. E.; Snaith, H. J.; McGehee, M. D. The Renaissance of Dye-Sensitized Solar Cells. *Nat. Photonics.* **2012**, *6* (3), 162–169.
4. Rehm, D.; Weller, A.; D. Rehm, A. Weller. Kinetics of Fluorescence Quenching by Electron and H-Atom Transfer. *Isr. J. Chem.* **1970**, 8 (2), 259-271.
5. Yao, Z.; Zhang, M.; Wu, H.; Yang, L.; Li, R.; Wang, P. Donor/Acceptor Indenoperylene Dye for Highly Efficient Organic Dye-Sensitized Solar Cells. *J. Am. Chem. Soc.* **2015**, *137* (11), 3799–3802.
6. Song, X.; Chen, Q.; Liu, Z. Recent Advances in the Development of Organic Photothermal Nano-Agents. *Nano Res.* **2015**, *8* (2), 340–354.
7. Jung, H. S.; Verwilst, P.; Sharma, A.; Shin, J.; Sessler, J. L.; Kim, J. S. Organic Molecule-Based Photothermal Agents: An Expanding Photothermal Therapy Universe. *Chem. Soc. Rev.* **2018**, *47* (7), 2280–2297.
8. Takano, Y.; Hanai, E.; Imahori, H. Photoinduced Electron Transfer Reaction in Mitochondria for Spatiotemporal Selective Photo-Oxidation of Lipids by Donor/Acceptor Linked Molecules. *Nanoscale* **2017**, *9* (45), 17909–17913.
9. Naoki, U.; Kumi, T.; Yasuteru, U.; Kazuya, K.; Tsunehiko, H.; Tetsuo, N. Novel Fluorescent Probes for Singlet Oxygen. *Angew. Chemie Int. Ed.* **1999**, *38* (19), 2899–2901.
10. Tanaka, K.; Miura, T.; Umezawa, N.; Urano, Y.; Kikuchi, K.; Higuchi, T.; Nagano, T. Rational Design of Fluorescein-Based Fluorescence Probes. Mechanism-Based Design of a Maximum Fluorescence Probe for Singlet Oxygen. *J. Am. Chem. Soc.* **2001**, *123* (11), 2530–2536.
11. Kim, S.; Fujitsuka, M.; Majima, T. Photochemistry of Singlet Oxygen Sensor Green. *J. Phys. Chem. B* **2013**, *117* (45), 13985–13992.

12. Kim, S.; Tachikawa, T.; Fujitsuka, M.; Majima, T. Far-Red Fluorescence Probe for Monitoring Singlet Oxygen during Photodynamic Therapy. *J. Am. Chem. Soc.* **2014**, *136* (33), 11707–11715.
13. Kohara, R.; Yuyama, K.; Shigeri, Y.; Biju, V. Blue-Emitting Electron-Donor / Acceptor Dyads for Naked- Eye Fluorescence Detection of Singlet Oxygen. *ChemPhotoChem.* **2017,** 1(7), 299-303.
14. Sun, M.; Krishnakumar, S.; Zhang, Y.; Liang, D.; Yang, X.; Wong, M. W.; Wang, S.; Huang, D. Singlet Oxygen Probes Made Simple: Anthracenylmethyl Substituted Fluorophores as Reaction-Based Probes for Detection and Imaging of Cellular 1O2. *Sensors Actuators, B Chem.* **2018**, *271* (May), 346–352.
15. Pavia, D.L.; Lampman, G.M.; Kriz, G.S.; Vyvyan, J.A. *Introduction to spectroscopy*; Cengage Learning, **2008**.
16. Pramanik, B.N.; Ganguly, A.K.; Gross, M.L. *Applied electrospray mass spectrometry: practical spectroscopy series*; CRC Press, 2002.
17. Möllmann, K. P.; Vollmer, M. Fourier Transform Infrared Spectroscopy in Physics Laboratory Courses. *Eur. J. Phys.* **2013**, *34* (6).
18. Compton, R.G.; Banks, C.E. *Understanding voltammetry*; World Scientific, 2011.
19. Argaman, N.; Makov, G. Density Functional Theory: An Introduction. *Am. J. Phys.* **2002**, *68* (1), 69–79.
20. Frisch, M.J.; Trucks, G.W.; Schlegel, H.B.; Scuseria, G.E.; Robb, M., Cheeseman, J.R.; Scalmani, G.; Barone, V.; Mennucci, B.; Petersson, G.A.; Nakatsuji, H. *Gaussian 09, Revision D. 01, Gaussian. Inc*; Wallingford, CT, 2009.
21. Becke, A. D. Thermochemistry. III. The Role of Exact Exchange. *J. Chem. Phys.* **1993**, *98* (October), 5648–5652.
22. Grimme, S.; Antony, J.; Ehrlich, S.; Krieg, H. A Consistent and Accurate Ab Initio Parametrization of Density Functional Dispersion Correction (DFT-D) for the 94 Elements H-Pu. *J. Chem. Phys.* **2010**, *132* (15).
23. Petersson, G. A.; Mohammad A, A.-L. A Complete Basis Set Model Chemistry. II. The Total Energies of Open-Shell Atoms and Hydrides of the First-Row Atoms. *J. Chem. Phys.* **1991**, *9* (September), 6081–6090.
24. Albani, J. R. Absorption Spectroscopy Theory. *Princ. Appl. Fluoresc. Spectrosc.* **2008**, 1–12.

25. Berera, R.; van Grondelle, R.; Kennis, J. T. M. Ultrafast Transient Absorption Spectroscopy: Principles and Application to Photosynthetic Systems. *Photosynth. Res.* **2009**, *101* (2–3), 105–118.
26. Lakowicz, J. R. ed. *Principles of fluorescence spectroscopy*; Springer Science and Business Media, 2013.
27. Naresh, K. Applications of fluorescence spectroscopy. *J. Chem. Pharm.* ***2014,*** 974, 2115.
28. Cazes, J. ed. *Analytical instrumentation handbook*; CRC Press, 2004.

Chapter 3

Intramolecular Electron Transfer for Photothermal Energy Conversion

Abstract: In this chapter, the photothermal effect exhibited by 9-substituted acridinium based electron D-A dyads is examined at different pH. One of the compounds, 9-(2,6-dimethyl-4-hydroxyphenyl)-10-methylacridinium chloride (**Acr1**) shows excellent photothermal effect. The photothermal effect in 9-(2,6-dimethyl-4-hydroxyphenyl)-10-methylacridinium chloride by irradiation with blue light (420-440 nm) is further enhanced by the simultaneous irradiation of blue light and yellow light (480-700 nm). The enhanced photothermal effect is attributed to the photoinduced betaine generation. The betaine absorbs longer wavelength light than the dyad. The excellent photostability and recyclability makes the dyad-betaine combination promising for efficient photothermal energy conversion. The photoinduced betaine generation and energy conversion are studied using steady-state and transient absorption spectroscopy.[1]

3.1 Introduction

The conversion of light energy to thermal energy attracted significant attention in the field of photothermal therapy (PTT) and solar-energy harvesting. The photothermal effect (PTE) refers to the production of heat by the action of electromagnetic radiation. Broad range of radiation has been used to demonstrate PTE such as X-ray, ultraviolet light, visible light, infrared light, microwave radiation and radio waves. However, the utilization of visible light and infrared frequency attract much attention to solar energy conversion and PTT. Besides, PTE finds diverse application in photothermal-mediated material probing, processing and destruction, thermal imaging, sea water desalinization and in fundamental science as in photothermal spectroscopy.[2]

3.1.1 Photothermal energy conversion in photothermal therapy

The utilization of controlled temperature increments in the treatment of cancer began in the earliest of the 19th century. During the localized application of temperature, cells die by the denaturation of the protein and the disruption of the cell membrane. The thermal localized photothermal therapy (PTT) comprises the hyperthermia region (41 ^{o}C-48 ^{o}C) to the region of irreversible injury (48 ^{o}C-60 ^{o}C). The application of temperature above 60 ^{o}C leads to the instantaneous coagulation of proteins and the drastic activation of cell death by necrosis. The promising classes of nanomaterial-based photothermal agents comprise metal nanoparticles, carbon nanostructures, and quantum dots.[3]

Metal nanomaterials (MNPs) have emerged into the superior class of heat generators. The heat generation efficiency of metal nanoparticles is governed by the wavelength of the light, and the size and shape of the particle. Owing to this fact, metal nanoparticles are made to work in the first biological window (700 nm - 800 nm) and second biological window (1000 nm - 1400 nm), where the deep penetration of laser beam and selective excitation of the cells/tissue is possible. The working principle of MNPs relies on the localized surface plasmon resonance (LSPR) effect.[3] LSPR emanates when the light interacts with the surface of metal nanoparticles, and the wavelength of light is less than the size of the particle. The intense interaction between the electric field of the incident light, and the free electrons in the conduction band of the MNP lead to collective and coherent oscillation along the direction of polarization of the electric field. The resonance between the frequency of the radiation and the oscillation leads to constructive interference and strong absorption of the radiation. The common MNPs employed in PTT are gold nanoparticles and its analogues such as nanorods, nanocages, nano prisms, and even nanostars. Besides, silver nanomaterials and iron-based nanomaterials have been intensively studied and applied for PTT.[3- 5]

Carbon-based nanomaterials have been developed into promising photothermal agents for PTT. This class of carbon-based materials comprises nanodiamonds, carbon nanotubes, graphene and graphene oxide, carbon dots, carbon nanohorns, and fullerene. Inherent biocompatibility of carbon strengthened the applicability of these materials to PTT. Even though carbon-based materials are known to be biocompatible, but the prolonged exposure causes toxic effects such as abnormalities in immune functions.[6]

The potential long-term toxicity, limited solubility, and low biodegradability of the exiting inorganic photothermal agents raised the demand for alternative materials. Organic compounds are an alternative class of photothermal agents comprising organic nanoparticles, organic polymers such as polyaniline, and nonfluorescent dyes with excellent NIR absorption. Organic PTT agents offer the possibility of cancer-targeting by modification of the structure of agents and efficient renal clearance with biodegradability. Organic PTT agents also render simultaneous cancer targeting, bioimaging, and PTT. NIR absorbing low fluorescent dyes are efficient candidates for PTT. This class of agents mainly comprises cyanine, phthalocyanines, croconaine, porphyrin, diketopyrrolopyrrol, and squaraines.[7] The advancement in PTT constitutes synergic PTT and chemotherapy or photodynamic therapy (PDT).[8,9]

3.1.2 Photothermal energy conversion in light harvesting

By considering the renewability of solar energy, its conversion into useful form attracted significant attention of scientists. The common strategies for solar energy conversion comprise the conversion into chemical energy (artificial photosynthesis) or electrical energy (photovoltaic devices). However, the inherent limitations associated with the conventional solar cells and the construction of complex antennae systems for artificial photosynthesis, raised the demand for an alternative method. Photothermal energy conversion is an excellent strategy for solar energy harvesting, which is applied to diverse applications such as thermophotovoltaics, solar-driven water vaporization for water purification, seawater desalinization, and water heaters. The conventional materials that have been used for photothermal energy conversion comprise plasmonic solar absorbers, carbon-based photothermal absorbers, and nonfluorescent dyes. Although the narrow absorption spectra of these materials restrain the efficient harnessing of the entire solar spectrum. Thus, in order to improve the absorption properties, for instance, the broadening of the absorption region of the photothermal agents, new strategies are needed.[10-12]

One of the methods to cover the solar spectrum is to extend the pi-conjugation structure in organic chromophores by the structural modification which involve lengthy synthetic procedure. The photodecomposition of the molecules is a major concern.

Photodecomposition may occur due to undesired generations of reactive species or uncontrolled redox reactions at the photo-excited states.[13] Therefore, significant efforts have been applied to tackle this issue, which is by designing rigid molecular frameworks or controlling the assembly at the molecular level. In this study, I am applying a novel approach to utilize a photogenerated species from a donor-acceptor linked molecule with high durability for the efficient use of light energy. As the molecular skeleton, I chose 9-position substituted acridinium moiety, which is intensively studied for photocatalysis and artificial photosynthesis because 9-position substituted acridinium-based electron D-A systems shows efficient electron transfer to form long-living CS states.[14,15]

3.2 Design and fundamental properties of electron donor-acceptor dyads

In this work, the PTE generated by a novel acridinium based electron D-A dyad, **Acr1** and two reference molecules, **Acr2** and **Acr3** is studied. The structures of the molecules are shown in Figure 3.1. The low reorganization energy for the electron exchange reactions exhibited by the acridinium ion makes it as an ideal electron acceptor candidate. The short linkage in between the donor and the acridinium acceptor part helps to decrease the solvent reorganization energy and thereby enhance the forward electron transfer process. The unique excited state properties exhibited by 9-mesityl-10-methyl acridinium[2] inspired me to synthesize the novel pH-responsive electron D-A dyad **Acr1**.

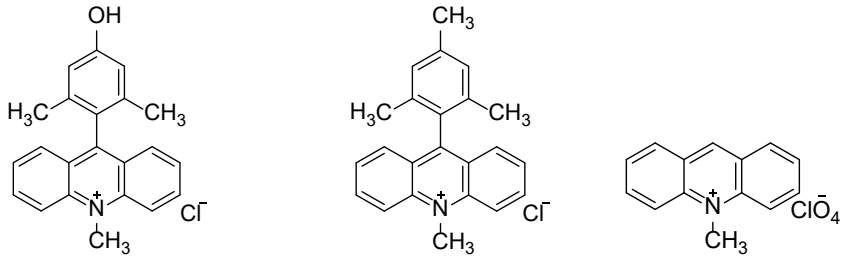

Figure 3.1. The structures of electron D-A dyads (**Acr1** and **Acr2**) and model compound (**Acr3**).

3.2.1 Density functional theory calculations

To study the molecular configuration and the orientation of the donor and acceptor moieties in these 9-substituted acridinium compounds, DFT analysis was applied. DFT calculation at UB3LYP-D3/6-31G* level of theory provided the highest occupied molecular orbital (HOMO) and lowest unoccupied molecular orbital (LUMO) configuration in the electron donor-acceptor dyads. The HOMO of **Acr2** is localized in the mesityl part, and the LUMO is localized in the acridinium part. The donor, mesityl group maintains an orthogonal symmetry to the acridinium in the conjugated state, keeping insignificant orbital interaction.[14,15] **Acr1** in the protonated form shows similar traits as that of **Acr2** with no delocalization of molecular orbitals (Figure 3.2). Thus, the orthogonal geometry of the donor and acceptor detains the possibility of ground-state charge transfer. However, once the molecule, **Acr1** gets deprotonated to produce the betaine form, **Acr1-betaine**, the molecular geometry changes drastically. In the betaine form, the donor and acridinium moieties are no longer orthogonal to each other. The dihedral angle is ~110^{o} and thereby the HOMO and LUMO are in the delocalized state. The delocalization of MO enhances the probability of charge transfer.

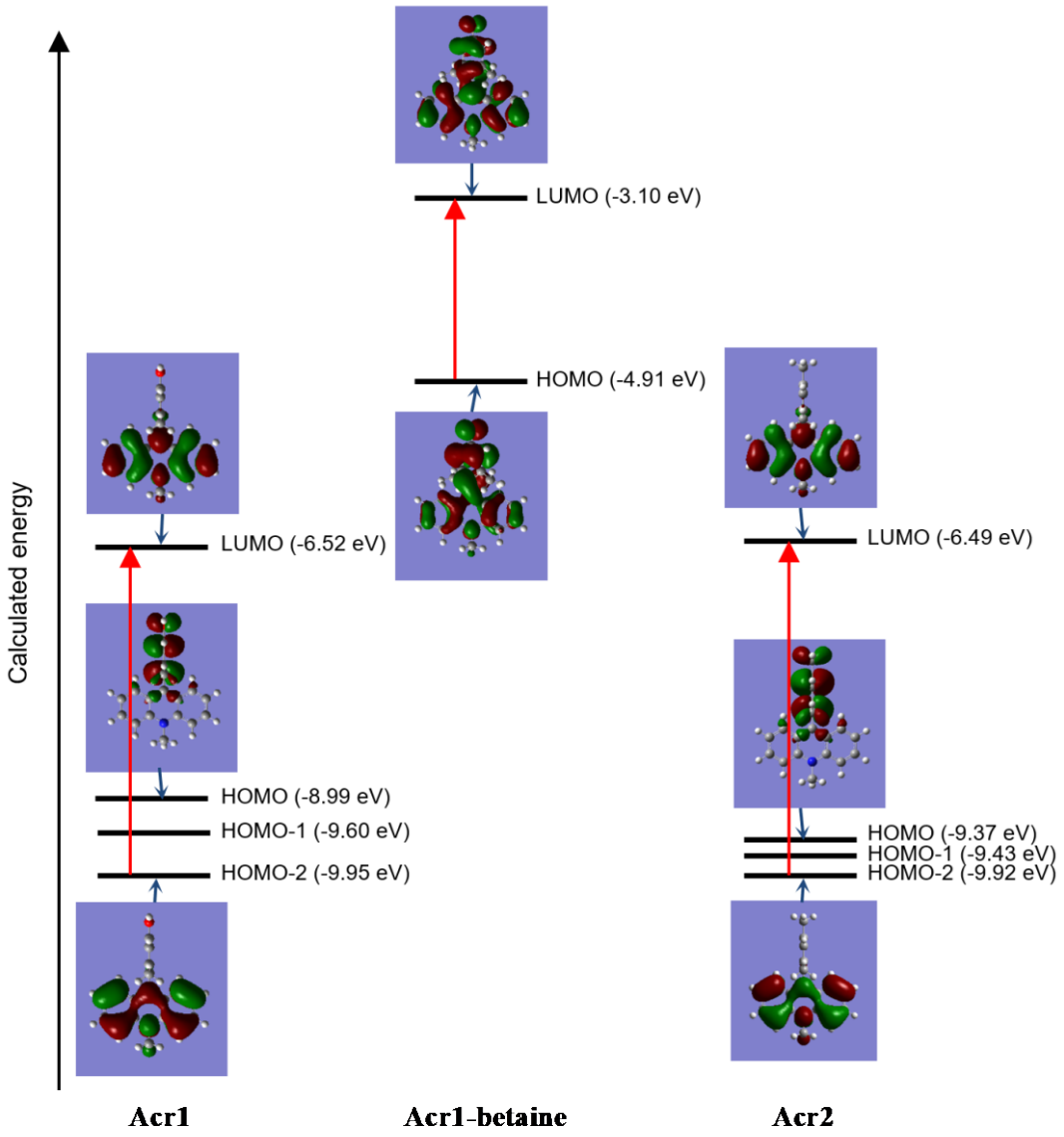

Figure 3.2. The HOMOs and LUMOs of **Acr1**, **Acr1-betaine** and **Acr2**, provided by the DFT calculation at UB3LYP-D3/6-31G* level of theory. The chloride anion is excluded for simplifying the calculations. Red arrows show the first singlet-singlet transition.

3.2.2 Cyclic voltammetry studies

To calculate the free energy of electron transfer from the donor, 3,5-dimethyl phenol to the photoexcited acridinium, the redox potentials of the donor and the acceptor were experimentally determined using cyclic voltammetry. Here, cyclic voltammograms (CVs) and differential pulse voltammograms (DPVs) were recorded at room temperature for 5 mM solutions of the samples dissolved in phosphate buffer at pH 7. Figure 3.3 shows CVs of the donor (3,5 dimethylphenol) and the acceptor (**Acr3**) respectively.

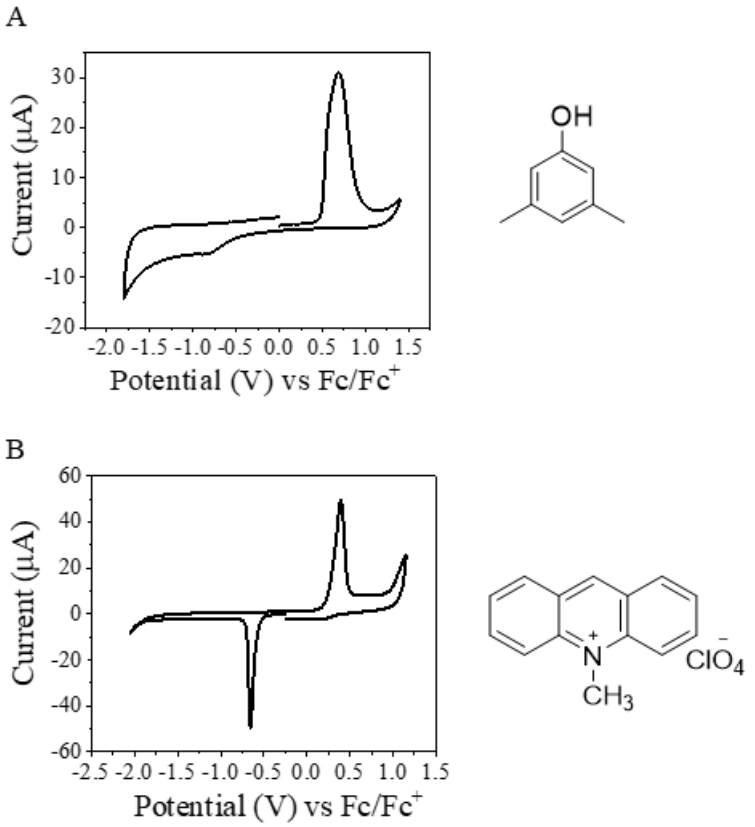

Figure 3.3. The CVs and structures of (A) 3,5-dimethylphenol and (B) **Acr3** in 0.1 M phosphate buffer at pH 7. The scan rate was set at 100 mV s^{-1}.

Then, thermodynamic feasibility of the electron transfer between the donor and acceptor units was verified by estimating the free energy change of the electron transfer according to eq. 1[16];

$$\Delta G_{et} = E(D^+/D) - E(A/A^-) - E_{00} - \frac{e^2}{\varepsilon d} \quad (1)$$

where, E_{ox} is the first oxidation potential of the donor moiety, and E_{red} is the first reduction potential of the acceptor, and $E_{0,0}$ is the zero-zero transition energy for excitation of the acridinium ion. The redox potentials of the compounds were determined by CV and DPV. The obtained redox potentials and the calculated free energy change of electron transfer are shown in Table 1. The free energy change for electron transfer between, 5-dimethylphenol and **Acr3** found significantly negative, which validate the thermodynamic feasibility of the PET.

Table 1. The first redox potentials of the electron donor and acceptor model compounds, E_{00} values, and the free energies of intermolecular electron transfer.

The first oxidation potential of the donor (V)	The first reduction potential of the acceptor (V)	E_{00} (eV)	Coulombic stabilization energy (eV)	ΔG (eV)
3,5-dimethylphenol 0.24	**Acr3** -0.56	2.69	0.52	-2.41

Values are given in volts relative to $Fc^{0/+}$ redox couple and were obtained from DPVs. Conditions: Glassy carbon electrode as the working electrode, the counter electrode was a platinum wire, and the reference electrode was Ag/Ag^+. The supporting electrolyte was 0.1 M phosphate buffer.

The DPV studies provided the redox potential of the electron donor and acceptor model compounds precisely. The zero-zero energy for the optical transition was estimated from the intersection point of absorption and fluorescence spectra of **Acr3**. The corresponding negative value obtained for the free energy of electron transfer verifies the possibility of electron transfer from 3,5-dimethylphenol to 10-methylacridinium by the photoexcitation of the acridinium part.

The feasibility of electron transfer was further verified at different pH by determining the redox potential of the constituent donor and acceptor in **Acr1**. To this purpose, the CVs of **Acr1** was monitored at pH 4.4, 7.4 and 9.1 respectively. The CVs

are shown in Figure 3.4. The first oxidation potential of the donor and the first reduction potential of the acceptor moieties are given in Table 2. The free energy change of the electron transfer between the donor and the acridinium moiety in the electron D-A dyad was calculated using eq.1. The negative value of free energy change of electron transfer verifies the feasibility of photoinduced electron transfer in **Acr1** at acidic, neutral and basic pH.

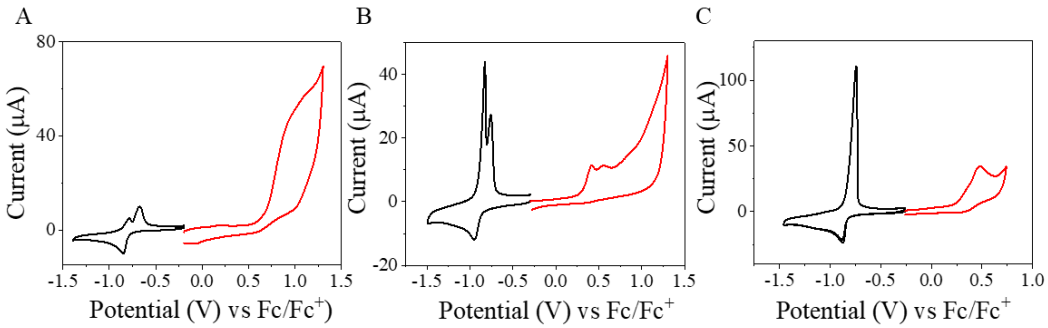

Figure 3.4. CVs of **Acr1** in 0.1 M phosphate buffer at (A) pH 4.4 and (B) pH 7.4 and C) pH 9.1. The scan rate was set at 100 mV s^{-1}.

Table 2. pH-dependent redox potentials of **Acr1** and free energy change of electron transfer.

pH	The first oxidation potential of the donor (V)	The first reduction potential of the acceptor (V)	E_{00} (eV)	Coulombic stabilization energy (eV)	ΔG (eV)
4.4	0.43	-0.59	2.69	0.52	-2.19
7.4	0.50	-0.60	2.69	0.52	-2.11
9.1	0.37	-0.57	2.69	0.52	-2.32

Values of redox potentials are given in volts relative to $Fc^{0/+}$ redox couple and were obtained from differential pulse voltammetry studies. Conditions: glassy carbon electrode as a working electrode, the counter electrode was a platinum wire and Ag/Ag^{+} as the reference electrode.

3.2.3 Steady-state absorption and fluorescence studies

The pH-dependent absorption and fluorescence spectra of **Acr1** is given in Figure 3.5. The absorption signal in the 350-450 nm region is mainly originated from the transition between the π energy levels within the acridinium part. However, a new band in ca. 450-700 nm region appeared at pH 12. The occurrence of this band in the longer wavelength region can be addressed in terms of formation of betaine form due to the deprotonation at higher pH. In DFT calculations, the HOMO and LUMO energy levels are delocalized over the entire molecular skeleton in the betaine (Figure 3.2). Hence, the new band can be attributed to the charge transfer (CT) band. **Acr1** significantly absorbs the light in the UV-blue region (extinction coefficient: 4.46 × 10^3 L mol^{-1} cm^{-1} at 430 nm), whereas **Acr1-betaine** absorbs the UV-blue light and the light between 480-700 nm. (extinction coefficient: 3.3 × 10^3 L mol^{-1} cm^{-1} at 430 nm, and 1.04 × 10^3 at 530 nm). The pH-dependent structural transformation was reversible (Scheme 3.1). The fluorescence of **Acr1** was drastically quenched compared to the model compound **Acr3** (Figure 3.5 B). The low fluorescence quantum efficiency of **Acr1** (φ_f= 0.001) can be attributed to the PET from the donor to the excited acridinium.

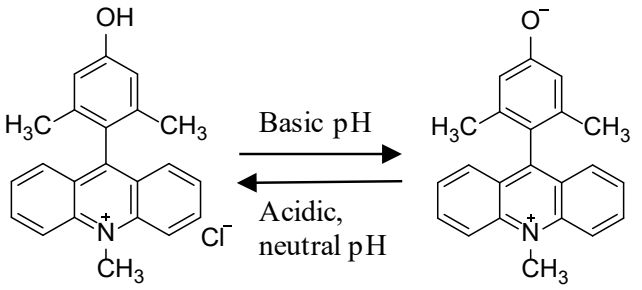

Acr1 **Acr1-betaine**

Scheme 3.1. pH-dependent structural transformation in **Acr1**.

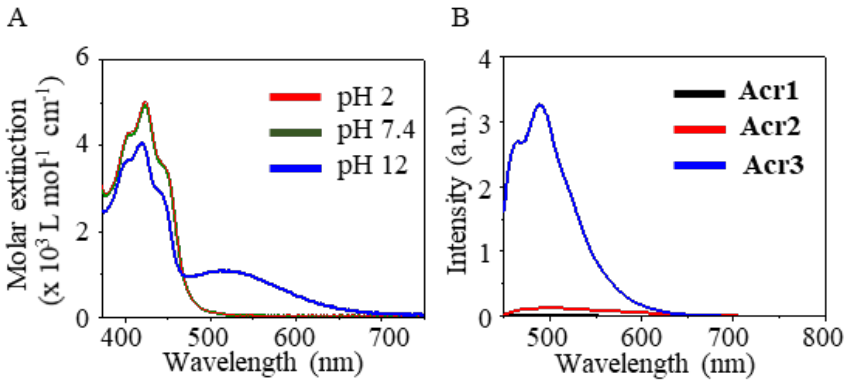

Figure 3.5. (A) pH dependent absorption spectra and (B) fluorescence spectra (λ_{ex}: 430 nm) of **Acr1** at pH 7.4.

In order to correlate the pH-dependent structural transformation and the effect of the substituent on the 9-position of acridinium, two reference molecules **Acr2** and **Acr3** were studied under identical conditions. The absorption spectra of the model compounds are shown in Figure 3.6 A. Both the compounds show similar absorption features. 9-position unsubstituted acridinium derivatives such as **Acr3** are more prior to the nucleophilic addition since the 9-position tends to be electron deficient. [17] As a result, the reaction of **Acr3** with OH^- leads to decomposition at pH 12. However, **Acr1** and **Acr2** were stable at pH 12. The stability is due to the hindrance around the 9-position of the acridinium moiety by the closely placed methyl groups in the ortho positions of benzene ring.[18]

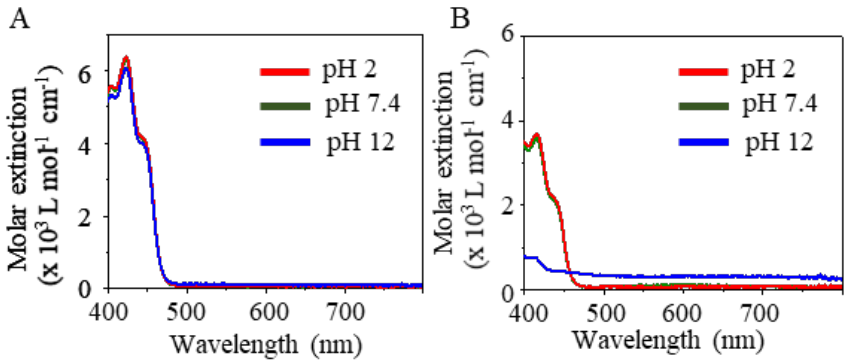

Figure 3.6. Absorption spectra of (A) **Acr2** and (B) **Acr3** at different pH.

3.2.4 Determination of the efficiency of electron transfer

The efficiency electron transfer (ϕ_{ET}) between an excited-state molecule and the redox partner can be estimated by knowing the fluorescence quantum yield of the excited-state molecule in the conjugated form and in the pristine form using equation 2.[19]

$$\phi_{ET} = 1 - \frac{\phi_f}{\phi_0} \qquad (2)$$

Where, ϕ_f is the fluorescence quantum yield of the 9-substituted acridinium based electron D-A dyad (**Acr1**) and ϕ_0 is the fluorescence quantum yield of the unsubstituted acridinium ion. The ϕ_{ET} corresponding to quantum efficiency of electron transfer from the the donor part to photoexcited acridium part in **Acr1** is estimated at 0.99 using equation 2. The high value of ϕ_{ET} of **Acr1** refers highly efficient photoinduced electron transfer.

3.2.5 Determination of pKa of Acr1

The electron D-A dyad **Acr1** undergoes reversible deprotonation to obtain the betaine form in a basic medium. Thus, it was necessary to find the pKa of the compound. UV-Vis absorption spectroscopy can be used to estimate the pKa value of a compound by monitoring absorbance at various pH. pKa value can be determined by plotting the absorbance value against the pH and can be determined as the pH value corresponding to half the maximum of absorbance.

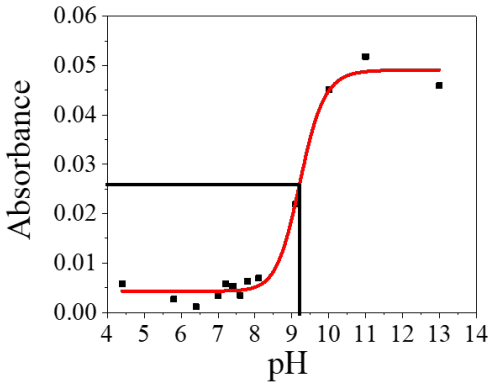

Figure 3.7. The plots of absorbance (510 nm) *vs* pH of the solutions (**Acr1**, 50 µM in phosphate buffer). The red curve represents the sigmoidal fitting.

Therefore, I recorded the absorbance spectra of **Acr1** in phosphate buffer solution at different pH and constructed a pH *vs* absorbance plot (Figure 3.7). The curve was fitted by the sigmoidal fitting. The pKa corresponds to the pH value at half the maximum absorbance which was determined at 9.2.

3.3 Transient absorption studies

To study the electron transfer kinetics and the excited-state processes comprehensively, the nanosecond transient absorption studies were carried out. Figure 3.8 shows the transient absorption spectra of **Acr1** at pH 7.4 and pH 6. After the action of the a pulsed laser at 430 nm (4-6 ns fwhm), a transient species was formed which absorbs light in the 480-650 nm region of the probe light with the maximum at 540 nm (Figure 3.8 A and B).

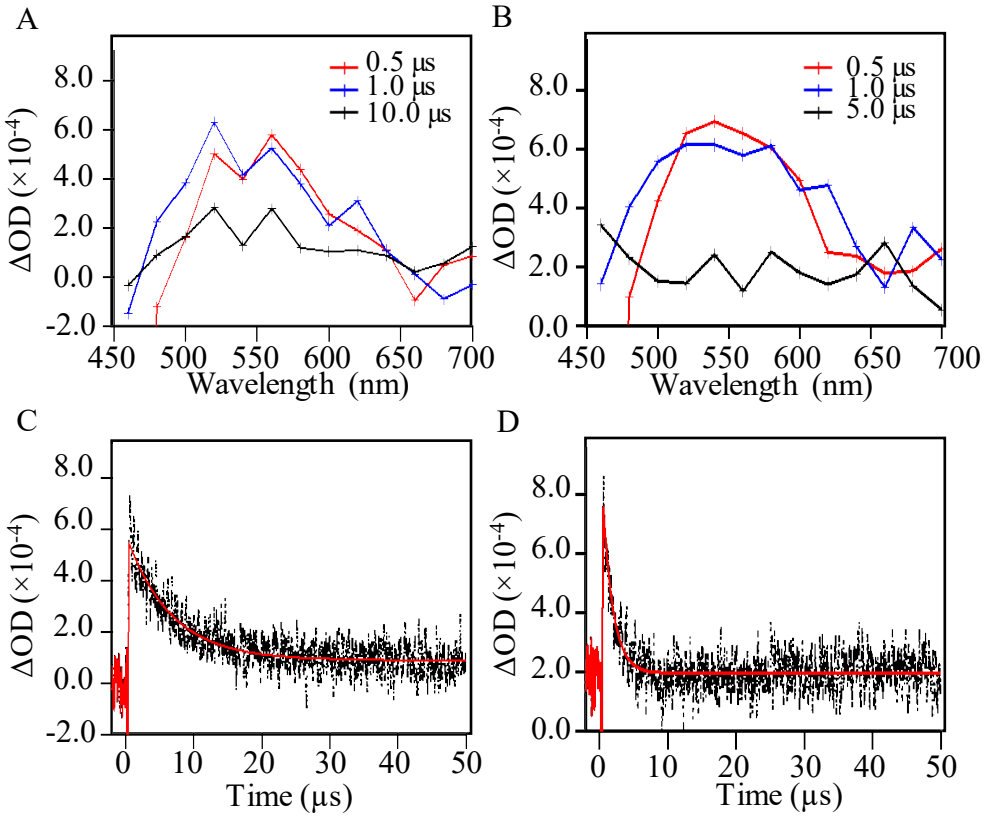

Figure 3.8. The nanosecond-transient absorption spectra of **Acr1** in aq. solutions at (A) pH 7.4 and (B) pH 6.0. Decay profiles at 540 nm at (C) pH 7.4 and (D) pH 6.0 (black dot) with the mono-exponential fitting curve (red line).

The absorption profile of the photogenerated species is well-matched with the peak obtained from the differential spectra between **Acr1** and **Acr1-betaine**. Thus, the photogenerated species was assigned to **Acr1-betaine** (Figure 3.9).

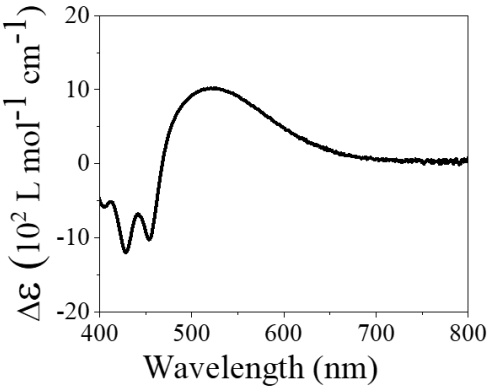

Figure 3.9. The differential absorption spectrum constructed by substracting the absorption spectrum of **Acr1-betaine** from **Acr1**.

The hypothesis of the photoinduced generation of the betaine was further verified by determining the lifetime of the species by examining the decay profile at different pH.

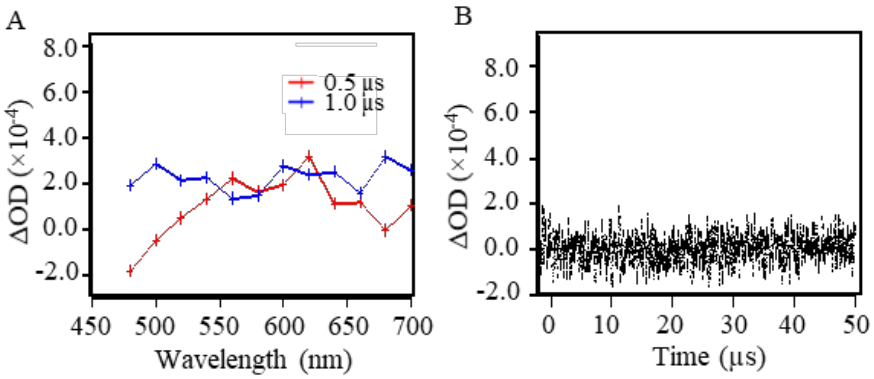

Figure 3.10. (A) The nanosecond-transient absorption spectra of **Acr1** in aq. solutions at pH 5. (B) Decay profiles at 540 nm in aq. solutions at pH 5.

Decay profiles at 540 nm arising from the betaine were analyzed and fitted mono-exponentially. The long-lived component with a half-life of 6.6 μs at pH 7.4 was diminished to 1.5 μs at pH 6 (Figures 3.8 C and 3.6 D), and at pH 5 no signal was observed (Figure 3.10) in the available timescale of the apparatus (>500 ns). Thus, the pH

dependency of the half-lives of the photogenerated species validates the assumption of photoinduced betaine generation.

The excited-state dynamics can be explained based on Scheme 3.2. Initially, the acridinium moiety was excited to the singlet excited state. Analogous 9-substituted acridinium compounds undergo electron transfer within picosecond time scale. Usually, phenolic OH groups undergoes deprotonation when the adjacent aromatic ring endures one-electron oxidation.[16] In **Acr1** the electron transfer state readily undergoes excited-state deprotonation and emerge into a betaine structure. At neutral pH the photogenerated betaine has an appreciably long lifetime. At lower pH the lifetime is reduced due to the re-protonation of the betaine. These results support the formation of **Acr1-betaine**, which can return to the protonated form (**Acr1**) by a faster protonation at lower pH and persist for long-time at neutral pH. An analogues compound of **Acr1** with an acridinium and phenolic moieties, can deprotonate under photoexcitation, to show photoacid behavior.[16] In the present study, the photogenerated betaine formed as the consequence of excited-state deprotonation, exhibited long lifetime, opening the possibility of further excitation to utilize it as an efficient photothermal generator.

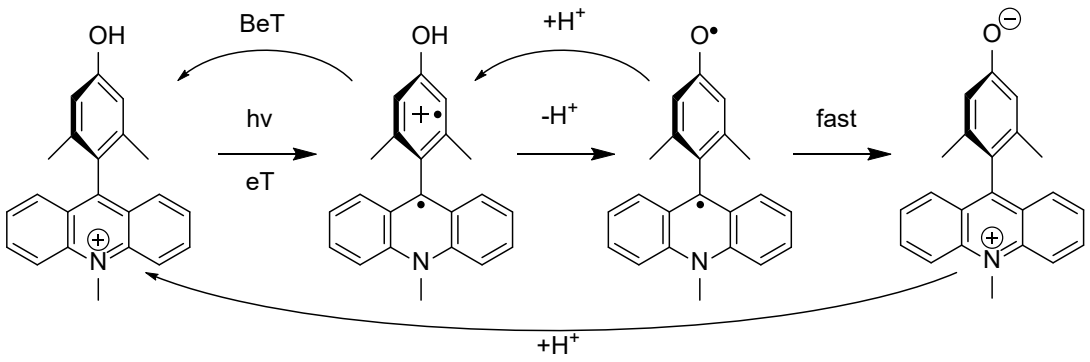

Scheme 3.2. The proposed scheme of PET and the subsequent deprotonation leading to the formation of **Acr1-betaine** from **Acr1**. eT: Electron transfer. BeT: Back electron transfer.

The excited-state properties of the model compound **Acr2** was studied in parallel. Figure 3.11 A shows the nanosecond transient absorption spectra of **Acr2** at pH 7. After

a pulsed laser excitation at 430 nm, **Acr2** showed a characteristic peak centered at 500 nm at pH 7.4 (Figure 3.11). The transient species showed long half-life (τ~35 μs), and it is matching to the one arising from the CS of **Acr2** (**Acr2-CS**), which corresponds to one-electron oxidized mesitylene moiety and one-electron reduced acridinium (τ~35 μs),[20] confirming the occurrence of PET and subsequent formation the CS in **Acr2** (Scheme 3.3). Therefore, **Acr1** and **Acr2** can form different long-lived photogenerated species, **Acr1-betaine** and **Acr2-CS** and the additional photoexcitation of these species are possible.

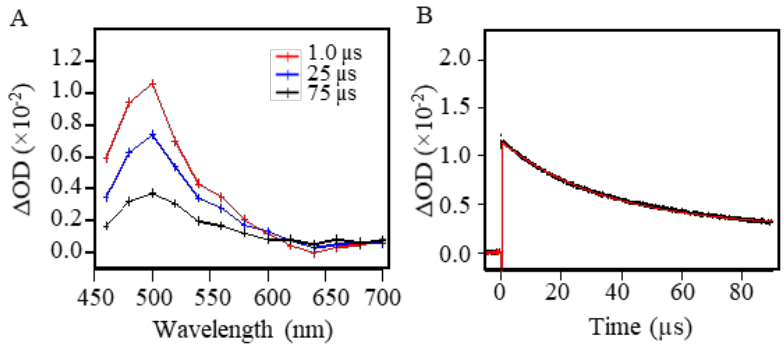

Figure 3.11. (A) The nanosecond-transient absorption spectra of **Acr2** in aq. solution at pH 7. (B) Decay profiles at 500 nm arising from **Acr2** in aqueous solutions at pH 7.

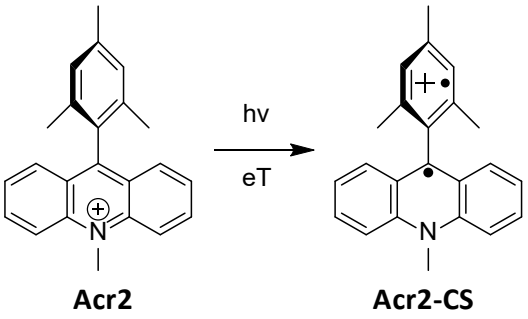

Scheme 3.3. A scheme of PET in **Acr2** and the subsequent formation of **Acr2-CS**.

3.4 pH-Dependent photothermal effect by dual photoexcitation

The long-lived photogenerated species **Acr1-betaine** and **Acr2-CS** with the expanded light absorption as discussed above, encouraged me to use them as a light-responsive heat generator. Therefore, I examined the PTEs of **Acr1** and **Acr2** under additional

photoexcitation of the long-lived **Acr1-betaine** and **Acr2-CS**. For this purpose, a dual photoexcitation method was followed which is by using two individual light sources. One is a blue light (420-440 nm LED, 140 mW cm^{-2}), to excite ground state molecules. The other is yellow light (Xenon lamp with a long pass filter, >480 nm, 440 mW cm^{-2}) for the additional excitation of the long-lived photogenerated species. Both **Acr1** and **Acr2** does not show significant absorption in the wavelength higher than 480 nm. However, **Acr1-betaine** and **Acr2-CS** absorb longer wavelength region (480-700 nm) of light.

In order to study the pH-dependent PTE in 9-position substituted acridinium based compounds, I monitored the temperature response showed by the aq. solution of the three compounds under the illumination of blue and yellow light. To know the enhancement in thermal response by the additional excitation of the photogenerated species, the dual-wavelength excitation (simultaneous illumination of both blue and yellow light) was applied, and the corresponding temperature change was monitored.

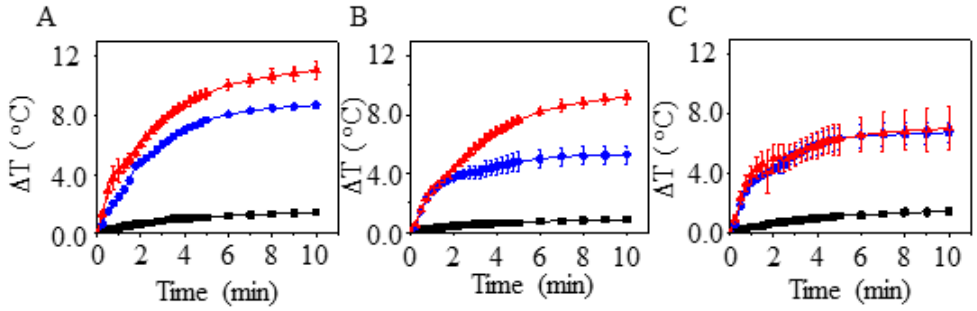

Figure 3.12. The photothermal responses showed by (A) **Acr1**, (B) **Acr2** and (C) **Acr3** at pH 7.4 due to the excitation with the blue light (420-440 nm, 140 mW cm^{-2}) (blue circle), a Xenon lamp (>480 nm, 440 mW cm^{-2}) (black quare), or the simultaneous excitation with both the light sources (red triangle).

Figures 3.12 A-C show the PTEs exhibited by **Acr1, Acr2**, and **Acr3** at pH 7.4 by the blue light (420-440 nm, 140 mW cm^{-2}), the yellow light (>480 nm, 440 mW cm^{-2}), or under dual photoexcitation. All the three compounds show increase in the temperature by the blue light illumination and under the dual photoexcitation. However, the yellow light illumination did not cause significant PTE, and showed comparable changes to that of the blank solution (Figures 3.13). Among the three compounds, **Acr1**

showed the largest increase in the temperature up to 11.0 °C at 10 min (Figure 3.12 A) under dual photoexcitation, demonstrating a high PTE from **Acr1**.

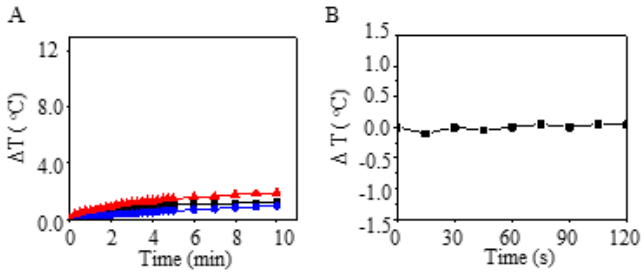

Figure 3.13. (A) Temperature response by irradiating the blank solution (phosphate buffer at pH 7.4) with the blue light (420-440 nm, 140 mW cm^{-2}) (blue circle), a Xenon lamp (>480 nm, 440 mW cm^{-2}) (black square), or simultaneous excitation with both the light sources (red triangle). (B) The effective PTE by the dual photoexcitation.

The betaine-type molecules are known to facilitate efficient nonradiative relaxation to release the excitation energy, which leads to the high efficiency of PTE.[9] To inspect the thermal response induced by the additional excitation of the photogenerated species (the enhanced PTE), the differential plots of effective thermal response as a function of the time under photoexcitation was constructed (Figure 3.14 A-C).

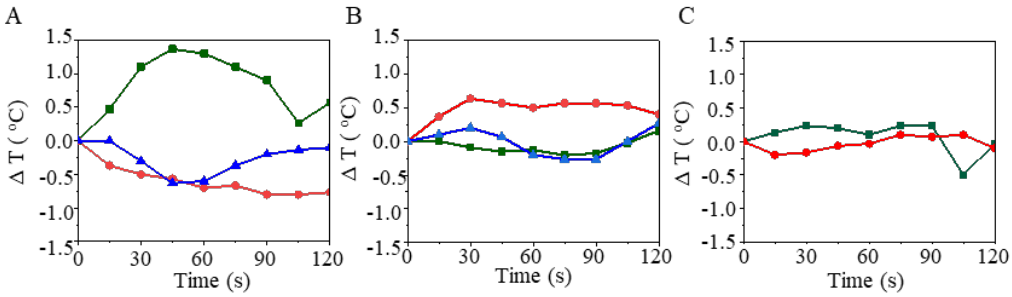

Figure 3.14. The effective PTE which is enhanced by the dual photoexcitation of (A) **Acr1** (B) **Acr2** and (C) **Acr3** at pH 7.4 (green square), pH 2 (red circle) and pH 12 (blue triangle).

The differential thermal plots are constructed by the simple subtraction of the sum of thermal responses showed under individual blue and yellow light illumination from that of temperature elevation under dual photoexcitation. The positive signals in Figures

3.14 A-C show the enhanced PTE attained under dual photoexcitation. In Figure 3.14 A, **Acr1** shows substantial thermal response under dual photoexcitation, and **Acr3** does not show any enhancement in PTE as shown in Figure 3.14 C. Therefore, additional excitation of photoexcited **Acr1** with yellow light enables enhanced PTE which helps to utilize a broad spectrum of wavelength. **Acr1** displayed a remarkable response to the dual photoexcitation at pH 7.4 due to the formation of **Acr1-betaine** with an appreciably long half-life. **Acr1** showed the notable enhancement in PTE up to 1.4 ºC within one min of the dual photoexcitation (Figure 3.14 A), i.e, 37 % enhancement in PTE was obtained.

3.5 Calculation of photothermal conversion efficiency of Acr1

The photothermal conversion is a standard parameter which represents the potential of an agent to effectively absorb the photon and convert it into the useful heat energy.[10] The photothermal conversion efficiency of **Acr1** was calculated according to the previous reports. [21,22] To this purpose a solution of **Acr1** in phosphate buffer at pH 7.4 was irradiated with a 446 nm laser for 25 min. The change in temperature was recorded as a function of time. Afterward, the laser was shut-off and the temperature drop was monitored until the room temperature was reached. A plot of temperature change *vs* time of irradiation was constructed (Figure 3.15 A). The photothermal conversion efficiency was calculated according to equation 3.

$$\eta = \frac{\mathrm{hS\,(T_{Max} - T_{Surr}) - Q_{dis}}}{\mathrm{I\,(1 - 10^{-A_{446}})}} \quad (3)$$

Where h is the heat transfer coefficient, *S* is the surface area of the container, T_{max} is the maximum temperature achieved by illumination, and T_{surr} is the temperature of the surroundings. I correspond to the intensity of the power source (446 nm laser at 0.075 W cm^{-2}), and A_{446} represents the absorbance of the sample solution at 446 nm. Q_{dis} rep resents the thermal response exhibited by the blank solution under identical condition. hS was calculated according to equation 4.

$$\mathrm{hS} = \frac{m_D C_D}{\tau_s} \quad (4)$$

Where m_D and C_D are the mass and heat capacity of deionized water, and τ_s is the sample system time constant and determined according to the equation 5. τ_s was determined as 390 s by the linear fitting of plot of the cooling period versus the negative logarithm of the driving force(θ) (Figure 3.15 B).

$$t = -\tau_s \ln \theta \tag{5}$$

$$\theta = \frac{(T - T_{Surr})}{(T_{Max} - T_{Surr})} \tag{6}$$

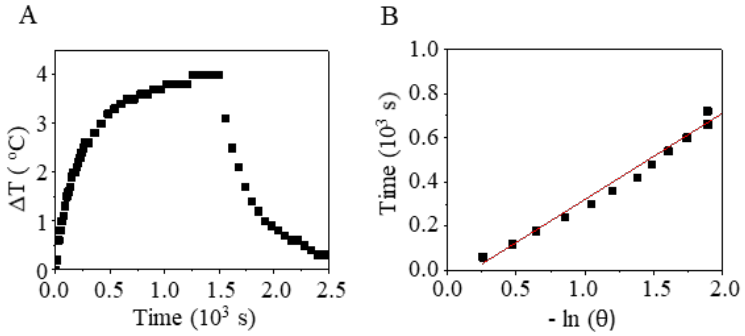

Figure 3.15. (A) The PTE showed by an aqueous solution of **Acr1** at pH 7.4 (0.72 mM in a glass cuvette with 0.2 cm thickness) by a 446 nm laser (at 0.075 W cm^{-2}), the irradiation was continued for 1500 s, and then the laser was turned off, and cooling pattern was monitored. (B) The plot of the cooling period versus the negative logarithm of the driving force(θ). The linear fitting affords τ_s = 390 s.

Acr1 showed a photothermal conversion efficiency of 43% under the blue light illumination (446 nm diode laser, 75 mW). This value is sufficiently high as a model organic molecule for photothermal conversion.[22] It is noteworthy that the high energy conversion efficiency under the blue light excitation is further enhanced by the yellow light illumination due to the betaine generation. Thus, the cumulative photothermal efficiency of **Acr1** will be enhanced under dual photoexcitation and the value will be higher than 43 %.

3.6 The effect of the excitation power of the blue light on the photothermal effect of Acr1.

The enhanced PTE by dual-wavelength excitation **Acr1** was studied as a function of the power of the blue light. For this purpose, the temperature response under simultaneous excitation with yellow and blue light was monitored as a function of the power of the blue LED. The powers of the LED were 140 mW cm^{-2}, 100 mW cm^{-2}, and 53 mW cm^{-2}. Figure 3.16 shows the power-dependent photothermal response of **Acr1**.

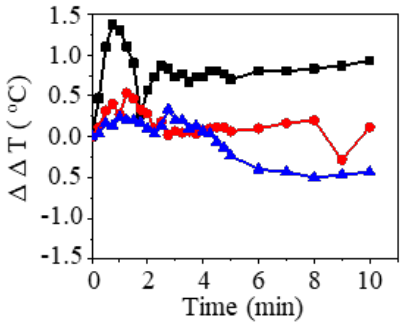

Figure 3.16. The power-dependent photothermal response of **Acr1** at pH 7.4 by the dual photoexcitation. The powers of the LED were 140 mW cm^{-2} (black), 100 mW cm^{-2} (red), and 53 mW cm^{-2} (blue).

From the power-dependent studies, it was verified that the PTE is dependent on the intensity of the blue light source which triggers the generation of the betaine. Generally, in photothermal studies and real-time applications, lasers with the excitation power of several milliwatts to watts have been used. In the present study the maximum power used was 140 mW cm^{-2} which is very low compared to the previous reports.[7] Therefore, by increasing the power of the excitation light, the PTE can be enhanced.

3.7 The pH-dependent photostability studies

Excellent photostability is a vital feature that any photothermal agents are demanded to hold in order to elicit recyclability and long-term durability. Therefore, the photostability of all the three molecules was checked at acidic, neutral and basic pH. Figure 3.17 shows the absorption spectra of **Acr1** recorded as the function of time under dual-wavelength excitation at various pH. The absorption spectra of **Acr1** remained intact during dual-wavelength photoexcitation. Interestingly, **Acr1** showed excellent photostability irrespective of the pH of the medium. Along with structural reversibility by changing the pH, stability against photoirradiation was maintained for several hours. The appealing photostability of the **Acr1** makes it an efficient photothermal generator in all environmental conditions.

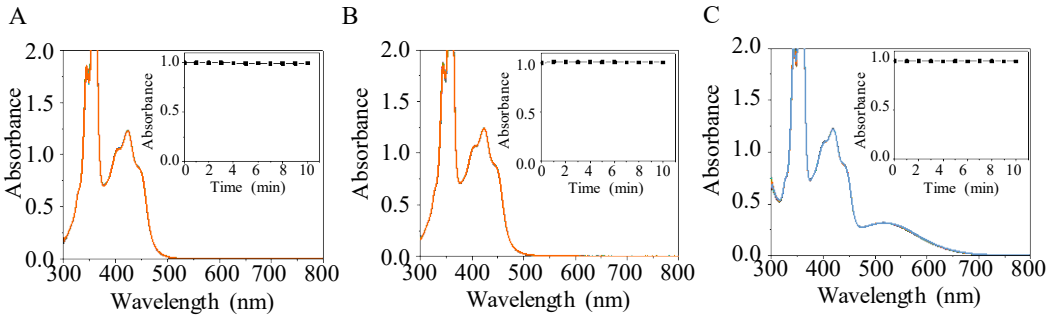

Figure 3.17. Absorption spectra of **Acr1** recorded as the function of time under the dual photoexcitation of blue (420-440 nm, 140 mW cm^{-2}) and yellow light (>480 nm, 440 mW cm^{-2}) at (A) pH 2 (B) pH 7.4 and (C) pH 12. The insets provide the change in the absorbance at 430 nm plotted as the function of time under photoirradiation.

In contrast to **Acr1**, the analogous compound **Acr2** showed poor photostability at neutral and basic pH, after illuminating with the blue light, **Acr2** showed remarkable photodegradation and the photodegraded product was settled as a dark brown precipitate in the cuvette. Figure 3.18 shows the absorption spectra of **Acr2** recorded as the function of time under dual-wavelength excitation at various pH.

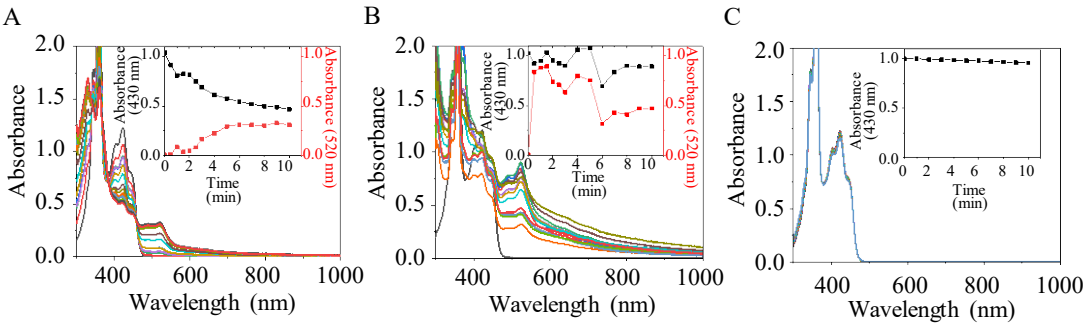

Figure 3.18. The absorption spectra of **Acr2** recorded as the function of time under the dual photoexcitation of blue (420-440 nm, 140 mW cm^{-2}) and yellow light (> 480 nm, 440 mW cm^{-2}) at (A) pH 7.4 (B) pH 12 and (C) pH 2. The insets provide the change in the absorbance at 430 nm (black squares) and at 520 nm (red squares) plotted as the function of time under photoirradiation.

In **Acr2**, the decrease in the characteristic band around 430 nm of suggest the decomposition of the acridinium moiety. Increase in pH of the medium accelerated degradation (Figure 3.18 A and 3.18 B). This degradation can be attributed to nucleophilic attack of OH^- to the photoexcited acridinium.[23,18] At low pH such as pH 2, photodegradation is reduced because of the low concertation of OH^- in the medium supressing the hydroxylation process. As the result the compound found photostable at lower pH (Figure 3.18C). Therefore, it was verified that the acidic pH is essentially required for utilization of **Acr2** and its derivatives.

The second model compound, the simple acridinium ion, **Acr3** showed no photodegradation at neutral or acidic pH. Photoexcited acridinium ion undergoes radiative decay with fluorescence quantum yield unity.[24] Since there are no complicated excited state processes involved, **Acr3** showed good photostability. Although it was verified in the earlier section of this chapter that **Acr3** intrinsically degrades at basic pH due to nucleophilic attack of OH^- ions. Therefore, PTE and photostability studies of **Acr3** at pH 12 was deliberately omitted.

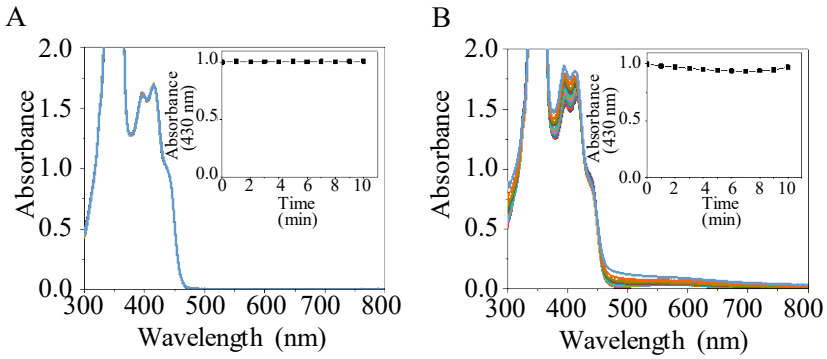

Figure 3.19. Absorption spectra of **Acr3** recorded as the function of time under the dual photoexcitation of blue (420-440 nm, 140 mW cm^{-2}) and yellow light (> 480 nm, 440 mW cm^{-2}) at (A) pH 2 (B) pH 7.4. The insets provide the change in the absorbance at 430 nm plotted as the function of time under photoirradiation.

3.8 The mechanism of pH-dependent photothermal effect and dual photoexcitation induced enhanced thermal response

The PTE generation by **Acr1** can be rationalised in terms of PET mediated betaine generation and the enhanced photothermal response induced by dual-wavelength which is claimed due to the longer wavelength absorption of the photogenerated long-living betaine. The enhanced PTE in **Acr1** can be explained by the proposed mechanistic pathway, as depicted in Scheme 3.4. At pH 7.4, **Acr1** is in the protonated form in the ground state. By 430 nm illumination, a fast intramolecular electron transfer occurs in **Acr1** which leads to deprotonation and fast intramolecular electron transfer to form **Acr1-betaine. Acr1-betaine** show lifetime about 6.6 μs at pH 7.4 (Figure 3.8). Since **Acr1-betaine** has an optical absorption in the 480 nm-700 nm wavelength region, the further excitation of the photogenerated **Acr1-betaine** with a yellow light is possible, and it can lead to the enhanced PTE. The reason behind moderate PTE under dual photoexcitaion is **Acr1-betaine** itself has strong absorption in the blue light region (around 430 nm). Therefore, **Acr1-betaine** can generate heat with only blue light illumination, limiting the enhanced PTE. The enhanced PTE was not observed in **Acr1** at acidic pH (pH 2), at which the lifetime of the photogenerated **Acr1-betaine** is very short (Figure 3.8 D and

3.10 B). At alkaline pH (pH 12), **Acr1-betaine** is already formed without the blue light illumination, and thus the enhanced PTE was not observed (Figure 3.14 A).

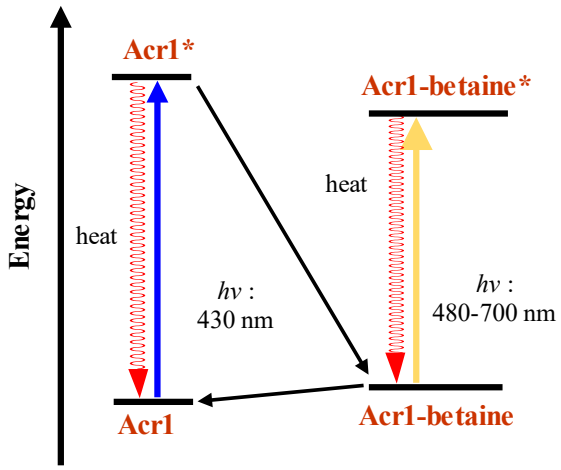

Scheme 3.4. A diagram describing the photoinduced generation of long-living betaine and the subsequent irradiation leading to enhanced PTE.

Meanwhile, the model compound **Acr2** showed an attenuated thermal response for the first 2 minutes of dual-wavelength irradiation. This attenuation in thermal response can be justified by the fast photodegradation of the compound. Nonetheless, the increased photothermal effect evolved afterward is due to the absorption band (with λ_{max} :520 nm) in longer wavelength region absorption of the photodegraded product. Since the photodegradation is irreversible in nature, **Acr2** cannot be nominated as an agent for photothermal energy conversion. On the other hand, the excellent photostability and efficient photothermal energy conversion by **Acr1** makes it an eminent candidate for real-time applications.

3.9 Conclusions

The generation of photothermal effect by 9-position substituted acridinium electron D-A dyads is comprehensively studied using a novel D-A dyad, **Acr1** and two analogous model compounds. The **Acr1** showed a fast PET followed by pH-dependent formation of the photogenerated betaine **Acr1-betaine** which absorbs the light in the 480-700 nm, which was verified by ns-transient absorption studies. Meanwhile, the model compound, **Acr2** showed photodegradation at neutral and basic pH, limiting its recyclability for photothermal energy conversion. **Acr1** showed excellent photostability than **Acr2** with the enhanced PTE for elevating the solution temperature. The photothermal conversion efficiency of **Acr1** was found to be 43 % with blue laser illumination, and the dual photoirradiation lifts the PTE. The present study provides useful information to design and synthesize the variety of molecules to achieve upgraded light-harvesting properties from the additional excitation of the photogenerated species. This work introduces a promising strategy to exploit the absorption properties of photogenerated species to accomplish efficient harvesting and photothermal conversion of light.

References

1. Sell, J. Photothermal *investigations of solids and fluids. Elsevier,* **2012**.
2. Jiang, Q.; Zeng, W.; Zhang, C.; Meng, Z.; Wu, J.; Zhu, Q.; Wu, D.; Zhu, H. Broadband Absorption and Enhanced Photothermal Conversion Property of Octopod-like Ag@Ag2S Core@shell Structures with Gradually Varying Shell Thickness. *Sci. Rep.* **2017**, *7* (1), 1–11.
3. Jaque, D.; Martínez Maestro, L.; Del Rosal, B.; Haro-Gonzalez, P.; Benayas, A.; Plaza, J. L.; Martín Rodríguez, E.; García Solé, J. Nanoparticles for Photothermal Therapies. *Nanoscale* **2014**, *6* (16), 9494–9530.
4. Shibu, E. S.; Hamada, M.; Murase, N.; Biju, V. Nanomaterials Formulations for Photothermal and Photodynamic Therapy of Cancer. *J. Photochem. Photobiol. C Photochem. Rev.* **2013**, *15* (1), 53–72.
5. Estelrich, J.; Antònia Busquets, M. Iron Oxide Nanoparticles in Photothermal Therapy. *Molecules* **2018**, *23* (7),1567.
6. Yu, J.; Yang, L.; Yan, J.; Wang, W.C.; Chen, Y.C.; Chen, H.H.; Lin, C.H. Carbon Nanomaterials for Photothermal Therapies. *Carbon Nanomaterials for Bioimaging, Bioanalysis, and Therapy,* **2019**.
7. Jung, H. S.; Verwilst, P.; Sharma, A.; Shin, J.; Sessler, J. L.; Kim, J. S. Organic Molecule-Based Photothermal Agents: An Expanding Photothermal Therapy Universe. *Chem. Soc. Rev.* **2018**, *47* (7), 2280–2297.
8. Liao, J. F.; Li, W. T.; Peng, J. R.; Yang, Q.; Li, H.; Wei, Y. Q.; Zhang, X. N.; Qian, Z. Y. Combined Cancer Photothermal-Chemotherapy Based on Doxorubicin/Gold Nanorod-Loaded Polymersomes. *Theranostics* **2015**, *5* (4), 345–356.
9. Li, C.; Lin, W.; Liu, S.; Zhang, W.; Xie, Z. Self-Destructive PEG–BODIPY Nanomaterials for Photodynamic and Photothermal Therapy. *J. Mater. Chem. B* **2019**, *7* (30), 4655–4660.
10. Shin, D.; Kang, G.; Gupta, P.; Behera, S.; Lee, H.; Urbas, A. M.; Park, W.; Kim, K. Thermoplasmonic and Photothermal Metamaterials for Solar Energy Applications. *Adv. Opt. Mater.* **2018**, 6 (18),1800317.

11. Gao, M.; Zhu, L.; Peh, C. K.; Ho, G. W. Solar Absorber Material and System Designs for Photothermal Water Vaporization towards Clean Water and Energy Production. *Energy Environ. Sci.* **2019**, *12* (3), 841–864.
12. Wang, Y.; Tang, B.; Zhang, S. Novel Organic Solar Thermal Energy Storage Materials: Efficient Visible Light-Driven Reversible Solid-Liquid Phase Transition. *J. Mater. Chem.* **2012**, *22* (35), 18145–18150.
13. Upama, M. B.; Wright, M.; Mahmud, M. A.; Elumalai, N. K.; Mahboubi Soufiani, A.; Wang, D.; Xu, C.; Uddin, A. Photo-Degradation of High Efficiency Fullerene-Free Polymer Solar Cells. *Nanoscale* **2017**, *9* (47), 18788–18797.
13. Fukuzumi, S.; Ohkubo, K.; Suenobu, T. Long-Lived Charge Separation and Applications in Artificial Photosynthesis. *Acc. Chem. Res.* **2014**, *47* (5), 1455–1464.
14. Fukuzumi, S.; Kotani, H.; Ohkubo, K.; Ogo, S.; Tkachenko, N. V.; Lemmetyinen, H. Electron-Transfer State of 9-Mesityl-10-Methylacridinium Ion with a Much Longer Lifetime and Higher Energy Than That of the Natural Photosynthetic Reaction Center. *J. Am. Chem. Soc.* **2004**, *126* (6), 1600–1601.
15. Zhao, G.; Wang, T. Stereoselective Synthesis of 2-Deoxyglycosides from Glycals via Visible-Light-Induced Photoacid Catalysis. *Angew. Chemie Int. Ed.* **2018**, 6120–6124.
16. Adamczyk, M.; Chen, Y. Y.; Mattingly, P. G.; Moore, J. A.; Shreder, K. Modulation of the Chemiluminescent Signal from N10(3-Sulfopropyl)-N-Sulfonylacridinium-9-Carboxamides. *Tetrahedron* **1999**, *55* (36), 10899–10914.
17. Romero, N. A.; Nicewicz, D. A. Organic Photoredox Catalysis. *Chem. Rev.* **2016**, *116* (17), 10075–10166.
18. Xu, W.; Chen, H.; Wang, Y.; Zhao, C.; Li, X.; Wang, S.; Weng, Y. Photoinduced Electron and Energy Transfer in Dyads of Porphyrin Dimer and Perylene Tetracarboxylic Diimide. *ChemPhysChem* **2008**, *9* (10), 1409–1415.
19. Takano, Y.; Hanai, E.; Imahori, H. Photoinduced Electron Transfer Reaction in Mitochondria for Spatiotemporal Selective Photo-Oxidation of Lipids by Donor/Acceptor Linked Molecules. *Nanoscale* **2017**, *9* (45), 17909–17913.
20. Lan, M.; Guo, L.; Zhao, S.; Zhang, Z.; Jia, Q.; Yan, L.; Xia, J.; Zhang, H.; Wang, P.; Zhang, W. Carbon Dots as Multifunctional Phototheranostic Agents for

Photoacoustic/Fluorescence Imaging and Photothermal/Photodynamic Synergistic Cancer Therapy. *Adv. Ther.* **2018**, *1* (6), 1800077.

21. Liu, X.; Li, B.; Fu, F.; Xu, K.; Zou, R.; Wang, Q.; Zhang, B.; Chen, Z.; Hu, J. Facile Synthesis of Biocompatible Cysteine-Coated CuS Nanoparticles with High Photothermal Conversion Efficiency for Cancer Therapy. *Dalt. Trans.* **2014**, *43* (30), 11709–11715.
22. Nakazono, M.; Oshikawa, Y.; Nakamura, M.; Kubota, H.; Nanbu, S. Strongly Chemiluminescent Acridinium Esters under Neutral Conditions: Synthesis, Properties, Determination, and Theoretical Study. *J. Org. Chem.* **2017**, *82* (5), 2450–2461
23. Joseph, J.; Kuruvilla, E.; Achuthan, A. T.; Ramaiah, D.; Schuster, G. B. Tuning of Intercalation and Electron-Transfer Processes between DNA and Acridinium Derivatives through Steric Effects. *Bioconjug. Chem.* **2004**, *15* (6), 1230–1235.

Chapter 4

Intramolecular Electron Transfer for Singlet Oxygen Sensing

Abstract: Singlet oxygen ($^1O_2$) gathers significant attention in chemistry and biology. There are several spectroscopic methods employ to detect $^1O_2$. Among these techniques, fluorescence sensing is one of the most promising method. Therefore, several anthracene-based electron D-A dyads are reported. Although, the correlation between the structure of the sensor and the sensing efficiency needs further attention. In this work, the $^1O_2$ sensing efficiency of various fluorescence sensor based on substituted anthracenes is examined and compared the efficiency with that of 9-methylanthracene. The rate of reaction of $^1O_2$ to the sensors and 9-methylanthracene is estimated using steady-state absorption spectroscopy. The second-order reaction rate of the $^1O_2$ and the sensors is an order of magnitude less than that of 9-methylanthracene. The lower reactivity of the sensors to $^1O_2$ is studied in terms of substituent effect, such as electronic interactions, steric interactions, and the reactivity of the intermediate complex.

4.1 Introduction

4.1.1 Reactive oxygen species

Oxygen, an inevitable part of the subsistence of life on the planet earth, exerts different effects in one form or another in the process of homeostasis. Starting from the metabolic process, the energy-producing oxidative phosphorylation in the ground state triplet form, it is employed in several constructive as well as destructive activities as in the form of reactive oxygen species (ROS) in life-cycle. Molecular oxygen in the ground-state is in a biradical form by the presence of two unpaired electrons occupying two separate orbitals in the outer shell, restricting the reactivity of the triplet state oxygen. However, the ground-state oxygen is converted into ROS during the aerobic metabolism in mitochondria. ROS poses extremely high reactivity towards biomolecules, including proteins, amino acids, and deoxyribonucleic acid (DNA). Either molecular oxygen can receive excitation energy to produce $^1O_2$ or can undergo electron transfer reactions to

produce superoxide ($O_2^{-\bullet}$), which is a precursor to many ROS. The dismutation of superoxide leads to the production of hydrogen peroxide (H_2O_2) which can undergo partial reduction to produce the strongest oxidant hydroxyl radical (OH•).[1]

ROS has significant importance in cell signaling. The redox signaling mediated by ROS constitutes the maintenance of diverse cellular activities such as cellular differentiation, tissue regeneration, prevention of aging, and control over various diseases. In the case of a properly functioning cell, the level of ROS is maintained by several antioxidative mechanisms. However, the balance in the ROS level in the physiological environment can be destroyed, causing accelerated production of ROS, which in turn leads to oxidative stress. The oxidative stress can impact several diseases such as neurological diseases, diabetes, cardiovascular diseases, and cancer. The oxidative stress can be originated as the result of exposure to xenobiotics, undesirable radiations, and unhealthy habits.[2,3] Nevertheless, the controlled rise of ROS can employ to cure life-threatening diseases. For example,$^1O_2$ can act as an anticancer agent in photodynamic therapy.

4.1.2 Singlet oxygen ($^1O_2$)

$^1O_2$, the lowest excited state of molecular oxygen, attracted significant attention in chemistry, biology, and environmental cleaning. $^1O_2$ is highly reactive due to its electrophilic nature. Therefore, $^1O_2$ is used as a versatile organic reagent. $^1O_2$ prompt positive as well as negative impacts on the biological systems. $^1O_2$ mediated signaling in plant, and animal cells lead to either constructive or destructive actions. $^1O_2$ acts as an active anti-microbial agent for disease prevention. Most importantly, cancer eradication strategy employed by $^1O_2$ made photodynamic therapy as an eminent anticancer treatment. However, the oxidative damage of biomolecules by $^1O_2$ is an ongoing matter of concern.

The occurrence of the singlet form of oxygen was predicted by R. Mulliken in 1928. He used molecular orbital theory to study the triplet and singlet electronic configurations of oxygen. The observation of the Fraunhofer line at 762 nm was key information to the existence of $^1O_2$. In 1931, Kautsky proposed the photosensitized generation of $^1O_2$ and demonstrated the photooxidation of a substrate. In 1963, Kasha and Khan interpreted the chemiluminescence from an aqueous solution of H_2O_2 and

hypochlorite, which was previously reported by Seliger, and the luminescence was assigned to a metastable singlet state of oxygen. In 1964, Foote and Wexer proved the involvement of $^1O_2$ in the photodynamic action of triplet state photosensitizer in the solution phase.Molecular oxygen ($^3\sum_g^-$) has two low lying singlet excited states. Singlet delta ($^1\Delta_g$: 22.5 kcal mol^{-1}) and other form, singlet sigma ($^1\sum_g^+$:31.5 kcal mol^{-1}). Compared to the ground-state molecular oxygen in the triplet state, both the excited state species exhibit diamagnetic spin due to the net cancellation of orbital angular moment associated with the electron in the π* orbitals. The molecular orbital diagram of the ground-state and excited-state of oxygen is shown in Figure 4.1.[4]

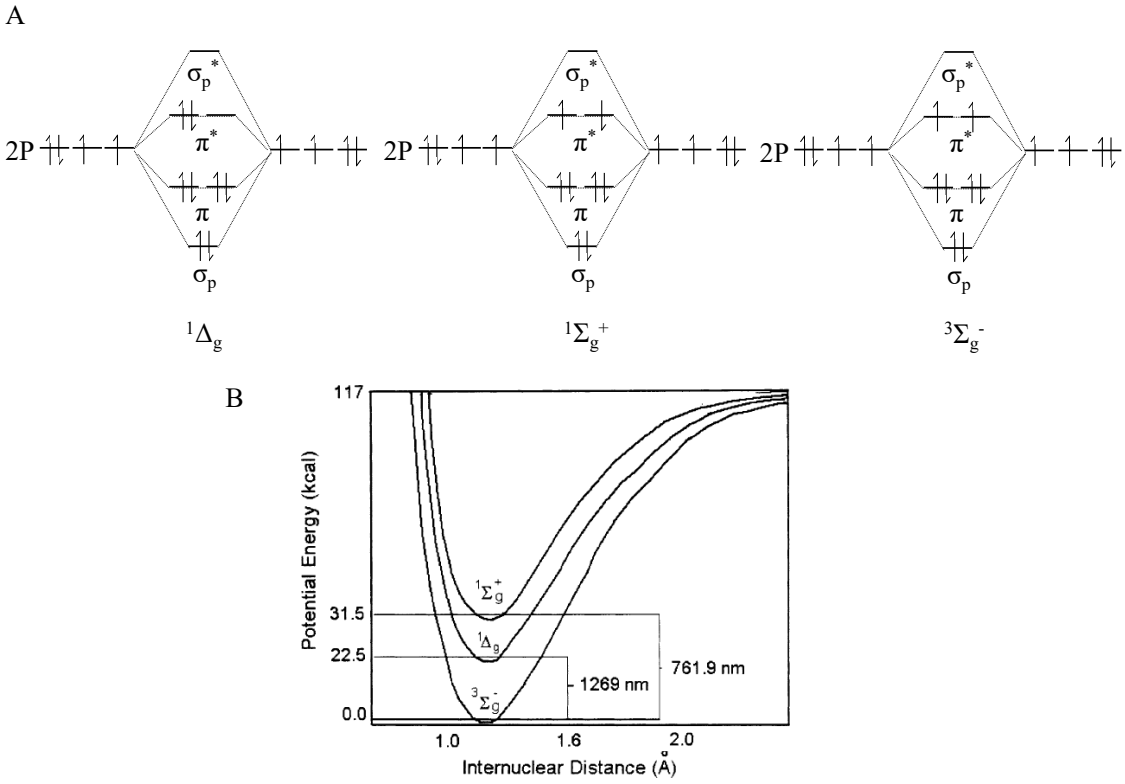

Figure 4.1. (A) The molecular orbital diagram of oxygen in the excited ($^1\Delta_g$ and $^1\sum_g^+$) and ground ($^3\sum_g^-$) states. (B) Potential energy curves for the three electronic states of molecular oxygen (reprinted from Ref 4).

4.1.3 Singlet oxygen sensitization

There are several physical well as chemical methods have been reported for the generation of $^1O_2$ in the solution phase.[4-13] Evans's and Matheson's groups reported the generation of $^1O_2$ by the direct high-power laser excitation of oxygen molecules at very high pressure. Later, $^1O_2$ was generated by the direct 765 nm and 1270 nm laser excitations of air-saturated water and organic solvents. The production of $^1O_2$ by the direct excitation method was verified by observing phosphorescence as two narrow bands with maxima at 1273 and 765 nm and using a chemical trap, 1,3-diphenylisobenzofuran (DPIBF) in air-saturated solvents. However, the optical density and extinction coefficient of oxygen at 1273 nm and 765 nm are very low, limiting the applicability of the direct excitation method for $^1O_2$ generation.[4,5,8]

Photosensitization is a simple and versatile method applied to generate $^1O_2$. In this method, only a photosensitizer (PS), oxygen, and light are needed. Since light acts as a stimulus for the process, this method has substantial controllability. Photoexcitation of a PS promotes the electron to singlet excited state. The intersystem crossing leads to a population of the triplet state. Compared to the lifetime of singlet state in several ns, the triplet lifetime of PS is appreciably long (μs). The triplet state PS can interact with molecular oxygen in two distinct ways, type I and type II mechanism (Figure 4.2). In the case of the type I mechanism, the triplet PS interacts with the substrate in the vicinity by hydrogen abstraction or electron transfer to produce free radicals. The nascent free radicals created interacts with molecular oxygen to form reactive oxygen species such as superoxide. Type II mechanism relies on the energy transfer process. The collision between triplet excited state of PS and molecular oxygen leads to triplet-triplet energy transfer to generate $^1O_2$. According to Dexter, an exchange energy transfer is involved in the type II mechanism. In this method, $^1O_2$ is generated only if the sensitizer singlet-triplet energy gap of the sensitizer exceeds the excitation energy required to produce $^1O_2$ (Figure 4.2).[4,5,7] Generally, an efficient photosensitizer exhibits very high intersystem crossing (ISC) quantum yield. The triplet state PS forms noncharged transfer encounter complexes (nCT) and partial charge transfer (pCT) exciplexes in excited state with singlet, triplet or quintet multiplicity. The decay of these intermediate states by internal conversion leads to the formation of $^1O_2$ in sigma (O_2 ($^1\Sigma_g^+$)) or, delta (O_2 ($^1\Delta_g$)) form or, molecular oxygen

O_2 ($^3\Sigma_g^-$) along with PS in the ground state. The mechanism varies on the electronic configuration of the triplet state of the PS (ππ* or nπ*). The individual contribution towards net $^1O_2$ produced by the intermediate state is governed by the oxidation potential and the triplet energy of the PS. On this basis, the $^1O_2$ quantum yield of the photosensitizers used for the present study were obtained from previous reports. The $^1O_2$ quantum yield (Φ_Δ) of Rose Bengal (RB) is 0.46 in DMF [10] and Tetrakis (4-carboxyphenyl) porphyrin (TCPP) is 0.55 in DMF[11]

The quantum yield of $^1O_2$ production (Φ_Δ) by a PS is given by

$$\Phi_\Delta = \Phi_T \phi_{en} = \Phi_T \left(\frac{k_{en}[O_2]}{k_r + k_{nr} + k_q[O_2]}\right)$$

Where, Φ_T, is the quantum yield of triplet formation; ϕ_{en}, is efficiency of energy transfer; k_{en}, rate constant of energy transfer; k_r, rate of radiative relaxation (fluorescence); k_{nr}, rate of nonradiative relaxation; k_q, sum of rate constants from the quenching of PS triplet by O_2.[4]

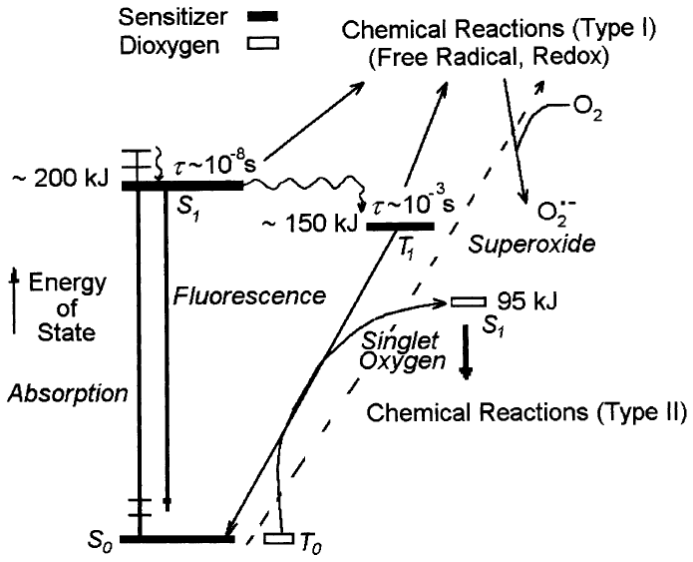

Figure 4.2. A diagram showing photosensitized generation of ROS (reprinted from Ref 4).

4.1.4 The significance of singlet oxygen

The light-induced disease curing has started before three thousand years. The ancient society used light as a curing agent for psoriasis, vitiligo, and even skin cancer. However, it took centuries to understand the mechanistic aspect of photodynamic action. The pioneering work on phototherapy was initiated by N. Finsen, who used phototherapy to cure diseases such as cutaneous tuberculosis and received Nobel prize in medicine and physiology in 1903. In the same year, H. V. Tappeiner and A. Jesionek described the curing effect of light as photodynamic action by demonstrating eosin mediated skin tumor treatment. The first clinical trial was reported in 1976 by Kelly and coworkers using a haematoporphyrin (HP) derivative Photofrin (HPD) to treat human bladder cancer. Later, the PSs have been modified from the basic porphyrin molecular framework to PS with advanced cancer-targeting properties. The first-generation PSs comprises porphyrins such as HP, HPD, and Protoporphyrin IX (PpIX). The second generation of PSs developed into a broad spectrum of organic molecules such as phthalocyanines chlorines, benzoporphyrin derivatives and, inorganic materials such as TiO_2, CdSe quantum dots, and Fullerenes. The third-generation includes PSs with cancer-targeting moieties. Captivating features such as minimal invasiveness, tumor targeting, low cost, spatiotemporal control (using light administration to protect the normal cell from damage) makes PDT an effective anticancer therapy compared to complex surgery and chemotherapy.[15-19]

PDT is initiated with intravenous or local injection of the PS and the photodynamic action is triggered by the photo illumination of PS. The ROS produced by the triplet PS by Type I and Type II mechanism can readily react with the biomolecules in the vicinity. The superoxide generated and can further produce ROS, such as H_2O_2 (by superoxide dismutase action) and hydroxyl radical, can oxidative damage to the cell by reacting with fatty acids and lipids. The $^1O_2$ produced by the Type II mechanism is vigorously reactive. It can readily react with biomolecules, including proteins, amino acids, unsaturated lipids, and nucleic acids. For example, $^1O_2$ can undergo [2+4] cycloaddition with guanosine or histidine to give endoperoxide. Also, $^1O_2$ undergoes of [2+2] cycloaddition with the amino acid, such as tryptophan to form a dioxetane. Cysteine and methionine are oxidized to sulfoxide. Unsaturated lipids suffer ene type of reaction

to give lipid hydroperoxides. $^1O_2$ leads to the oxidative damage of DNA by damaging the nucleic acid bases and the sugar linkages. All these oxidative damages ultimately lead to cell death. However, the mode and extent of cell death are governed by the intracellular localization of PS since the low lifetime of the $^1O_2$ limits its diffusion length in the cellular domain.[20,21]

4.1.5 Singlet oxygen sensing

By considering the significance of $^1O_2$ in the synthetic chemistry, cell biology, and clinical applications, detection of $^1O_2$ is important. There are several spectroscopic methods have been developed to detect $^1O_2$.

4.1.5.1 Phosphorescence detection

Analysis of the phosphorescence is a direct spectroscopic tool to detect $^1O_2$. The energy of two forms of $^1O_2$, $^1\Delta_g$ and $\sum_g^+$ are different, making a remarkable difference in the phosphorescence features. The radiative relaxation of $^1\Delta_g$ to ground-state leads to luminescence at ~1270 nm and the phosphorescence from $\sum_g^+$ can be recorded at 762 nm. Despite phosphorescence is the direct evidence for the $^1O_2$ existence, the low quantum yield of spin-forbidden phosphorescence (~10^{-2}) limits the practical application of this method. However, advancement in the phosphorescence detectors raised the applicability of this method even in biological systems.[5, 22, 23]

4.1.5.2 Electron paramagnetic detection

EPR spectroscopy has been used as an indirect method for $^1O_2$ detection. In this method $^1O_2$ is trapped using a sterically hindered amine such as 2,2,6,6-tetramethylpiperidine (TEMP). The reaction of TEMP and $^1O_2$ leads to generation of a paramagnetic N-oxyl radical (TEMPO), which gives prominent EPR signal (Scheme 4.1). However, electron transfer mediated oxidation of TEMP leads to the overestimation of the actual result which limits the reliability of this method.[24,25]

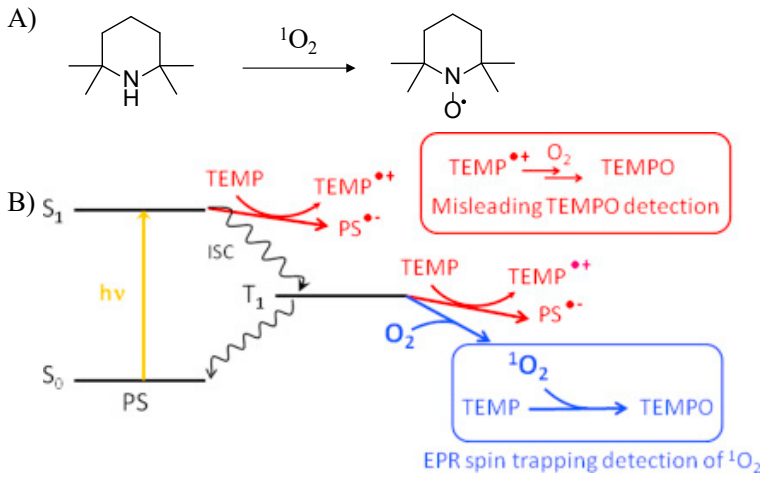

Scheme 4.1. (A) A scheme for generation of TEMPO by $^1O_2$ mediated oxidation of TEMP. (B) Scheme of TEMPO formation by electron transfer mechanism and reaction with $^1O_2$. (reprinted from Ref 25).

4.1.5.3 Fluorescence detection

Fluorescence spectroscopy is an eminent and well-sophisticated technique applied in analytical studies to investigate sensitive and ultra-low concentrated analytes. The striking feature such as high-sensitivity, cost-effectiveness, and fast responses encouraged scientists to design a fluorescence probe to detect $^1O_2$. Anthracene-based electron D-A systems are promising for efficient $^1O_2$ sensing. The fundamental structure of such an electron D-A based sensor is composed of an oxygen trapping moiety, which is anthracene, and a fluorescence reporter moiety. The sensing probe is in a fluorescence "off" state in the absence of $^1O_2$, which is by a dominant photoinduced intramolecular electron transfer from anthracene to the fluorescence reporter. The mechanism of sensing involves [4+2] cycloaddition reaction of $^1O_2$ to anthracene, leading to the formation of a 9,10-endoperoxide. Due to the endoperoxide formation, the PET is blocked, uncaging the fluorescence and leading to the detection of $^1O_2$. The most promising fluorescence sensors of $^1O_2$ are anthracene-based electron D-A dyads.[26]

In 1999, N. Umezawa et al. developed the first anthracene-based electron D-A system for fluorescence detection of $^1O_2$, which a fluorescein-anthracene conjugate and

further modified the fluorescein derivative to enhance the sensitivity of detection. Kim et al. developed a silicon-containing rhodamine-anthracene conjugate (Si-DMA), an efficient red fluorescent probe. The biocompatibility and cell-permeability of Si-DMA made it an excellent probe for invitro $^1O_2$ sensing during photodynamic therapy. However, the long and tedious synthetic procedure is a concern. Si-DMA show18-fold fluorescence enhancement upon irradiation of the photosensitizer meso-tetra (N-methyl-4-pyridyl) porphinetetratosylate for 50 min (510–550 nm at 0.07 Wcm^{-2}). Another $^1O_2$ sensor, Arhus Sensor Green (ASG) require 60 min to show the saturated fluorescence signal in the under photosensitization of phenalene-1-one-2-sulfonic acid with 420 nm (3 mW) light. The commercially available $^1O_2$ sensor, the Singlet Oxygen Sensor Green (SOSG), needs 10 min of photosensitization of tetrakis(4-carboxyphenyl) porphyrin (532 nm at 2.8 Wcm^{-2}) to detect $^1O_2$. However, SOSG is unstable under visible light due to self-sensitized $^1O_2$ generation and oxidation of the sensor.[26-31] A stable $^1O_2$ sensor based on a coumarin–anthracene conjugate (**S1**) is reported by our research group.[32]

Even though several anthracene-based fluorescence sensors are reported with good selectivity and stability, the correlation of $^1O_2$ detection rate with the structure of sensors remains undisclosed. In other words, investigation and optimization of the role of substituents on the rate of $^1O_2$ sensing need further attention for developing novel sensors with high sensitivity and faster fluorescence response. Therefore, in this work, I study the rate of $^1O_2$ sensing by different 9-substituted anthracene-based D-A dyads to understand the role of the substituent on the $^1O_2$ sensing efficiency.

4.2 Design and ground-state electronic interaction studies of electron donor-acceptor sensors

The fundamental design of a $^1O_2$ molecular sensor is composed of a $^1O_2$ trapping moiety and a fluorescence reporter moiety in a chemically conjugated form. The inherent intramolecular electron transfer makes the sensor in a fluorescence *off* state. The $^1O_2$ mediated chemical modification leads to production of anthracene endoperoxide consequently blocking the intramolecular electron transfer to release the fluorescence from the fluorophore.[26,27] The promising $^1O_2$ sensors are based on substituted anthracene owing to appreciable thermal stability of anthracene endoperoxide compared to other aromatic endoperoxides.[26-32] To study the kinetics of $^1O_2$, three anthracene based fluorescent sensors of $^1O_2$ were used. First, **S1**, which is an aminocoumarin -anthracene conjugate, **S2** which is N-alkylated derivative of **S1** and a Rhodamine 6G-anthracene conjugate (**S3**), which was previously reported by Mingtai et al. [33] The structures of the sensors are shown in Figure 4.3.

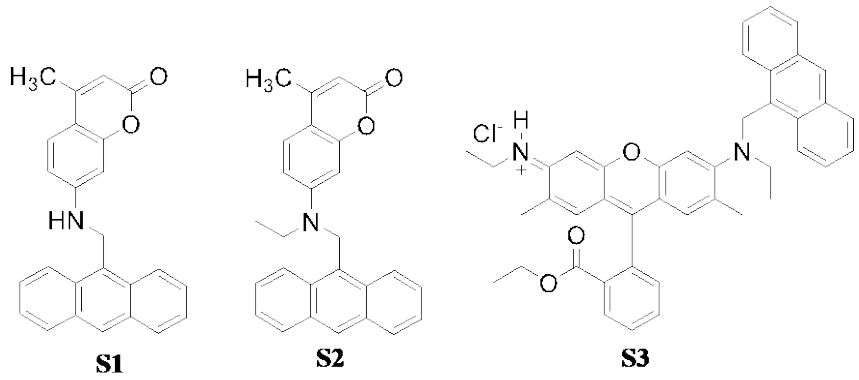

Figure 4.3. The structures of $^1O_2$ sensors in the present study.

In order to study the possible ground state electronic interactions between the anthracene part and the coumarin part in **S1**, the absorption spectra of the model compounds 9-methylanthracene (**A1**) and 7-propylamino,4-methyl-coumarin (**C1**) and the **S1** was examined. The structures and absorption spectra of the model compounds **A1** and **C1** are shown in Figure 4.4.

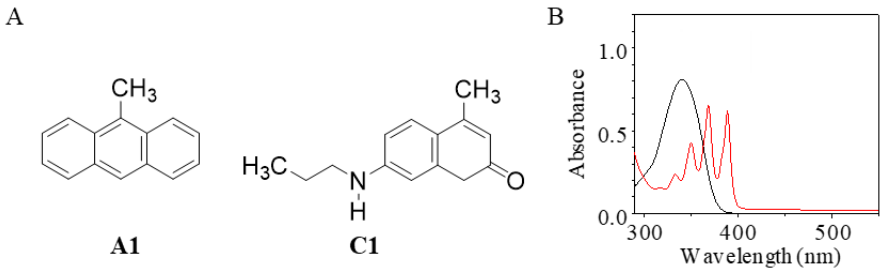

Figure 4.4. (A) Structures of model compounds **A1** and **C1**. (B) Absorption spectra of **A1** (red trace) and **C1** (black trace).

Figure 4.5 A shows the sum absorption spectrum of **A1** and **C1** (a trace in red) and the absorption of **S1** (a trace in black). An equal concentration of individual samples in DMF was prepared, and the absorption spectra was recorded. Although I expected the complete overlap of the absorption spectrum of **S1** with the sum absorption spectrum of **A1** and **C1**, the actual spectrum is redshifted (ca. 20 nm) without changing the anthracene vibrational bands. The slight redshift is assigned to the possible ground state electronic interactions between electron donor and acceptor in **S1**. A similar redshift was observed in the absorption spectrum of **S1** in a polar solvent (DMF) compared to that of in non-polar toluene, which further verified the assumption of electronic interaction.

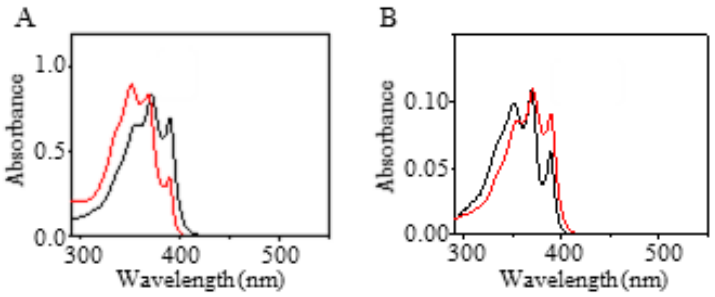

Figure 4.5. (A)The sum absorption spectra of **A1** and **C1** (red trace) and the absorption spectrum of **S1** (black trace) in DMF. (B) Absorption spectra of **S1** in toluene (black trace) and DMF (red trace).

4.3 Kinetics of singlet oxygen sensing using 9-substituted anthracene derivatives

The comprehensive kinetic study of sensing using 9-substituted anthracene derivates can help to rationalize the role of substituents on anthracene on the rate of $^1O_2$ sensing. To this purpose, the rate of $^1O_2$ sensing using three electron D-A systems, **S1**, **S2** and **S3** and compared the rate with that of the model compound, **A1**. In this study, $^1O_2$ was generated using conventional photosensitizers RB or TCPP. Monochromatic light sources were used to excite the PS, to calculate the concentration of $^1O_2$ produced per second in order to determine the second order photooxidation rates.

4.3.1 Singlet oxygen sensing by S1

The $^1O_2$ sensing by **S1** was studied using fluorescence and absorption spectroscopic techniques. To examine the $^1O_2$ sensing efficiency of **S1**, a photooxidation reaction of **S1** with $^1O_2$ generated by RB was demonstrated. A solution of **S1** and RB (2:1 molar ratio) was prepared and irradiated with a 532 nm laser at 50 mW cm^{-2}. Fluorescence and absorption spectra of the solution were recorded after every 5 min photosensitization for 60 min and ca. 20-fold increase in the fluorescence quantum efficiency of the sample was observed (Figure 4.6 A). The enhancement in fluorescence observed is attributed to reaction of nonfluorescent **S1** with $^1O_2$ and the formation of a highly fluorescent 9,10-endoperoxide of **S1** (Scheme 4.2).

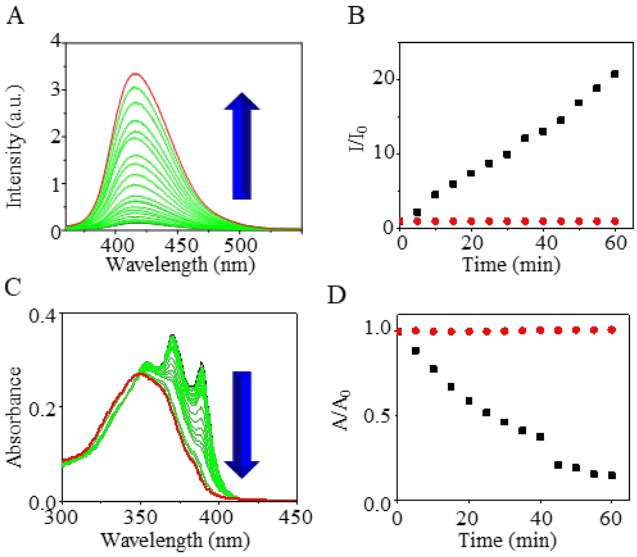

Figure 4.6. (A) Fluorescence (λ_{ex} 340 nm) and (C) absorption spectra of a solution of **S1** (10 μM) and RB (5μM) in DMF, before and after every 5 min intervals of photoactivation at 532 nm (50 $mWcm^{-2}$). (B) Time-traced relative fluorescence intensities and (D) relative absorbance of solutions of **S1** (10 μM) and RB (5μM) with (red trace) and without (black trace) NaN_3 (150 μM) in DMF.

The absorbance of the anthracene part in **S1** was decreased during photosensitization (Figure 4.6 C and 4.6 D). The transformation of **S1** to endoperoxide form caused the decrease in the anthracene bands. On the other hand, any fluorescence enhancement or decrease in the anthracene absorption were not observable for an equivalent solution supplemented with sodium azide (Figure 4.6 B and 4.6 D, a trace in red), which is an efficient $^1O_2$ scavenger.[34] Therefore, I confirmed that the 20-fold fluorescence enhancement of **S1** was originated from oxidation of **S1** by $^1O_2$.

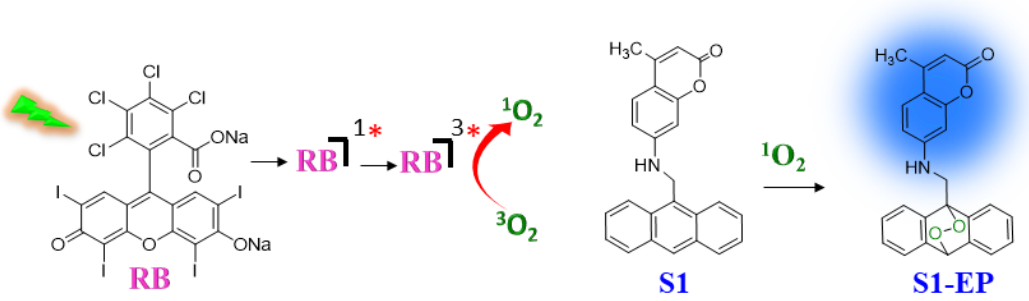

Scheme 4.2. A schematic representation of the RB-sensitized generation of $^1O_2$, and photooxidation of **S1** by $^1O_2$.

4.3.1.2 Mechanism of singlet oxygen mediated oxidation of S1

The photooxidation of a substrate by $^1O_2$ was extensively studied by Davidson et al. and formulated a second-order rate equation for the reaction of a substrate with $^1O_2$. [35] The overall photooxidation process proceeds through several stages, starting with photoexcitation of the sensitizer for the generation of $^1O_2$. Photoirradiation of the sensitizer activates it to the singlet excited state as depicted in Scheme 4.3. From the singlet excited state, it can either nonradiatively or radiatively (fluorescence) relax to ground state. However substantial ISC quantum yield of common PS leads to population of triplet excited state in large scale. The triplet state PS can transfer the excitation energy to ground state oxygen. The $^1O_2$ generated can either undergo nonradiative relaxation by interaction with solvent molecules or it can facilitate oxidation of a substrate in the given lifetime. The nonradiative relaxation of $^1O_2$ in solvent was described in terms of energy transfer from electronically excited oxygen to suitable overtones of solvent vibration. Kearns and co-workers proposed a Foster-type dipole-dipole interaction between $^1O_2$ and solvent molecules.[36] Alternatively, Schuster and co-workers proposed a relaxation mechanism based on exchange energy transfer.[37]

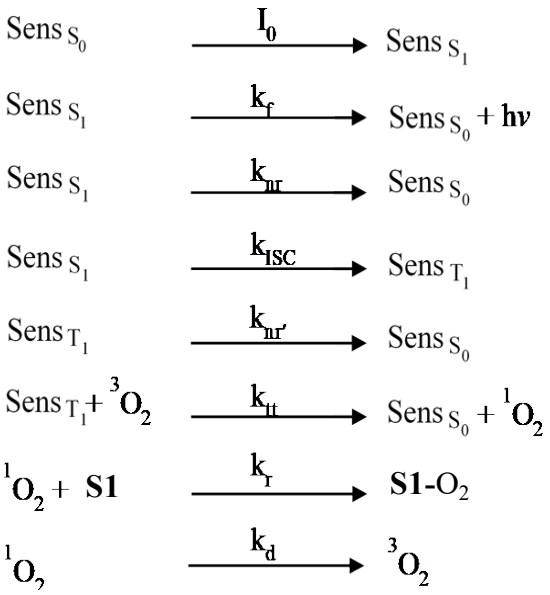

Scheme 4.3. Steps involved in photosensitized $^1O_2$ generation and photooxidation of **S1**. Here, k_f is the rate constant of radiative relaxation, k_{nr} is the rate constant of non-radiative relaxation, k_{ISC} is the rate constant of intersystem crossing, $k_{nr'}$ is the rate constant of non radiadive relaxation of sensitizer from triplet excited state, k_{tt} is the rate constant of photosensitization of molecular oxygen by triplet-triplet energy transfer, k_r is the rate constant of reaction of $^1O_2$ with **S1**, and k_d is the rate constant of nonradiative relaxation of $^1O_2$ by solvent molecules.

The photooxidation of anthracenes proceeds *via* addition of $^1O_2$ to the anthracene by a [4+2] cycloaddition. During the cycloaddition reaction, HOMO of the diene (anthracene) interacts with LUMO of the dienophile ($^1O_2$) forming corresponding endoperoxide. Aubry et al. proposed a single step concerted mechanism in which the addition of $^1O_2$ to the aromatic ring proceeds through a reversible formation of an exciplex in singlet excited state having substantial charge transfer from organic donor to oxygen. The solvated exciplex can either undergo chemical reaction to produce endoperoxide or endure ISC to avail a triplet state complex which would subsequently relax to the ground state (Figure 4.7).[38] Besides, alternative mechanisms have been proposed with emergence of biradical [39] or zwitterionic intermediates.[40] However, the actual mechanistic studies providing the direct evidence for the intermediate states needs further attention.

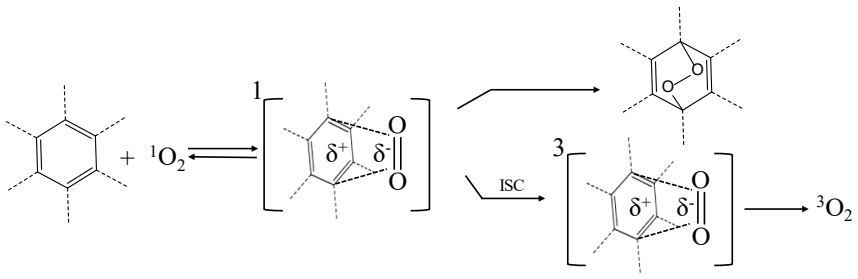

Figure 4.7. The proposed mechanism of [4+2] cycloaddition of $^1O_2$ to aromatic hydrocarbons. Ref 18.

The molecular sensor **S1** undergoes $^1O_2$ mediated photooxidation by a [4+2] cycloaddition to form corresponding endoperoxide and the details of characterization of the intermediate complex are discussed in the following chapter.

4.3.1.3 Kinetics of singlet oxygen sensing by S1

The second order rate of reaction of **S1** with $^1O_2$ was studied with the help of absorption spectroscopy. The rate constant for the reaction was determined using eq. 1 which is a modified second order rate equation in the integrated form, constructed according the previous report by Davidson et al. [35]

$$\ln\frac{C}{C_0} = k\,\frac{\{C_0 - C - (\Delta C_{singlet\ oxygen}\ t)\}}{k_d} \qquad (1)$$

where C_0 and C are concentration (in mol L^{-1}) of the sensor **S1** before and after photosensitization, respectively; $\Delta C_{\text{singlet oxygen}}$ is the concentration (8.86×10^{-8} M s^{-1}) of $^1O_2$ produced by RB with time. $\Delta C_{\text{singlet oxygen}}$ was calculated by estimating the number of photons (1.16×10^{17} s^{-1}) absorbed by RB per second; k is the second order rate constant which is estimated as the decrease of the substrate during the cycloaddition reaction; k_d is the rate constant (6.7×10^4 s^{-1} in DMF) [41] of deactivation of $^1O_2$ by the solvent; and t is the time of photosensitization in seconds.

Figure 4.8 shows the second order kinetic plot of the photooxidation of **S1** by $^1O_2$. The plot was constructed based on equation 1. Linear fitting of the data obtained from the

plot of $\ln\frac{C}{C_0}$ vs $\frac{\{C_0-C-(\Delta C_{singlet\ oxygen}\ t)\}}{k_d}$ provided the rate of $^1O_2$ sensing by **S1** at 3.4 × 10^8 M^{-1} s^{-1}.

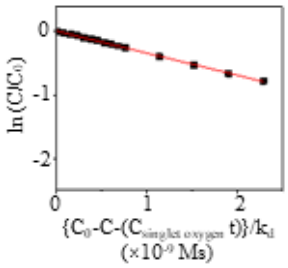

Figure 4.8. The second order kinetic plot of photooxidation of **S1** by $^1O_2$ constructed according to equation 1.

4.3.2 Kinetics of singlet oxygen mediated oxidation of A1

To correlate between the role of the substituent on anthracene and $^1O_2$ sensing efficiency of substituted anthracenes, the rate of reaction of **A1** with $^1O_2$ was evaluated and compared this rate with that of **S1**, both under identical experimental conditions and using the common photosensitizer RB.

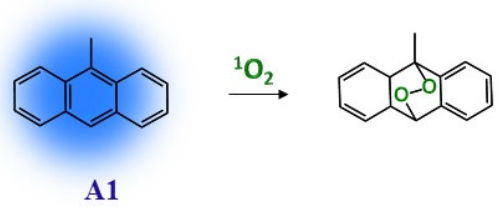

Scheme 4.4. The schematic representation of photooxidation of **A1** by $^1O_2$.

Upon continuous photoirradiation of RB at 532 nm (50 mW cm^{-2}) in a mixture of **A1** and RB, as shown in Figure 4.9 A and C, the fluorescence intensity and absorbance of **A1** decreased due to oxidation of **A1** by $^1O_2$ and the formation of a 9,10-endoperoxide

(Scheme 4.4). **A1** showed a 20-fold decrease in fluorescence intensity after 10 min photoirradiation of RB with a 532 nm laser (50 mW cm^{-2}). On the other hand, **S1** need 60 min of photosensitization or RB to show 20-fold fluorescence enhancement under identical condition. **A1** reacts with $^1O_2$ at a rate higher than that by **S1**. Likewise in the case of **S1**, the rate of reaction of **A1** with $^1O_2$ was estimated using eq. 1 and by plotting $\ln\frac{C}{C_0}$ *vs* $\frac{\{C_0-C-(\Delta C_{singlet\ oxygen}\ t)\}}{k_d}$ (Figure 4.9 D). By analyzing this second order kinetic plot, the reaction rate of **A1** was estimated at 3.3×10^9 M^{-1} s^{-1}, which is an order of magnitude greater than that of **S1**.

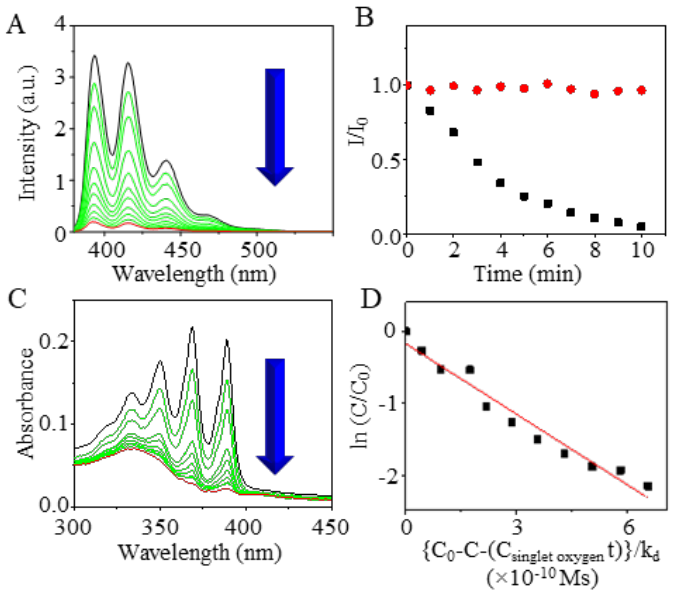

Figure 4.9. (A) Fluorescence spectra (λ_{ex} 350 nm) of a solution of **A1** (10 μM) and RB (5μM) in DMF, before and after every 1 min interval of photoactivation (532 nm, 50 mW cm^{-2}). (B) Time-traced relative fluorescence intensities of solutions of **A1** and RB (2:1 molar ratio) with (red traces) and without (black traces) NaN_3 (150 μM) in DMF. (C) The absorption spectra of a solution of **A1** (10 μM) and RB (10 μM) in DMF before and after every 1 min interval of photoactivation (532 nm, 50 mW cm^{-2}). (D) Second order kinetic plot of photooxidation of **A1** by $^1O_2$ constructed according to equation 1.

The electronic properties and steric aspects of the substituent are needed to be considered while studying the reactivity of the sensor to $^1O_2$. The notable difference in the rates of $^1O_2$ sensing by **S1** and **A1** can be correlated with electronic interaction

between anthracene and coumarin as well as the steric effect exerted by coumarin. Based on the absorption spectra (Figure 4.5), the anthracene moiety in **S1** supposed to be more electron rich than **A1**, due to the presence of aminocoumarin in **S1**. Certainly, with such an enhanced nucleophilicity of anthracene, the rate of reaction of **S1** with electrophilic $^1O_2$ is expected to be high. However, the reactivity of **A1** to $^1O_2$ is an order of magnitude greater than that of **S1**, suggesting that the coumarin substituent at the 9-position in **S1** minimizes any increased nucleophilicity of anthracene and decelerate the reaction between **S1** and $^1O_2$. In other words, the coumarin moiety in **S1**, when compared with a methyl group in **A1**, unfavourably affect the speed of $^1O_2$ sensing by **S1**.

4.3.3 Kinetics of singlet oxygen sensing by S2

In order to obtain additional information regarding the substituent effect on the rate of sensing, the structure of sensor **S1** was modified by alkylation of the nitrogen in the aminocoumarin part. The kinetics of $^1O_2$ sensing by the alkylated sensor (**S2**) was studied under the identical condition.

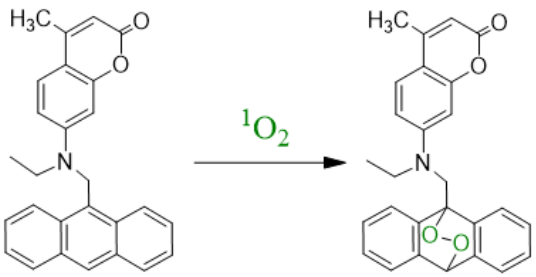

Scheme 4.5. The schematic representation of photooxidation of **S2** by $^1O_2$.

Upon continuous photoirradiation of RB at 532 nm (50 $mWcm^{-2}$) in a mixture of **S2** and RB, as shown in Figure 4.10 A, the fluorescence intensity monotonously increased due to oxidation of **S2** by $^1O_2$ and the formation of a 9,10-endoperoxide (Scheme 4.5). When compared with the 20-fold enhancement of fluorescence intensity (Figure 4.6A and 4.6B) for **S1**, after 60 min photoirradiation of RB with a 532 nm laser (50 $mWcm^{-2}$), the fluorescence intensity of **S2** was increased only by a factor of 6 (Figure 4.10 A and 4.10 B) under the identical condition. The reduction in the fluorescence response was due to

the lower reactivity of **S2** to $^1O_2$ compared to that of **S2**. The absorbance of anthracene in **S2** was decreased as time under photosensitization (Figure 4.10 C). A second order kinetic plot corresponding to the oxidation of **S2** by $^1O_2$ was constructed according to eq. 1. The linear fitting of the kinetic plot provided the $^1O_2$ sensing rate by **S2** at 1.6 $\times 10^8$ M^{-1} s^{-1}. The minor lessening in the rate of sensing in **S2** compared to **S1** is probably due to the steric factors as a consequence of alkylation.

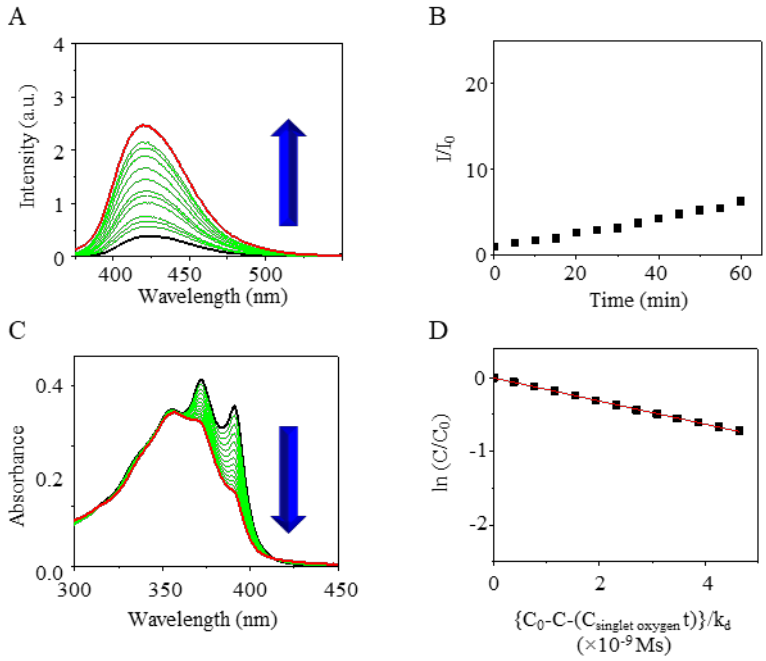

Figure 4.10. (A) Fluorescence spectra (λ_{ex} 340 nm) of a solution of **S2** (10 μM) and RB (5μM) in DMF, before and after every 5 min interval of photoactivation (532 nm, 50 mW cm^{-2}). (B) Time-traced relative fluorescence intensities of a solution of **S2** and RB (2:1 molar ratio). (C) The absorption spectra of a solution of **S2** (10 μM) and RB (10 μM) in DMF before and after every 5 min interval of photoactivation (532 nm, 50 mW cm^{-2}). (D) Second order kinetic plot of photooxidation of **S2** by $^1O_2$ constructed according to equation 1.

4.3.4 Kinetics of singlet oxygen sensing by S3

To verify of the substituent effects on the rate of $^1O_2$ sensing, the kinetics of $^1O_2$ sensing by a Rhodamine 6G-anthracene conjugate (**S3**) was studied. The effect of Rhodamine substituent on sensing was examined in this kinetics study. Due to the overlap of absorption spectrum of **S3** with the common photosensitizer RB, TCPP was employed as the $^1O_2$ generator in this case.

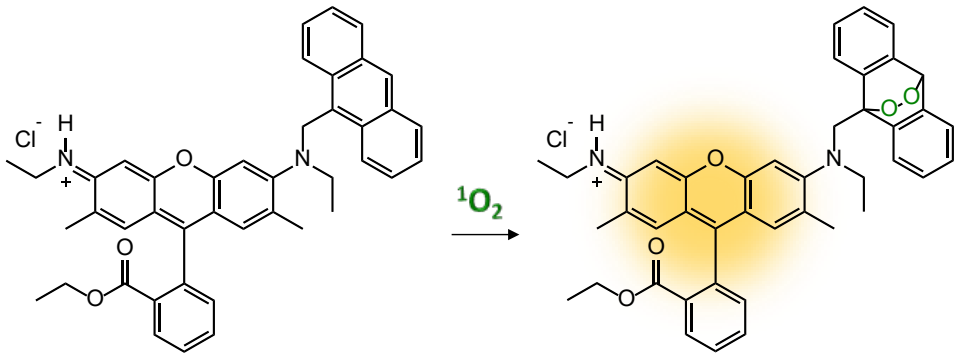

Scheme 4.6. The schematic representation of photooxidation of **S3** by $^1O_2$.

Upon continuous photoirradiation of TCPP at 405 nm (70 mW cm^{-2}) in a mixture of **S3** and TCPP, the fluorescence intensity is tremendously increased due to $^1O_2$ sensing (Figure 4.11 A). **S3** showed ca. 100-fold enhancement of fluorescence intensity (Figure 4.11 A and B) after 25 min photoirradiation of TCPP with 405 nm laser (70 mW cm^{-2}). The absorbance of anthracene in **S3** was decreased with time under photosensitization (Figure 4.17 C). $\Delta C_{\text{singlet oxygen}}$ (7.0×10^{-8} mol L^{-1} s^{-1}) was maintained comparable to the $^1O_2$ produced by RB in the previous studies. The second order kinetic plot corresponding to the oxidation of **S3** by $^1O_2$ was constructed according to eq. 1 (Figure 4.11 D). The linear fitting of the kinetic plot provided the $^1O_2$ sensing rate by **S3** at 1.9×10^8 M^{-1} s^{-1}. There is a minor decrease in the reactivity is compared to that of **S1** (3.4×10^8 M^{-1} s^{-1}). It is probably due to the steric factors associated with the larger rhodamine moiety than the coumarin moiety. This is consistent with the different rates reflect on the steric effect between **S1** and **A1** (3.3×10^9 M^{-1} s^{-1}) as mentioned above.

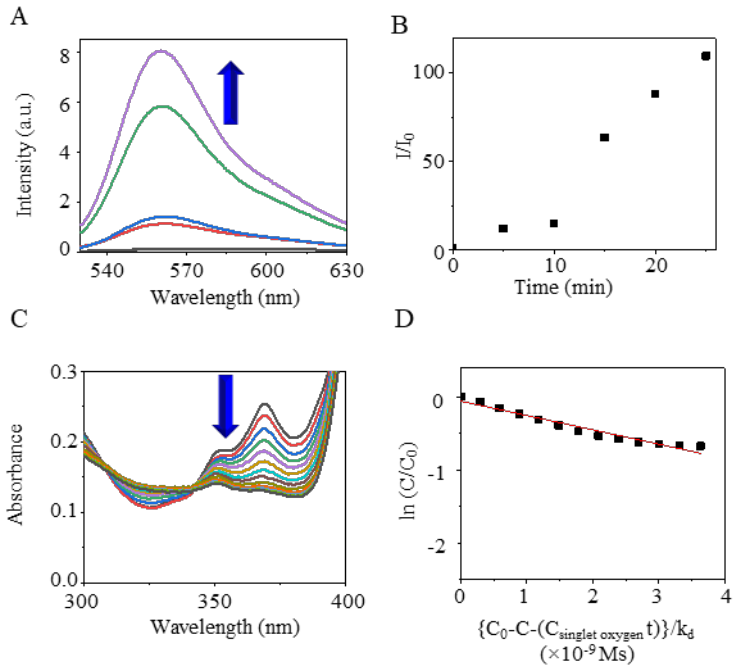

Figure 4.11. (A) Fluorescence spectra (λ_{ex} 500 nm) and (C) absorption spectra of a solution of **S3** (10 µM) and TCPP (5µM) in DMF, before and after every 5 min interval of photoactivation (405 nm, 70 mW cm^{-2}). (B) Time-traced relative fluorescence intensities of solutions of **S3** and TCPP (2:1 molar ratio). (D) Second order kinetic plot of photooxidation of **S3** by $^1O_2$ constructed according to equation 1.

4.4 Conclusions

The rate of $^1O_2$ sensing by fluorogenic sensors, anthracene–coumarin conjugates (**S1** and **S2**) and a Rhodamine 6G-anthracene conjugate (**S3**) was estimated and compared with that of 9-methylanthracene (**A1**). When compared to **A1**, all the three sensors show an order of magnitude reduced reactivity to $^1O_2$. The difference between the reactivities of **S1** and **A1** to $^1O_2$ can be correlated with the substituents (coumarin in **S1** and a methyl group in **A1**). Although coumarin enhances the nucleophilicity of anthracene part in **S1**, the rate of oxidation found less than that of **A1**. In order to verify the truncated reactivity, the role of the intermediate of the final product 9,10-endoperoxide, between **S1** or **A1** and $^1O_2$ on the $^1O_2$ sensing rate needs further attention.

References

1. Turrens, J. F. Mitochondrial Formation of Reactive Oxygen Species. *J. Physiol.* **2003**, *552* (2), 335–344.
2. Lin, G. G.; Scott, J. G. Ros Function in Redox Signaling. **2012**, *100* (2), 130–134.
3. Apel, K.; Hirt, H. REACTIVE OXYGEN SPECIES: Metabolism, Oxidative Stress, and Signal Transduction. *Annu. Rev. Plant Biol.* **2004**, *55* (1), 373–399.
4. DeRosa, M. C.; Crutchley, R. J. Photosensitized Singlet Oxygen and Its Applications. *Coord. Chem. Rev.* **2002**, *233–234*, 351–371.
5. Krasnovsky, A. A. Luminescence and Photochemical Studies of Singlet Oxygen Photonics. *J. Photochem. Photobiol. A Chem.* **2008**, *196* (2–3), 210–218.
6. Mulliken, R.S. Interpretation of the atmospheric oxygen bands; electronic levels of the oxygen molecule. *Nature*. **1928**, 122(3075), 505.
7. Kearns, D. R. Physical and Chemical Properties of Singlet Molecular Oxygen. *Chem. Rev.* **1971**, *71* (4), 395–427.
8. Weldon, D.; Poulsen, T. D.; Mikkelsen, K. V.; Ogilby, P. R. Singlet Sigma: The "Other" Singlet Oxygen in Solution. *Photochem. Photobiol.* **1999**, *70* (4), 369.
9. Schweitzer, C.; Mehrdad, Z.; Shafii, F.; Schmidt, R. Charge Transfer Induced Quenching of Triplet Sensitizers by Ground State Oxygen and of Singlet Oxygen by Ground State Sensitizers: A Common Deactivation Channel. *Phys. Chem. Chem. Phys.* **2001**, *3* (15), 3095–3101.
10. Redmond, R. W.; Gamlin, J. N. A Compilation of Singlet Oxygen Yields from Biologically Relevant Molecules. *Photochem. Photobiol.* **1999**, *70* (4), 391–475.
11. Figueiredo, T. L. C.; Johnstone, R. A. W.; SantAna Sørensen, A. M. P.; Burget, D.; Jacques, P. Determination of Fluorescence Yields, Singlet Lifetimes and Singlet Oxygen Yields of Water-Insoluble Porphyrins and Metalloporphyrins in Organic Solvents and in Aqueous Media. *Photochem. Photobiol.* **1999**, *69* (5), 517–528.
12. Khan, A. U.; Kasha, M. Red Chemiluminescence of Molecular Oxygen in Aqueous Solution. *J. Chem. Phys.* **1963**, *39* (8), 2105–2106.
13. Onyango, A. N. Endogenous Generation of Singlet Oxygen and Ozone in Human and Animal Tissues: Mechanisms, Biological Significance, and Influence of Dietary Components. *Oxid. Med. Cell. Longev.* **2016**.

14. Krinsky, N. I. Singlet Oxygen in Biological Systems. *Trends Biochem. Sci.* **1977**, *2* (2), 35–38.
15. Dolmans, D.E.; Fukumura, D.; Jain, R.K. Photodynamic therapy for cancer. Nat. Rev. Can. **2003**, 5, 380-387.
16. Shi, X.; Zhang, C. Y.; Gao, J.; Wang, Z. Recent Advances in Photodynamic Therapy for Cancer and Infectious Diseases. *Wiley Interdiscip. Rev. Nanomedicine Nanobiotechnology* **2019**, No. April, 1–23.
17. Park, W.; Cho, S.; Han, J.; Shin, H.; Na, K.; Lee, B.; Kim, D. H. Advanced Smart-Photosensitizers for More Effective Cancer Treatment. *Biomater. Sci.* **2018**, *6* (1), 79–90.
18. Park, W.; Cho, S.; Han, J.; Shin, H.; Na, K.; Lee, B.; Kim, D. H. Advanced Smart-Photosensitizers for More Effective Cancer Treatment. *Biomater. Sci.* **2018**, *6* (1), 79–90.
19. Park, W.; Cho, S.; Han, J.; Shin, H.; Na, K.; Lee, B.; Kim, D. H. Advanced Smart-Photosensitizers for More Effective Cancer Treatment. *Biomater. Sci.* **2018**, *6* (1), 79–90.
20. Baptista, M. S.; Cadet, J.; Di Mascio, P.; Ghogare, A. A.; Greer, A.; Hamblin, M. R.; Lorente, C.; Nunez, S. C.; Ribeiro, M. S.; Thomas, A. H.; et al. Type I and Type II Photosensitized Oxidation Reactions: Guidelines and Mechanistic Pathways. *Photochem. Photobiol.* **2017**, *93* (4), 912–919.
21. Castano, A. P.; Demidova, T. N.; Hamblin, M. Mechanisms in Photodynamic Therapy: Part One. *Photodiagnosis Photodyn Ther* **2004**, *1* (4), 279–293.
22. Jiménez-Banzo, A.; Ragàs, X.; Kapusta, P.; Nonell, S. Time-Resolved Methods in Biophysics. 7. Photon Counting vs. Analog Time-Resolved Singlet Oxygen Phosphorescence Detection. *Photochem. Photobiol. Sci.* **2008**, *7* (9), 1003–1010.
23. Hasebe, N.; Suzuki, K.; Horiuchi, H.; Suzuki, H.; Yoshihara, T.; Okutsu, T.; Tobita, S. Absolute Phosphorescence Quantum Yields of Singlet Molecular Oxygen in Solution Determined Using an Integrating Sphere Instrument. *Anal. Chem.* **2015**, *87* (4), 2360–2366.
24. Lion, Y.; Delmelle, M.; Van De Vorst, A. New Method of Detecting Singlet Oxygen Production. *Nature* **1976**, 263(5576), 442.

25. Nardi, G.; Manet, I.; Monti, S.; Miranda, M. A.; Lhiaubet-Vallet, V. Scope and Limitations of the TEMPO/EPR Method for Singlet Oxygen Detection: The Misleading Role of Electron Transfer. *Free Radic. Biol. Med.* **2014**, *77*, 64–70.
26. Naoki, U.; Kumi, T.; Yasuteru, U.; Kazuya, K.; Tsunehiko, H.; Tetsuo, N. Novel Fluorescent Probes for Singlet Oxygen. *Angew. Chemie Int. Ed.* **1999**, *38* (19), 2899–2901.
27. Tanaka, K.; Miura, T.; Umezawa, N.; Urano, Y.; Kikuchi, K.; Higuchi, T.; Nagano, T. Rational Design of Fluorescein-Based Fluorescence Probes. Mechanism-Based Design of a Maximum Fluorescence Probe for Singlet Oxygen. *J. Am. Chem. Soc.* **2001**, *123* (11), 2530–2536.
28. Kim, S.; Tachikawa, T.; Fujitsuka, M.; Majima, T. Far-Red Fluorescence Probe for Monitoring Singlet Oxygen during Photodynamic Therapy. *J. Am. Chem. Soc.* **2014**, *136* (33), 11707–11715.
29. Pedersen, S. K.; Holmehave, J.; Blaikie, F. H.; Gollmer, A.; Breitenbach, T.; Jensen, H. H.; Ogilby, P. R. Aarhus Sensor Green: A Fluorescent Probe for Singlet Oxygen. *J. Org. Chem.* **2014**, *79* (7), 3079–3087.
30. Flors, C.; Fryer, M. J.; Waring, J.; Reeder, B.; Bechtold, U.; Mullineaux, P. M.; Nonell, S.; Wilson, M. T.; Baker, N. R. Imaging the Production of Singlet Oxygen in Vivo Using a New Fluorescent Sensor, Singlet Oxygen Sensor Green®. *J. Exp. Bot.* **2006**, *57* (8), 1725–1734.
31. Kim, S.; Fujitsuka, M.; Majima, T. Photochemistry of Singlet Oxygen Sensor Green. *J. Phys. Chem. B* **2013**, *117* (45), 13985–13992.
32. Kohara, R.; Yuyama, K.; Shigeri, Y.; Biju, V. Blue-Emitting Electron-Donor / Acceptor Dyads for Naked- Eye Fluorescence Detection of Singlet Oxygen. *ChemPhotoChem*. **2017**, 1(7), 299–303.
33. Sun, M.; Krishnakumar, S.; Zhang, Y.; Liang, D.; Yang, X.; Wong, M. W.; Wang, S.; Huang, D. Singlet Oxygen Probes Made Simple: Anthracenylmethyl Substituted Fluorophores as Reaction-Based Probes for Detection and Imaging of Cellular $^1O_2$. *Sensors Actuators, B Chem.* **2018**, *271* (May), 346–352.
34. Haag, W. R.; Mill, T. Rate Constants for Interaction of $^1O_2$ ($^1\Delta_g$) with Azide ion in Water. *Photochem. Photobiol.* **1987**, *45* (3), 317–321.

35. Stephen Davidson, R.; Trethewey, K. R. Factors Affecting Dye-Sensitised Photo-Oxygenation Reactions. *J. Chem. Soc. Perkin Trans. 2* **1977**.
36. Merkel, P. B.; Kearns, D. R. Radiationless Decay of Singlet Molecular Oxygen in Solution. An Experimental and Theoretical Study of Electronic-to-Vibrational Energy Transfer. *J. Am. Chem. Soc.* **1972**, *94* (21), 7244–7253.
37. Hurst, J. R.; Schuster, G. B. Nonradiative Relaxation of Singlet Oxygen in Solution. *J. Am. Chem. Soc.* **1983**, *105* (18), 5756–5760.
38. Aubry, J. M.; Pierlot, C.; Rigaudy, J.; Schmidt, R. Reversible Binding of Oxygen to Aromatic Compounds. *Acc. Chem. Res.* **2003**, *36* (9), 668–675.
39. Zehm, D.; Fudickar, W.; Linker, T. Molecular Switches Flipped by Oxygen. *Angew. Chemie - Int. Ed.* **2007**, *46* (40), 7689–7692.
40. Castro-Olivares, R.; Günther, G.; Zanocco, A. L.; Lemp, E. Linear Free Energy Relationship Analysis of Solvent Effect on Singlet Oxygen Reactions with Mono and Disubstituted Anthracene Derivatives. *J. Photochem. Photobiol. A Chem.* **2009**, *207* (2–3), 160–166.
41. Wilkinson, F.; Helman, W. P.; Ross, A. B. Rate Constants for the Decay and Reactions of the Lowest Electronically Excited Singlet State of Molecular Oxygen in Solution. An Expanded and Revised Compilation. *J. Phys. Chem. Ref. Data* **1995**.

Chapter 5

Mechanism of Singlet Oxygen Reaction

Abstract: In chapter 4, the singlet oxygen sensing efficiency of anthracene-based fluorescence sensors is examined in terms of the rate of cycloaddition reaction with $^1O_2$. I found an order of magnitude less rate than the model compound 9-methylanthracene. The attenuated reactivity causes an adverse impact on the sensitivity of the probe, limiting the fluorescence response. Although, several anthracene-based fluorogenic sensors are reported, the roles of the intermediate complex on the rate of sensing remains unknown. Here, I validate the role of the intermediate state on the $^1O_2$ sensing efficiency of a fluorescence sensor, **S1**, and attempt to improve the efficiency by activating the intermediate. In this chapter, I demonstrate that **S1** traps $^1O_2$ generated by a photosensitizer to form an intermediate that can be activated by the UV light and enhance the sensitivity of $^1O_2$ detection. I characterize the intermediate and its reactivity using absorption spectroscopy, fluorescence spectroscopy, electron paramagnetic resonance spectroscopy and NMR spectroscopy. The UV activation substantially enhances the efficiency of sensing and facilitates faster fluorescence sensing. On the other hand, the organelle-specific localization and invitro $^1O_2$ sensing during photodynamic action inside Hela cells are demonstrated using the Rhodamine 6G- anthracene conjugate (**S3**).

5.1 Introduction

By considering the biological and clinical impact of $^1O_2$, various fluorescence sensors have been developed, among them anthracene-based fluorescence sensors have attracted immense attention due to the excellent features such as high selectivity and sensitivity of anthracene towards $^1O_2$.[1-6] Nevertheless, there are a very few efforts carried-out to improve the sensitivity of the detection. The essential factors affecting the efficiency of $^1O_2$ sensing are the rate of reactions of $^1O_2$ with the anthracene receptor, fluorescence quantum yield of the reporter, efficiency of electron transfer in the molecular sensor, and the concentration and lifetime of $^1O_2$ in the prevailing medium. All these factors are needed to be examined during the application of the sensing prob. The high efficiency and sensitivity of the sensor are critical for the detection of $^1O_2$ during PDT since the sensing process must be accomplished within the time interval of the therapy. The reported fluorescence sensors demand a long time of photoactivation of the photosensitizer to give the saturated fluorescence response, which in turn leads to undesirable oxidative damage of the common photosensitizers. [1-6]

For example, the fluorescence sensors with xanthene derivatives as fluorescence reporter shows the fluorescence quantum efficiency noticeably less than the non-conjugated xanthene.[1] The cell-permeable and NIR emitting Si-DMA shows considerably less fluorescence quantum efficiency after $^1O_2$ mediated oxidation (0.17) compared to the reference molecule, Silicon-Rhodamine (0.42).[2] Furthermore, the fluorescence quantum efficiency of the molecule of my interest, coumarin-anthracene conjugate, **S1** ($\phi_F = 0.30$), is lower than the reference compound, Coumarin-120 ($\phi_F = 0.63$).[5] Therefore, the factors that limit tallying the absolute quantum yield of the fluorescence sensor is needed to be investigated systematically. One of the reasons behind low ϕ_F can be the reduced reactivity of the intermediate formed during the [4+2] cycloaddition reaction of $^1O_2$ to anthracene. In this work, I investigate the UV-induced activated reaction of the long-lived intermediate complex, which resulted in an enormous enhancement of fluorescence intensity. The activated reaction improves the efficiency of sensing. Furthermore, it opens up a possibility of delayed fluorescence sensing, providing temporal control over sensing activity.

5.2 UV-induced fluorescence enhancement during singlet oxygen sensing

The low rate of $^1O_2$ sensing by molecular sensor, **S1** impelled me to investigate the factors affecting the reactivity of **S1** to $^1O_2$, to improve the sensing efficiency. I found an enormous enhancement in the fluorescence intensity of **S1** by irradiation with UV light immediate to the photosensitization process. The change in fluorescence was appreciably high to observe with naked eye. A solution containing **S1** and RB (2:1 molar ratio) was irradiated with a 532 nm laser at 50 mW cm^{-2} to generate $^1O_2$. Immediate to the photosensitization, the sample solution was irradiated with a handheld UV lamp (1 mW cm^{-2}). Figure 5.1 A shows fluorescence spectra of **S1** recorded as a function of time under photosensitization of RB. After 30 min of photosensitization, the sample solution was irradiated with low intensity UV light (1 mW cm^{-2}) for 3 min.

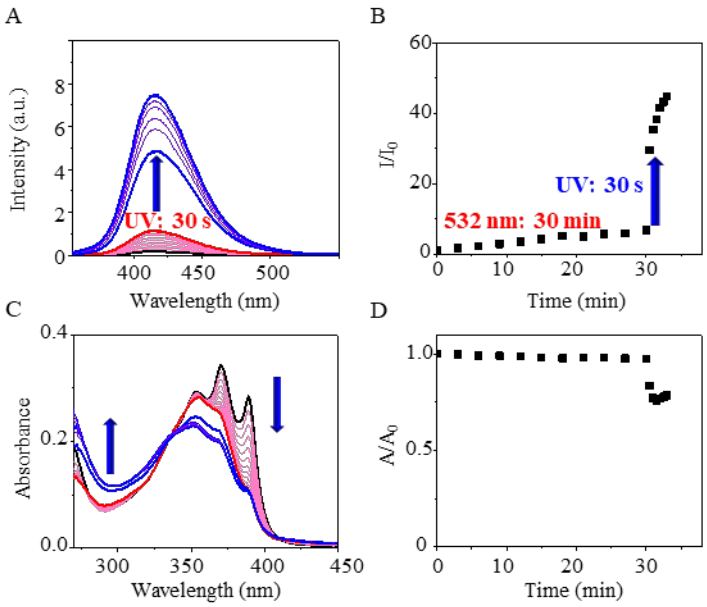

Figure 5.1. (A) Fluorescence (λ_{ex}=340 nm)and (C) absorption spectra of a solution of **S1** (10 μM) and RB (2:1 molar ratio) in DMF before and after every 5 min of photosensitization (λ=532 nm, 50 mW cm^{-2}) and photoactivation with UV (365 nm, 1 mW cm^{-2}) (B) Time-traced relative fluorescence intensities (at λ=420 nm). (D) Time-traced relative absorbance (at λ=370 nm).

Surprisingly, a huge enhancement in the fluorescence intensity was detected. ~5-fold enhancement in the fluorescence intensity was occurred within 30 s of illumination with the handheld UV lamp. Furthermore, the enhancement factor was further increased to 7-fold by the additional 2 min of UV illumination (Figure 5.1 B). Similar trends were visible in the absorption spectra. There is a sudden drop in the wavelength region were absorbance of anthracene (330-400 nm). The noticeable increase in the absorbance below 300 nm points out the formation of the endoperoxide of **S1** since the anthracene endoperoxides predominantly absorbs in the UV B wavelength region (Figure 5.1 C).[7] The enhanced fluorescence and reduced absorption features refers to the UV activated reaction of $^1O_2$ with **S1** leading to the formation of the endoperoxide at a higher rate. Here, I hypothesize the existence of an intermediate which is in an inactive state, and the surplus amount of energy supplied by the UV illumination stimulates the intermediate, activating the unimolecular reaction of the complex to form the endoperoxide.

The UV induced fluorescence enhancement found to be extremely sensitive. Even the UV light used for spectral measurement in the fluorescence spectrometer enhances the fluorescence intensity to greater extent. After the photosensitization, the fluorescence spectra of **S1** was continuously recorded. The fluorescence intensity of **S1** was increased to 2-fold within 5 measurements. By considering this point, the number of measurements during photosensitization was decreased. Then, the UV effect exhibited by **S1** increased to 7-fold within 30 s of UV illumination with the handheld lamp after photosensitization.

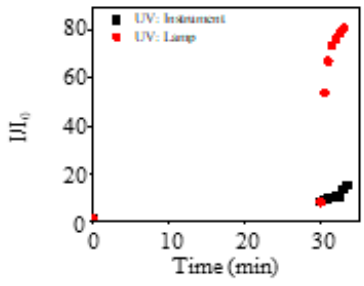

Figure 5.2. Time-traced relative fluorescence intensities (at λ=420 nm) of DMF solution of **S1** (10 μM) and RB (2:1 molar ratio) before and after photosensitization (λ=532 nm, 50 mW cm^{-2}) for 30 min followed by photoactivation with UV lamp (red trace) and under continuous fluorescence monitoring in the spectrometer (black trace).

5.3 The effect of singlet oxygen scavenger on UV-induced fluorescence enhancement

To verify the involvement of $^1O_2$ in the UV activated reaction of the intermediate, experiments were conducted in the presence of the $^1O_2$ quencher sodium azide. Azide anions are well known physical quencher of $^1O_2$ and often employed to verify the participation of $^1O_2$ in the oxidation reactions.[9] A solution of **S1** and RB in DMF supplemented with 15 equivalent of sodium azide (NaN_3) was irradiated with 532 nm laser. After 30 min of photosensitization the sample solution was illuminated with UV light. From Figure 5.3 A and B, it is obvious that the photooxidation of **S1** is diminished since there is no fluorescence enhancement under the action of 532 nm laser.

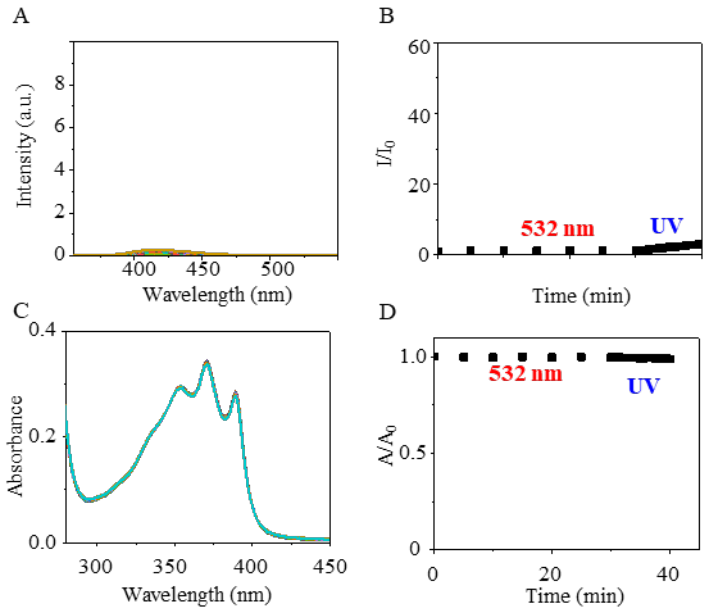

Figure 5.3. (A) Fluorescence and (C) absorption spectra of a solution of sensor **S1** (10 μM) and RB (2:1 molar ratio) in DMF in the presence of $^1O_2$ scavenger NaN_3 before and after every 5 min of photosensitization (λ=532 nm, 50 mW cm^{-2}) and photoactivation with UV (365 nm, 1 mW cm^{-2}) (B) Time-traced relative fluorescence intensities (at λ=420 nm). (D) Time-traced relative absorbance (at λ=370 nm).

The efficient quenching of $^1O_2$ generated by RB was accomplished by the azide ion. The inhibition of photooxidation of **S1** by $^1O_2$ is further verified by the intact absorption spectra monitored (Figure 5.3 C and 5.3 D). Besides, the action of UV light did not cause any significant enhancement in the fluorescence. The insignificant increase

in fluorescence during UV illumination is attributed to the dimerization of **S1**.[5] The lack of substantial fluorescence enhancement during the UV activation in the presence of NaN_3 confirms the intermediacy of $^1O_2$ in the UV activated reaction.

Although, when the scavenger was added to the sample solution after the photosensitization and prior to UV activation, unexpectedly, the enhancement in fluorescence was resumed. The fluorescence spectra and absorption spectra are shown in Figure 5.4. A fluorescence enhancement by a factor of 6 was obtained during 30 s of UV illumination. A control experiment was conducted under identical condition without adding NaN_3 and 30 s of UV illumination elicited ca. 8-fold fluorescence enhancement. However, the fluorescence enhancement observed during total of 3 min of UV illumination in the presence of NaN_3 is moderately less than the control experiment.

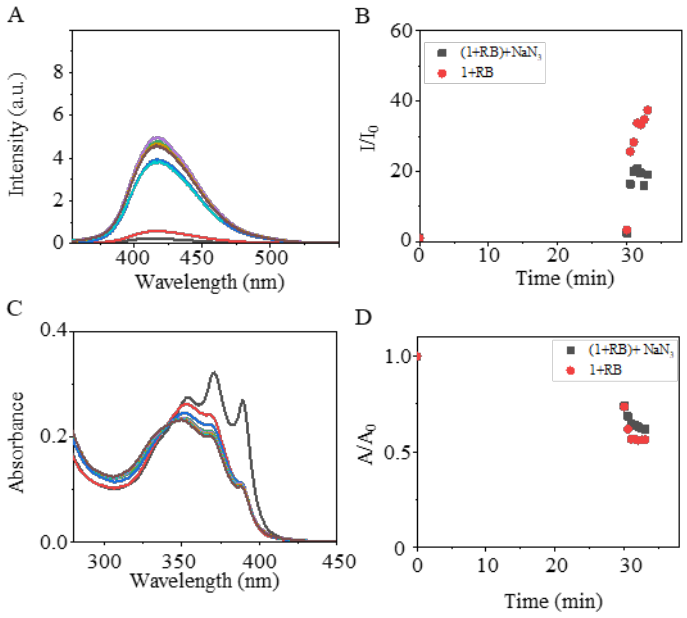

Figure 5.4. (A) Fluorescence and (C) absorption spectra of a solution of **S1** (10 μM) and RB (2:1 molar ratio) in DMF before and after the photosensitization (λ=532 nm, 50 mW cm^{-2}) for 30 min, then the $^1O_2$ scavenger, NaN_3 (150 μM) was added and photoactivated with UV (365 nm, 1 mW cm^{-2}) (B) Time-traced relative fluorescence intensities (at λ=420 nm), the black traces represents the fluorescence response of the sample solution containing NaN_3 and the red traces correspond to the control experiment . (D) Time-traced relative absorbance (at λ=370 nm).

The fluorescence response as the function of UV illumination and the presence of a the $^1O_2$ scavenger suggest that the intermediate complex is appreciably stable towards the $^1O_2$ scavenger. Nevertheless, the reasonable attenuation in enhancement factor suggests the existence of the intermediate complex in which the $^1O_2$ is probably trapped. The UV illumination activates the complex to undergo rearrangement to produce the endoperoxide. In the meanwhile, NaN_3 scavenges some portion of the trapped $^1O_2$, causing reduction in the fluorescence intensity compared to an experiment conducted without the scavenger. The diminished reactivity of the intermediate complex in the presence of the $^1O_2$ scavenger was further verified from the reduced absorbance during the UV activation (Figure 5.4 C and 5.4 D).

5.4 The stability of the intermediate complex

The stability of the intermediate complex was evaluated by inspecting the fluorescence response by activating the intermediate by UV light with a time delay after the photosensitization. A sample solution of **S1** (10 μM) in 5 μM solution of RB was prepared. The sample was illuminated with 532 nm laser for 30 min. Thereafter, illuminated with UV with a delay of 2 min, 4 min, 6 min, 8 min, and 10 min. Interestingly, the fluorescence responses were comparable in each case (Figure 5.5 A). The similar fluorescence response during the UV action on the intermediate complex over 10 min time delay points out the significant stability of the intermediate complex. This encouraged me to check the long-term stability. The photosensitized sample was illuminated with UV light after 5 h and 24 h. The UV-induced enhanced fluorescence was accessible even after a day suggesting the long lifetime of the intermediate complex (Figure 5.5 B). However, the intermediate is extremely sensitive to the light which restrict the separation of it from the reaction mixture.

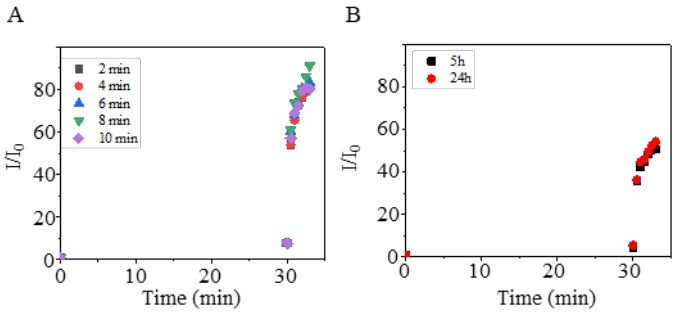

Figure 5.5. Time-traced relative fluorescence intensities (at λ=420 nm) of a DMF solution of **S1** (10 μM) and RB (2:1 molar ratio) before and after photosensitization (λ=532 nm, 50 mW cm^{-2}) followed by photoactivation with UV lamp after a time delay of 2-10 min. (B) The delay time is 5h (black trace) and 24h (red trace).

5.5.1 The role of substituent on the UV-induced fluorescence enhancement

The OH functionality in the molecular framework of the enes or dienes helps to coordinate with the incoming $^1O_2$ during the cycloaddition reactions by association interactions and leads to control the stereochemistry of the reaction.[13] In order to check whether any analogous interaction is occurring in the amine proton of **S1,** and $^1O_2$, I replaced the proton with ethyl group to make *N*-alkylated form of **S1**. In other words, to check the possibility of assistance of amine proton to trap $^1O_2$ through any non-covalent interaction such as H-bonding, the UV activated reaction was studied in the N-alkylated sensor, **S2**. The UV activated reaction of the **S2** was studied under the identical conditions as reported in the section 5.2. After 30 min of photosensitization by RB under 532 nm laser excitation, the solution containing **S2** and RB was illuminated with UV light. Within a minute of UV illuminations, the fluorescence response of the sensor was saturated. The absorbance of the samples also showed a sudden drop during UV illumination (Figure 5.6). These results rule out the assumption of the contribution of the amine proton to the UV-activated reaction.

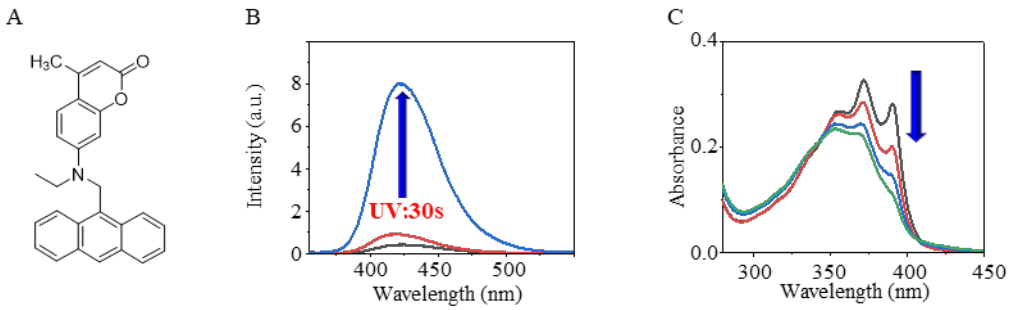

Figure 5.6. (A) The structure of **S2**. (B) Fluorescence and (C) absorption spectra of a solution of sensor **S2** (10 μM) and RB (2:1 molar ratio) in DMF before and after the photosensitization (λ=532 nm, 50 mW cm^{-2}) for 30 min, followed by photoactivation with UV (365 nm, 1 mW cm^{-2}) for 1 min.

5.5.2 Examination of UV effect on Rhodamine 6G-anthracene conjugate (S3)

To evaluate the role of coumarin in the UV induced activated reaction, the substituent at 9-position of anthracene was replaced with Rhodamine 6G. Figure 5.7 A shows the fluorescence spectra of **S3** in DMF supplemented with TCPP plotted as the function of time under photosensitization. After 60 min of photosensitization, the sample solution was illuminated with UV light. However, UV illumination did not lead to markedly high fluorescence (Figure 5.7 A and 5.7 C). From the absorption features, it is clear that the rate of reaction during photosensitization was somewhat reduced during UV illumination (Figure 5.7 B and 5.7 D). Therefore, it was verified that the coumarin substitution is a requisite to elicit UV-activated reaction. The exact role of the coumarin in the UV effect remains curious.

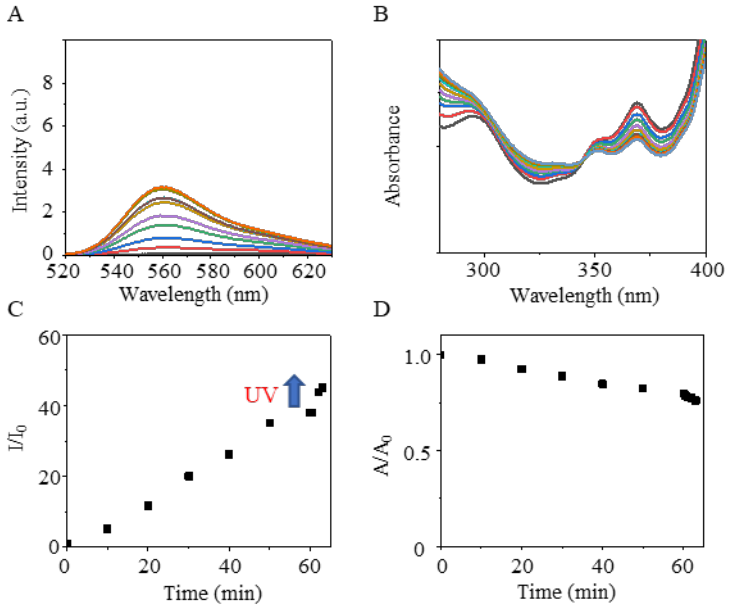

Figure 5.7. (A) Fluorescence and (B) absorption spectra of a solution of sensor **S3** (10 μM) and TCPP (2:1 molar ratio) in DMF before and after the photosensitization (Xenon lamp fitted with 410-430 nm bandpass filter, 10 mW cm^{-2} at 420 nm) for 60 min, followed by photoactivation with UV (365 nm, 1 mW cm^{-2}) for 3 min. (C) Time-traced relative fluorescence intensities (at λ= 560 nm). (D) Time-traced relative absorbance (at λ=370 nm).

5.6 EPR studies of UV activated reaction of singlet oxygen and S1

EPR spectroscopy is one of the widely used techniques to study the reactions facilitated by $^1O_2$.[14] EPR is an indirect method to detect the presence of $^1O_2$ by chemically-trapping it by a sterically hindered amine as the prob. The oxidation of the probe produces paramagnetic N-oxyl radical which gives a significant EPR signal (Figure 5.8). The sensitivity of this method is appreciable since EPR signals from even 10^{-7} M of nitroxide radical can be detected.[14] In the present study, I applied EPR spectroscopic technique to account for the role of $^1O_2$ in the UV-activated reaction of a complex between $^1O_2$ and **S1**. Therefore, I carried out the UV-activated reaction of **S1** in the presence of the photosensitizer RB and the prob 2,2,6,6-tetramethylpiperidine (TEMP), and analysed the EPR signals from the 2,2,6,6- tetramethylpiperidine-1-oxyl radical (TEMPO).

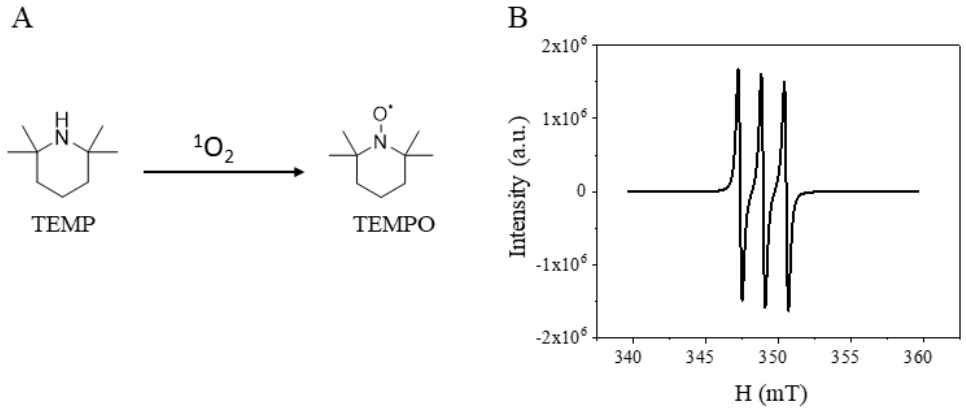

Figure 5.8. A scheme for oxidation of TEMP by $^1O_2$ to produce TEMPO. B) EPR spectra of 5 mM of TEMPO in DMF.

Initially, I optimized the measurement conditions by analysing the generation $^1O_2$ by photosensitization of RB in the presence of TEMP. To this purpose, 5 mM of TEMP was added to 5 μM RB in DMF. The solution was irradiated with a Xenon lamp fitted with >480 nm long-pass filter for 30 min. The power of the light source was set at 50 mW cm^{-2} at 532 nm. After the photosensitization, EPR spectra of the sample solution was recorded using X band frequency of microwave (9.79 GHz) at 1 mW cm^{-2} power. In parallel, an equivalent solution was illuminated with a UV LED with emission maximum at 365 nm, at 2 mW cm^{-2} for 10 min.

The significant enhancement in the EPR signal in the Figure 5.9 B after 30 min of illumination (Xenon lamp) shows the $^1O_2$ generation and subsequent oxidation of TEMP to produce TEMPO. However, the UV illumination of RB did not cause any significant increase in the EPR signal, which indicates the insignificant generation $^1O_2$ of by RB under the UV illumination. This observation supports that the UV-activated reaction of **S1** is not caused by $^1O_2$ generated by UV illumination; the absorbance of RB at 365 nm is extremely low (Figure 5.9 C).

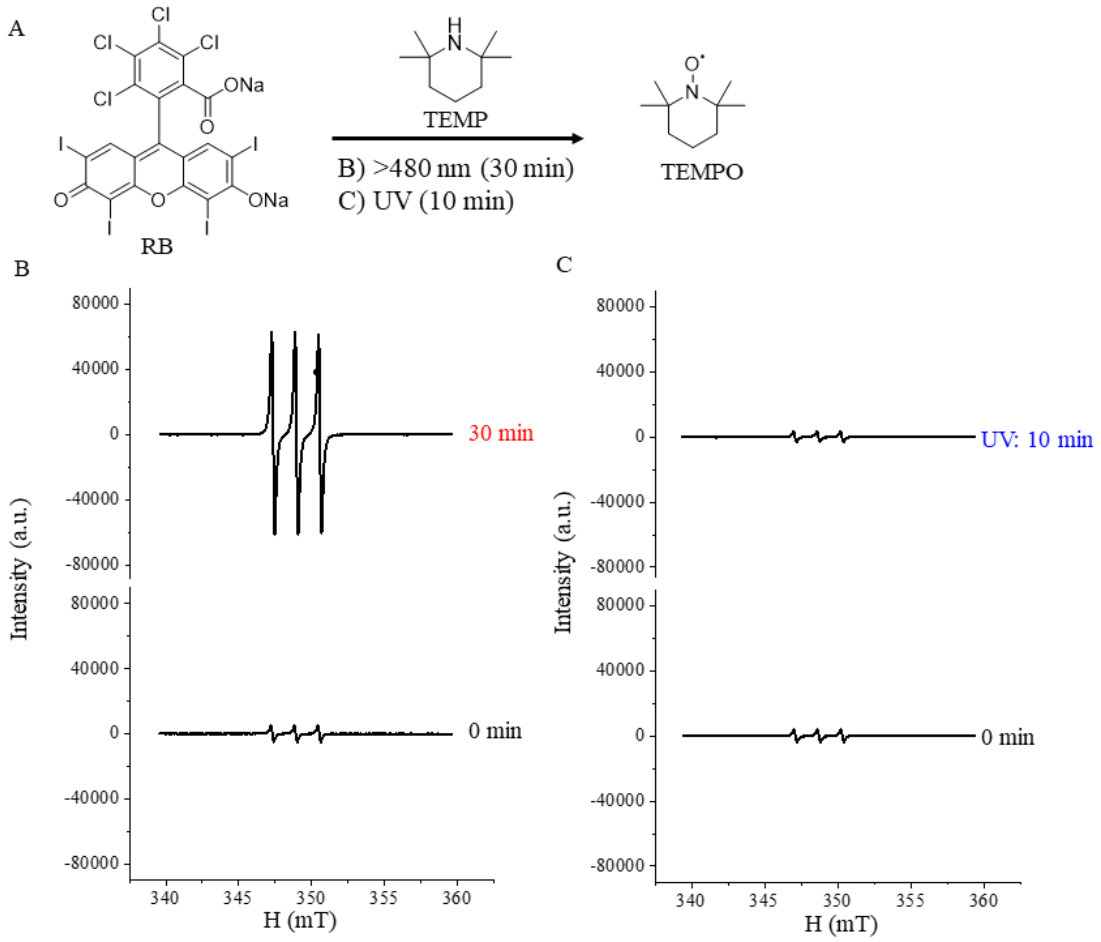

Figure 5.9. (A) A scheme of the experiment. The EPR spectra of a solution containing 5 µM RB and 5 mM TEMP in DMF before and after (B) 30 min illumination with Xenon lamp (>480 nm long pass filter, 50 mW cm^{-2}) and (C) 10 min illumination with a UV LED (365 nm, 2 mW cm^{-2}).

Then, I examined whether the sensor, **S1** itself generates $^1O_2$ under the UV illumination. To this purpose, I illuminated a DMF solution containing 10 µM of **S1** in the presence of 5 mM of TEMP with UV for 10 min. The EPR spectra recorded before and after 10 min UV illumination is shown in Figure 5.10. There wasn't any significant change in the EPR signal intensity during the UV illumination. Therefore, I excluded the possibility of self-sensitization by **S1** molecule.

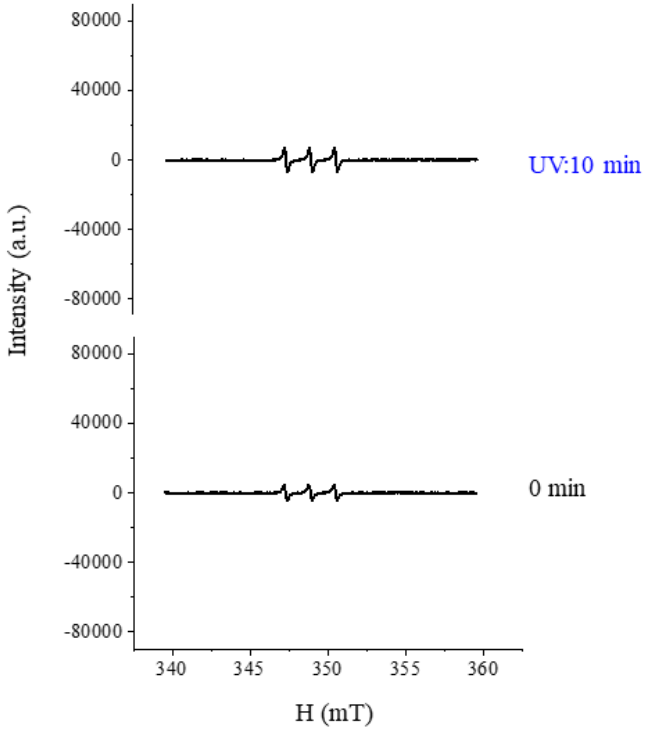

Figure 5.10. EPR spectra of a solution containing 10 µM of **S1** and 5mM TEMP in DMF before and after 10 min of illumination with UV LED (365 nm, 2 mW cm^{-2}).

In order to examine the UV-activated reaction of the intermediate complex, the procedure was slightly modified. First, I prepared a sample solution of 10 µM of **S1** and 5 µM of RB in DMF. The solution was irradiated with the Xenon lamp for 30 min. Then, 5 mM of TEMP was added to the solution containing the intermediate complex and EPR spectra was recorded. Afterwards, the solution was illuminated with UV light for 10 min and the EPR spectra was recorded.

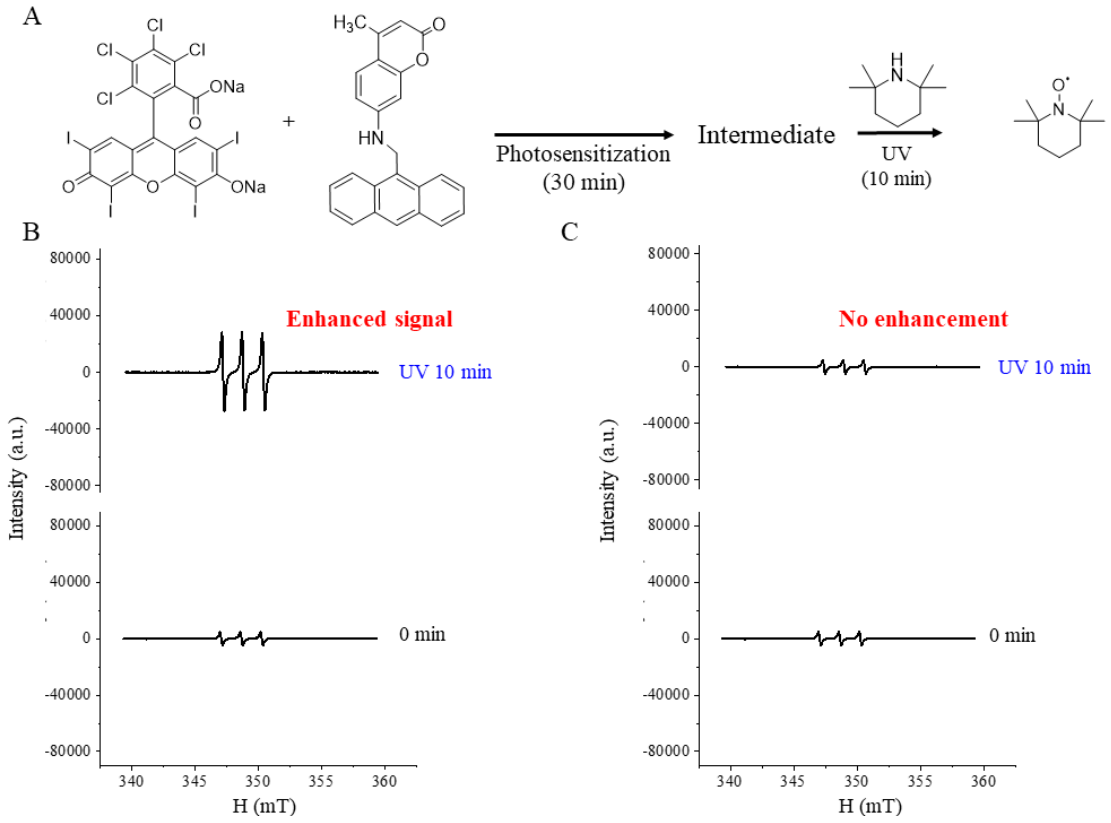

Figure 5.11. (A) A scheme of experiment involving trapping of $^1O_2$ and its scavenging with TEMP. (B) A sample solution of **S1** and RB (2:1) was illuminated under xenon lamp for 30 min (>480 nm long-pass filter, 50 mW cm^{-2}) and then, 5 mM of TEMP was added. B) the EPR spectra of the sample recorded before and after 10 min of illumination with UV LED (365 nm, 2 mW cm^{-2}). (C) The control experiment conducted by 10 min of UV illumination (365 nm, 2 mW cm^{-2}) of a solution of **S1** and RB (2:1) and 5 mM of TEMP.

A remarkable enhancement in the EPR signal was observed after 10 min of UV illumination (Figure 5.11 B). This signal response is ca. 50 % of the EPR signal enhancement observed during the photosensitization of RB (Figure 5.9 B). It is already verified that both RB and **S1** didn't exhibit enhancement in EPR signal under illumination (Figure 5.9 C and 5.10) which was further confirmed by conducting a control experiment of UV illumination of a solution containing **S1**, RB and TEMP. The EPR signal was intact before and after UV illumination (Figure 5.11 C). Therefore, it can be stated that the enhanced EPR signal is by the oxidation of TEMP by the $^1O_2$ released from the intermediate complex during the UV-activated reaction (Figure 5.11 B). This observation supports the assumption of existence of the intermediate complex of **S1** and $^1O_2$.

In order to analyse the extent of the $^1O_2$ release during the UV activation and substantiate the effect of TEMP in the UV-activated reaction, the fluorescence response of the intermediate complex was examined in the presence of TEMP. A sample solution of 10 µM of **S1** and 5 µM of RB in DMF was irradiated with the Xenon lamp for 30 min. Then 5 mM of TEMP was added to the solution containing the intermediate complex and the fluorescence spectra was recorded before and after 3 min of UV activation. The UV-induced fluorescence enhancement was sustained even in the presence of high concentration of TEMP (Figure 5.12 A). However, there is a slight decrease in the overall fluorescence enhancement factor triggered by 3 min of UV illumination in the presence of TEMP (8-fold enhancement) which is when compared to the control experiment conducted without TEMP (11-fold enhancement) as shown in the Figure 5.12 B. This result is comparable that in the presence of NaN_3 (Figure 5.4).

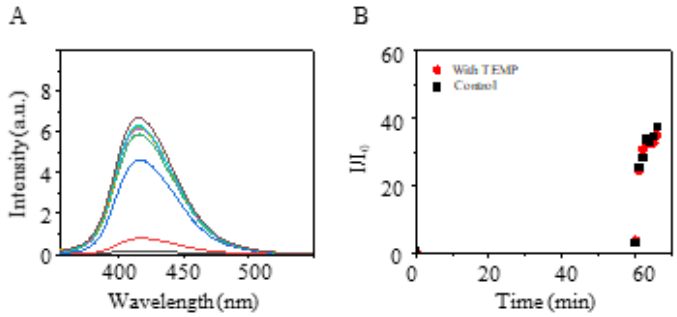

Figure 5.12. (A) Fluorescence spectra of a solution of **S1** (10 µM) and RB (2:1 molar ratio) in DMF before and after the photosensitization (λ=532 nm, 50 mW cm^{-2}) for 30 min, then the $^1O_2$ trap, TEMP (5 mM) was added and photoactivated with UV (365 nm, 1 $mWcm^{-2}$) B) Time-traced relative fluorescence intensities (at λ=420 nm): the red traces represents the fluorescence response of the sample solution containing TEMP and the black traces correspond to the control experiment conducted without TEMP.

From EPR and fluorescence spectroscopic studies, it is possible to propose the existence of the intermediate complex between **S1** and $^1O_2$ and the surplus energy supplied by UV light activates this complex to produce the endoperoxide. During the activated reaction, a portion of $^1O_2$ is released out of the complex which was captured by TEMP to produce TEMPO. The information regarding the existence and the activated reaction of the intermediate complex was obtained from the EPR studies. However, the characterization of the intermediate complex needs additional experiments.

5.7 NMR studies of the UV-activated reaction of S1

NMR spectroscopy is widely employed to characterize organic compounds. With the help of NMR spectroscopy, it is possible to extract the information regarding covalent and non-covalent interaction between organic molecules.[16] Therefore, I applied NMR spectroscopy to study the formation of the intermediate complex between $^1O_2$ and **S1**, and its activated reaction under UV light. Generally, the NMR signals of the endoperoxides shows different features compared to the staring material. During the cycloaddition of the dienophile, $^1O_2$ the anthracene undergoes drastic changes. The unsaturated C=C bonds are replaced by the newly formed C-O σ bonds. This change leads to the loss of aromaticity and the anthracene ring loses the planarity. Therefore, the NMR signals of endoperoxide should be different from the parent anthracene.[7]

In order to study the UV-activated reaction of **S1** using NMR spectroscopy, I made a solution of **S1** (3 mM) and RB (150 μM) in DMF-d7. Heptane (2 mM) was added as an internal reference to assist the analysis of the change in the signals during photo-illumination. The NMR spectrum of the sample solution was recorded prior to the irradiation. The sample solution was taken in a quartz cell having 0.1 mm path length and irradiated with the Xenon lamp fitted with a 480 nm long-pass filter (166 mW cm^{-2} at 560 nm) for the photosensitized generation of $^1O_2$ by RB. The NMR spectra of the sample is measured every 90 min photoirradiation interval. After 180 min of photosensitization the solution was illuminated with UV light (300-400 nm band pass filter; 118 mW cm^{-2} at 365 nm). After UV irradiation for 5 min, NMR spectrum was recorded.

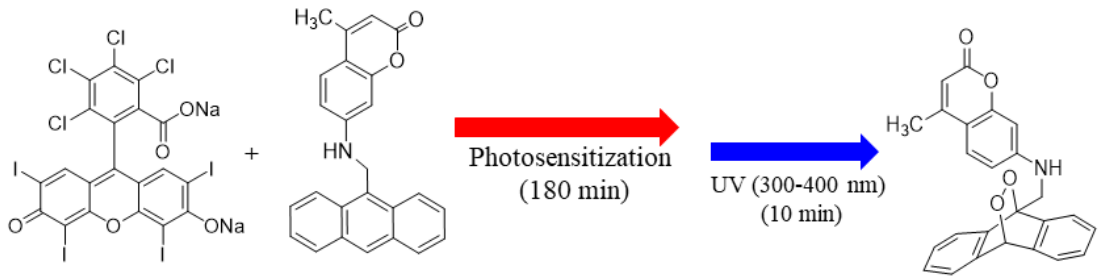

Figure 5.13. A scheme of UV-activated reaction of a complex between **S1** and $^1O_2$.

The NMR spectra of **S1** before and after photo illumination is shown in Figure 5.14. After 90 min of illumination ca. 25 new signals are produced. By considering the number of non-equivalent protons (11), apparently two new species are formed. The accurate assignments of the peaks are very difficult due to the unresolved peaks which are appeared together. The peaks of heptane (m, δ: 1.27-1.31 and m, δ: 0.86-0.89) were considered as references and all the other peaks were integrated according to this reference peaks.

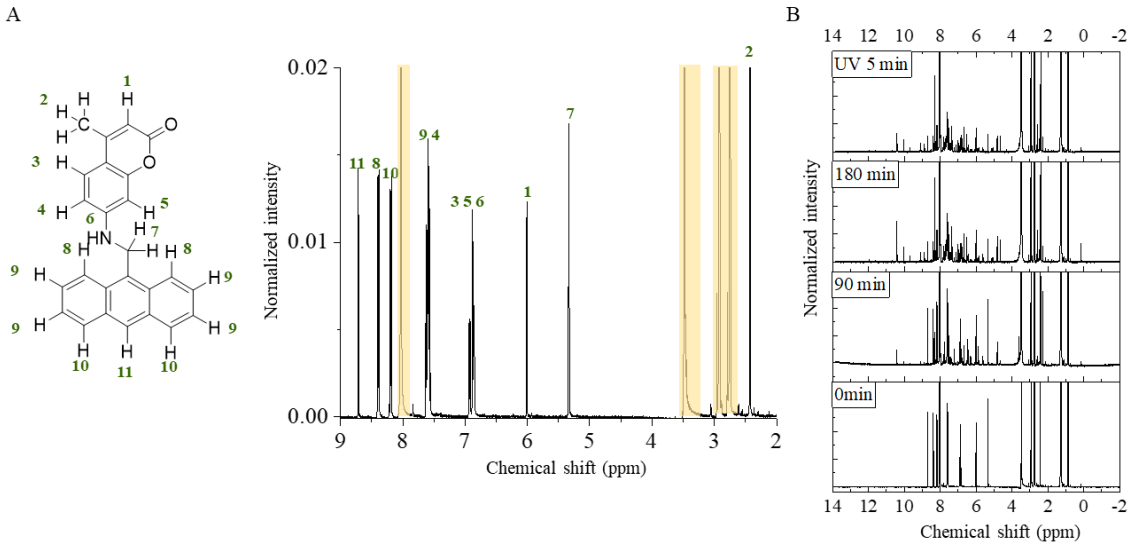

Figure 5.14. (A) The structure and NMR spectrum of **S1** with peak assignments. (B) The combined NMR spectra of the sample solution containing **S1** (3 mM) and RB (150 µM) Heptane (2 mM) in DMF-d7 taken at different time interval of photoirradiation under xenon lamp fitted with 480 nm long-pass filter (166 mWcm^{-2} at 560 nm for 90 min and 10 min) and 300-400 nm band-pass filter for 5 min (118 mW cm^{-2} at 365 nm).

Interestingly, a set of signals were weakened over the time under photosensitization. Besides, another set of peaks were enhanced with time. The overall NMR spectra were complicated to be resolved. Therefore, for the convenience, I picked the NMR peaks with significant intensities, which were changing over the time. The selected area NMR signals collected at different time intervals of photosensitization and UV illumination are stacked in Figure 5.15. I analyzed the changing pattern of the signals and interpreted that there were two new species coexisting in the sample. One of the species was degrading and another was increasing with the time under photosensitization. I assigned the set of signals which were fading to the intermediate complex between $^1O_2$ and **S1**. The other set of enhancing peaks were assigned to endoperoxide of **S1**.

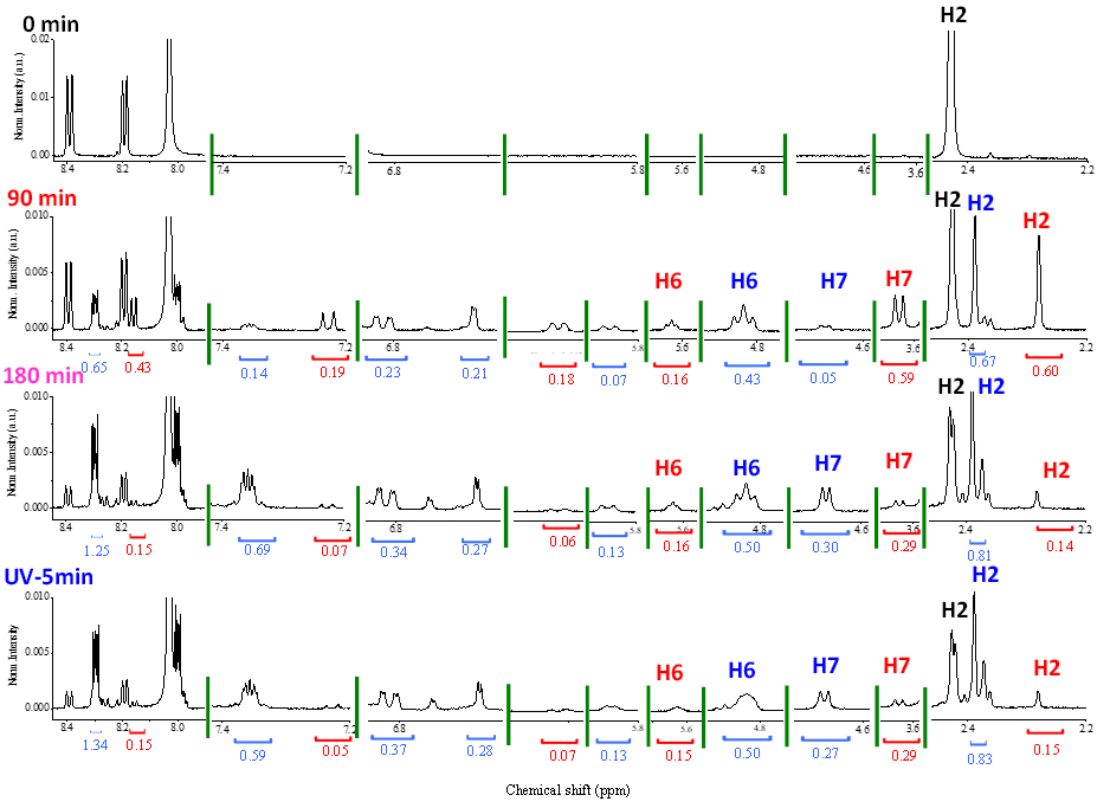

Figure 5.15. The selected area NMR spectra of a mixture of **S1** and RB taken at different time interval of photoirradiation. The blue letter represents the peaks corresponding to the endoperoxide and the red letter represents the peaks corresponding to the intermediate complex. To avoid possible confusion, only charecteristic signals are indicated in this figure.

Since UV stimulates the intermediate complex to undergo activated reaction, I expected that during the UV illumination there will be a sudden and intense change in the signals. To assign the peaks to the corresponding protons, I considered the a few characteristic peaks such as the proton at N-H (H6), N-CH_2 (H7), CH_3 (H2) which are appreciably resolved in the NMR spectra (Figure 5.15). There are two new sets of peaks. One set was decreasing with time, which corresponds to the intermediate complex and other was increasing with time, which corresponds to the endoperoxide. The change in the peaks of proton of coumarin suggests the inevitable participation of the coumarin substituent in the UV activated reaction in **S1** to form the endoperoxide of **S1** at tremendously high rate.

Thus, the NMR data gives a better idea about the UV-activated reaction. During the photosensitization of RB, the $^1O_2$ generated reacts with **S1.** A portion of the $^1O_2$ reacts with **S1** and produces the endoperoxide. On the other hand, a portion of **S1** traps $^1O_2$ to form the intermediate complex. During UV illumination, the intermediate completely reacts to form the endoperoxide. Therefore, the intensity of the NMR signals from the intermediate complex decreased with the time under UV illumination and the intensity of the signals corresponding to the endoperoxide increased simultaneously. Unfortunately, contrary to my expectation of sudden and remarkable change to the intensities of signals, I noticed only a minor change.

5.8 Mechanism of UV-activated reaction of S1 and singlet oxygen

Here, I propose a hypothetical mechanism to rationalise the UV-induced activated reaction of **S1** and $^1O_2$. In order to explain this process, the reported mechanism of 4+2 cycloaddition of anthracenes and $^1O_2$ is needed to be considered. The low energy π^* LUMO of $^1O_2$ makes it an excellent electrophile. $^1O_2$ can efficiently undergo pericyclic reactions with unsaturated organic compounds, specifically cycloaddition reactions with acenes in a concerted or stepwise pathway. In literatures, anthracene derivatives are reported to follow any of these mechanisms. In the single step concerted mechanism, $^1O_2$ addition to the aromatic ring proceeds through a reversible formation of an exciplex in singlet excited state having substantial charge transfer from organic donor to oxygen. The partial formation new bonds can occur in this transition state in which if both the bonds are formed to the equivalent extent in a synchronous way otherwise, new bonds are

formed to a different extent through an asynchronous mode. In the stepwise pathway, at first $^1O_2$ forms a single bond with one of the carbon atoms in the anthracene and afterward the second bond is established to produce the endoperoxide (Figure 5.16). The center ring of the anthracenes are more reactive to take part in the cycloaddition reactions.[17-24]

However, in the present case, **S1** is more unlikely to follow stepwise mechanism as because from the fluorescence studies, I verified that the intermediate complex is in *fluorescence off* state. In the stepwise mechanism, the intermediate state has the anthracene bonded to $^1O_2$ causing the disruption of the aromaticity of the central ring. However, in case of **S1** the anthracene ring is optically intact in the intermediate complex otherwise the deformation of anthracene ring would have caused blockage of PET with coumarin and the complex would be in a *fluorescence on* state which is not happening in this study. Therefore, the stepwise mechanism can be dismissed.

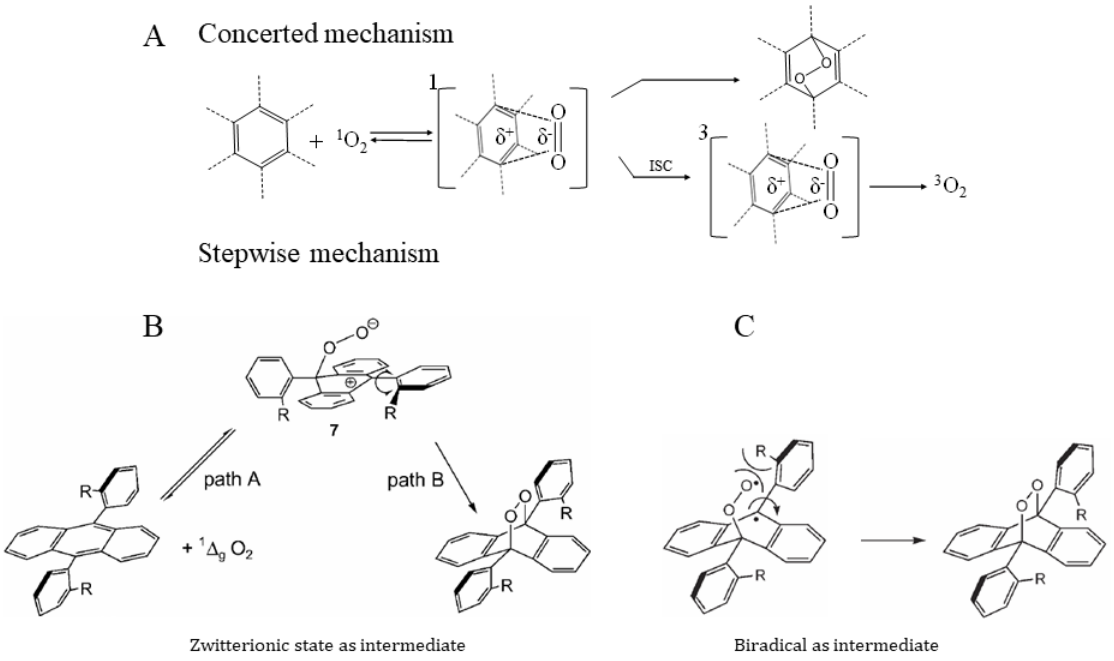

Figure 5.16. The proposed Mechanism of [4+2] cycloaddition of $^1O_2$ to aromatic compounds in (A) Concerted pathway (Ref 21) (B) and (C) stepwise mechanism involving a zwitterionic intermediate (Ref 22) or a biradical intermediate respectively (Ref 23).

While considering the concerted pathway, the intermediate form a partial bond with both the carbon atom in the anthracene ring and this readily rearranges to give the product. The unusually high stability of the intermediate complex of **S1** and $^1O_2$ is a unique observation. The intermediate persisted for 24h under dark and undergoes a rapid change under UV illumination to elicit enhanced fluorescence by blocking PET between anthracene and coumarin. The coumarin substituent has a vital role in this activated reaction which was previously verified by changing the substitution on anthracene.

The mechanism of UV activated reaction can be explained using the hypothetical mechanism shown in Scheme 5.1. The $^1O_2$ generated by the photosensitization of RB reacts with the **S1** to form endoperoxide. Although a large portion of the $^1O_2$ reacting with the molecular sensor, **S1** gets trapped between the coumarin substituent and anthracene part to form an intermediate complex. There is a probable noncovalent interaction of $^1O_2$ with both the coumarin and anthracene which is evident from the NMR studies. When the intermediate is exposed to UV light the complex receives surplus amount of energy which leads to release of the $^1O_2$ from the intermediate. The UV induced photolysis of anthracene endoperoxides and $^1O_2$ release is already reported.[24] However, in the present case, the anthracene in **S1** captures the $^1O_2$ released from complex with a high affinity to undergo activated reaction to produce the endoperoxide which is responsible for the enormous enhancement in the fluorescence. However, some fraction of $^1O_2$ gets released outside which was detected in the EPR studies. The UV activated reaction helps to improve the efficiency of the sensor and leads to ultrafast detection of $^1O_2$. Furthermore, the usage of UV as the external stimuli, it is possible to achieve the temporal control over the sensing activity making time-delayed sensing possible. In other words, the detection can be verified even long time after photodynamic action, making sensor **S1** as an efficient sensor for future applications.

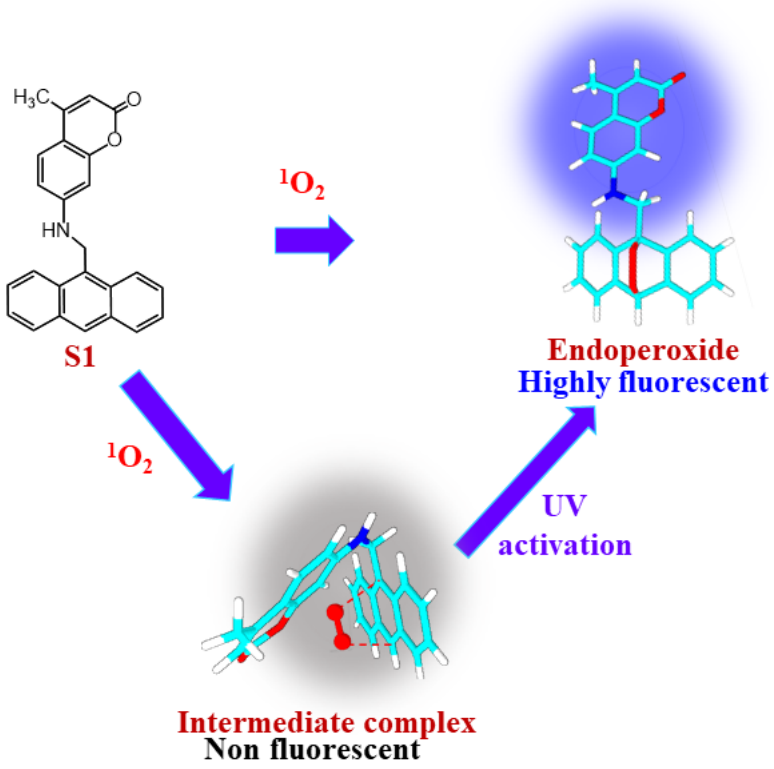

Scheme 5.1: Schematic representation of UV activated reaction of **S1** leading to enhanced fluorescence and enhancement in $^1O_2$ sensing efficiency.

5.9 The application of singlet oxygen sensors

One of the important applications of the $^1O_2$ fluorescence sensors comprises in vitro detection of $^1O_2$ during photodynamic therapy in cancer cell, to which only a limited number of cell permeable sensors are reported. Among the cell permeable sensors, xanthene-based sensors undergo self-sensitization, limiting its reliability.[25] The Si-Rhodamine-anthracene conjugate, is a stable sensor but its synthesis is complex.[2] Recently, Sun et al. reported a Rhodamine 6G-anthracene conjugate (**S3**) for intracellular $^1O_2$ detection. However, the organelle specific intracellular localization of **S3** is unknown.[6] Generally, Rhodamine-based cationic dyes target the matrix side of the inner mitochondrial membrane.[2]

In this study, I investigated the organelle specific localization of **S3** in Hela cell and demonstrated its ability to sense endogenous $^1O_2$, specifically in mitochondria. To this purpose Hela cells were incubated with 200 nM of **S3** solution in Hank's balanced

salt solution (HBSS buffer) at room temperature for 10 min. The cell imaging was carried out using Nikon confocal system (A1Rsi) with Nikon inverted microscope (Ti-E). The sensor was excited with a 487 nm laser and the images were collected. In order to know the organelle specific localization of **S3**, the cells were counter-stained with Mitotracker deep red (excited with 636 nm laser) and colocalization was examined.

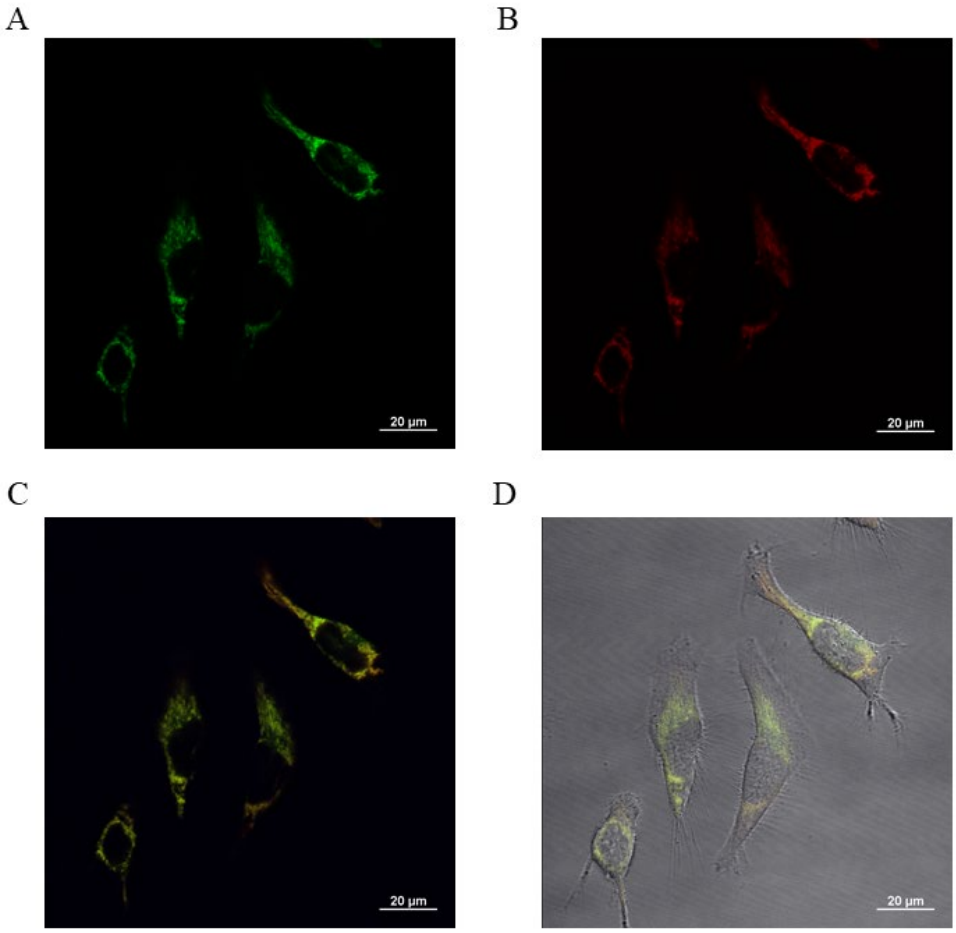

Figure 5.17. Hela cells stained with (A) 200 nM of **S3 (**B) 50 nM of Mitotracker deep red. (C) overlay image under counterstaining. (D) overlay and bright-field images.

The dual-color confocal microscopy images provide information regarding the degree of colocalization of the two fluorophores. In the present study, the Mander's colocalization coefficient for extent of colocalization of **S3** and Mitotracker deep red was found at 0.88±0.01 referring to very high mitochondrial targetability of **S3**.[25] By considering the mitochondrial localization of **S3**, the cells incubated with 200 nM of **S3**

were irradiated with 402 nm laser in order to excite the intracellular photosensitizers like porphyrin and heme which are located in the mitochondria. The fluorescence response of **S3** was recorded as the function of time under laser excitation. The increase in the fluorescence response suggests the intracellular $^1O_2$ sensing. Therefore, I verified that **S3** is an efficient probe for the detection of intracellular $^1O_2$.

5.10 Conclusions

The $^1O_2$ sensing efficiency of **S1** was improved by supplying additional energy by low-intensity UV light after the photosensitization. The UV-induced enhancement in fluorescence is attributed to the activated reaction of the intermediate complex between $^1O_2$ and **S1**. The intermediate complex showed stability against $^1O_2$ scavenger and persisted for several hours. The substituent effect on the UV-activated reaction was examined by changing the substituent on the 9-position of anthracene with Rhodamine 6G (**S3**), and I interpret the role of coumarin in the activated reaction. The role of the amine proton in the 7-amino-4-methyl coumarin substituent was ruled out by assessing the UV effect in N-alkylated coumarin-anthracene conjugate (**S2**). The release of a fraction of $^1O_2$ from the intermediate complex during UV-activated was detected duing the EPR study. The EPR study strengthened the assumption of a long-lived intermediate state in which $^1O_2$ is trapped in **S1**. NMR studies were conducted to characterize the intermediate complex formed during the reaction of $^1O_2$ and **S1**. The intermediate state exhibited different chemical shift compared to the endoperoxide and pristine **S1**. The mechanism of the UV-activated reaction is explained in terms of the formation of the intermediate complex between $^1O_2$ and **S1**. The intermediate complex undergoes activated reaction under UV light. The UV-activated reaction increases the sensitivity of **S1** and decreases the sensing time. In parallel, intracellular $^1O_2$ sensing was demonstrated using **S3**. The organelle specific localization of **S3** was verified by colocalization with a counter fluorophore. The colocalization of **S3** with Mitotracker deep red in Hela cell verified the mitochondrion specificity of **S3** which efficiently detects endogenous $^1O_2$.

References

1. Tanaka, K.; Miura, T.; Umezawa, N.; Urano, Y.; Kikuchi, K.; Higuchi, T.; Nagano, T. Rational Design of Fluorescein-Based Fluorescence Probes. Mechanism-Based Design of a Maximum Fluorescence Probe for $^1O_2$. *J. Am. Chem. Soc.* **2001**, *123* (11), 2530–2536.
2. Kim, S.; Tachikawa, T.; Fujitsuka, M.; Majima, T. Far-Red Fluorescence Probe for Monitoring $^1O_2$ during Photodynamic Therapy. *J. Am. Chem. Soc.* **2014**, *136* (33), 11707–11715.
3. Flors, C.; Fryer, M. J.; Waring, J.; Reeder, B.; Bechtold, U.; Mullineaux, P. M.; Nonell, S.; Wilson, M. T.; Baker, N. R. Imaging the Production of $^1O_2$ in Vivo Using a New Fluorescent Sensor, 1O2 Sensor Green®. *J. Exp. Bot.* **2006**, *57* (8), 1725–1734.
4. Pedersen, S. K.; Holmehave, J.; Blaikie, F. H.; Gollmer, A.; Breitenbach, T.; Jensen, H. H.; Ogilby, P. R. Aarhus Sensor Green: A Fluorescent Probe for$^1O_2$. *J. Org. Chem.* **2014**, *79* (7), 3079–3087.
5. Kohara, R.; Yuyama, K.; Shigeri, Y.; Biju, V. Cover Picture: Blue-Emitting Electron-Donor/Acceptor Dyads for Naked-Eye Fluorescence Detection of $^1O_2$. *ChemPhotoChem.* **2017**, *1* (7), 297–297.
6. Sun, M.; Krishnakumar, S.; Zhang, Y.; Liang, D.; Yang, X.; Wong, M. W.; Wang, S.; Huang, D. $^1O_2$ Probes Made Simple: Anthracenylmethyl Substituted Fluorophores as Reaction-Based Probes for Detection and Imaging of Cellular $^1O_2$. *Sensors Actuators, B Chem.* **2018**.
7. Fidder, H.; Lauer, A.; Freyer, W.; Koeppe, B.; Heyne, K. Photochemistry of Anthracene-9, 10-Endoperoxide. **2009**, 6289–6296.
8. Bouas-Laurent, H.; Castellan, A.; Desvergne, J. P.; Lapouyade, R. Photodimerization of Anthracenes in Fluid Solutions: (Part 2) Mechanistic Aspects of the Photocycloaddition and of the Photochemical and Thermal Cleavage. *Chem. Soc. Rev.* **2001**, *30* (4), 248–263.
9. Li, M. Y.; Cline, C. S.; Koker, E. B.; Carmichael, H. H.; Chignell, C. F.; Bilski, P. Quenching of Singlet Molecular Oxygen ($^1O_2$) by Azide Anion in Solvent Mixtures. *Photochem. Photobiol.* **2001**, *74* (6), 760.

10. Curran, D. P.; Heffner, T. A.; Jeong, K. S.; Rebek, J. New Chiral Auxiliaries for Thermal Cycloadditions. *J. Am. Chem. Soc.* **1989**, *111* (26), 9238–9240.
11. Turro, N. J.; Chow, M. F.; Rigaudy, J. Thermolysis of Anthracene Endoperoxides. Concerted vs. Diradicai Mechanisms. Microscopic Reversibility in Endothermic Chemiluminescent Reactions. *J. Am. Chem. Soc.* **1979**, *101* (5), 1300–1302.
12. Fudickar, W.; Linker, T. Release of $^1O_2$ from Organic Peroxides under Mild Conditions. *ChemPhotoChem* **2018**, *2* (7), 548–558.
13. Adam, W.; Prein, M. Communications to the Editor: Diastereoselective [4 + 2] Cycloaddition of $^1O_2$ in the Photooxygenation of Chiral Naphthyl Alcohols: Evidence for a Hydroxy Group-Directing Effect. *J. Am. Chem. Soc.* **1993**, *115* (9), 3766–3767.
14. Vorst, A. V.; Lion, Y. Indirect E P R Evidence for the Production of 1O2 in the Photosensitization of Nucleic Acid Constituents by Proflavine. *Notizen*, **1976**, 32 (3-4), 203-204.
15. Roessler, M. M.; Salvadori, E. Principles and Applications of EPR Spectroscopy in the Chemical Sciences. *Chem. Soc. Rev.* **2018**, *47* (8), 2534–2553.
16. Mazzei, P.; Piccolo, A. Quantitative Evaluation of Noncovalent Interactions between Glyphosate and Dissolved Humic Substances by NMR Spectroscopy. *Environ. Sci. Technol.* **2012**, *46* (11), 5939–5946.
17. Chien, S. H.; Cheng, M. F.; Lau, K. C.; Li, W. K. Theoretical Study of the Diels-Alder Reactions between Singlet ($^1\Delta_g$) Oxygen and Acenes. *J. Phys. Chem. A* **2005**, *109* (33), 7509–7518.
18. Reddy, A. R.; Bendikov, M. Diels-Alder Reaction of Acenes with Singlet and Triplet Oxygen - Theoretical Study of Two-State Reactivity. *Chem. Commun.* **2006**, No. 11, 1179–1181.
19. Leach, A. G.; Houk, K. N. Diels-Alder and Ene Reactions of 1O2, Nitroso Compounds and Triazolinediones: Transition States and Mechanisms from Contemporary Theory. *Chem. Commun.* **2002**, *2* (12), 1243–1255.
20. Bobrowski, M.; Liwo, A.; Ołdziej, S.; Jeziorek, D.; Ossowski, T. CAS MCSCF/CAS MCQDPT2 Study of the Mechanism of Singlet: Oxygen Addition

to 1,3-Butadiene and Benzene. *J. Am. Chem. Soc.* **2000**, *122* (34), 8112–8119.

21. Aubry, J. M.; Pierlot, C.; Rigaudy, J.; Schmidt, R. Reversible Binding of Oxygen to Aromatic Compounds. *Acc. Chem. Res.* **2003**, *36* (9), 668–675.
22. Zehm, D.; Fudickar, W.; Hans, M.; Schilde, U.; Kelling, A.; Linker, T. 9,10-Diarylanthracenes as Molecular Switches: Syntheses, Properties, Isomerisations and Their Reactions with $^1O_2$. *Chem. Eur. J.* **2008**, *14* (36), 11429–11441.
23. Zehm, D.; Fudickar, W.; Linker, T. Molecular Switches Flipped by Oxygen. *Angew. Chemie. Int. Ed.* **2007**, *46* (40), 7689–7692.
24. Schmidt, R.; Schaffner, K.; Trost, W.; Brauer, H. D. Wavelength-Dependent and Dual Photochemistry of the Endoperoxides of Anthracene and 9,10-Dimethylanthracene. *J. Phys. Chem.* **1984**, *88* (5), 956–958.
25. Manders, E.M.M.; Verbeek, F.J.; Aten, J.A. Measurement of co-localization of objects in dual-colour confocal images. *J. Microsc.* **1993**, 169 (3), 375-382.

Summary and perspectives

Photoinduced electron transfer (PET) is an extensively investigated and explored phenomenon in the field of chemistry and biology. By considering the contribution of electron transfer systems in natural photosynthesis, diverse artificial molecular systems have been developed and utilized for solar energy harnessing. The applications of electron transfer are not limited to solar harvesters only but also enables the construction of eminent PET-based biosensors. I developed two classes of electron D-A dyads with high electron transfer efficiency; one is applied to photothermal energy conversion, and the other to $^1O_2$ sensing applications. In chapter 1, I summarize photoinduced electron transfer occurring in natural photosynthesis and its efficient mimicking toward the construction of various artificial solar energy harvesting systems. In this chapter, I explain the classical theories of electron transfer in the designing of simple D-A dyads with efficient intramolecular electron transfer. In chapter 2, I discuss the synthesis of novel D-A systems, methods of characterization of D-A systems, and spectroscopic methods employed in the investigation of electron transfer and photothermal and sensing studies.

In chapter 3, I focused on the design and synthesis of acridinium-based electron D-A dyads with highly efficient electron transfer and demonstrated its photothermal effect (PTE). 9-position substituted acridinium based D-A dyad with the phenolic OH group (**Acr1**) exhibited pH-dependent PTE. **Acr1** efficiently absorbs light in the UV to blue wavelength region. The photoexcitation of **Acr1** resulted in fast PET and subsequent deprotonation to form the betaine structure (**Acr1-betaine**) which absorbs the light in the UV-Vis-NIR region. The generation of betaine intermediate was verified by the transient absorption studies. The photothermal conversion efficiency of **Acr1** was estimated at 43 % with blue laser illumination, and the illumination with longer wavelength light improved the PTE. **Acr1** showed excellent photostability. Therefore, I confirmed that **Acr1** can be used as an efficient photothermal generator under white light illumination with high photostability. In the future, the light harnessing property of such systems can be improved by the construction of an interconnected array of electron D-A systems to form multiple betaines.

In chapter 4, I studied the kinetics of $^1O_2$ sensing by anthracene-based electron D-A dyads. I examined the $^1O_2$ sensing efficiency of three sensors, aminocoumarin-anthracene conjugates (**S1** and **S2**), and the Rhodamine 6G-anthracene conjugate (**S3**), and the model compound, 9-methylanthracene. The rates of the [4+2] cycloaddition reaction between $^1O_2$ and the molecular sensors were determined with the aid of fluorescence spectroscopy and absorption spectroscopy. The second order rate of the oxidation of three sensors found to be an order of magnitude less than the model 9-methylanthracene. I hypothesize that the reduced reactivity is due to the steric effect of the bulky substituents or the truncated reactivity of the intermediate complex.

In chapter 5, I extensively studied the mechanism of $^1O_2$ sensing by **S1** and rationalize the reduced sensing efficiency of **S1**. I found that UV illumination subsequent to the photosensitization of a sample solution of **S1** and RB show enormous fluorescence enhancement within 30 s. I hypothesize the existence of a less reactive intermediate complex which undergoes activated reaction under UV illumination. The intermediate persisted for several hours and showed significant stability towards $^1O_2$ scavengers. The role of coumarin substituent on the UV-activated reaction was confirmed by synthesizing a Rhodamine 6G-bases sensor (**S3**). The role of the amine proton in coumarin in trapping $^1O_2$ was ruled by studying the UV-activated reaction of N-alkylated sensor (**S2**). The mechanism of UV-activated reaction was studied with the aid of EPR spectroscopy and NMR spectroscopy. The results in this chapter guided me to assume that $^1O_2$ reacts with **S1** to form a mixture of endoperoxide and an intermediate complex between $^1O_2$ and **S1**. By UV light illumination, the complex undergoes activated reaction to produce the endoperoxide at a higher rate, which is responsible for the enormous enhancement in the fluorescence. Thus, the UV-activated reaction helped me to improve the efficiency and speed of $^1O_2$ sensing. Finally, I demonstrated the organelle-specific intracellular localization and endogenous $^1O_2$ sensing using **S3** in Hela cell. In the future, such dyads can be promising for two-photon assisted photodynamic therapy provided the trapped $^1O_2$ can be released by controlling the structure of the D-A systems. Furthermore, by the careful selection of the substituent, it will be possible to construct NIR absorbing molecules for efficient $^1O_2$ delivery under one-photon excitation.

List of publications

1. Kinetics of singlet oxygen sensing using 9-substituted anthracene derivatives

Devika Sasikumar, Reiko Kohara, Yuta Takano, Ken-ichi Yuyama, Vasudevanpillai Biju

Journal of Chemical Science, **2019**, *131*, 1.

2. Photoinduced Betaine Generation for the Efficient Photothermal Energy Conversion

Devika Sasikumar, Yuta Takano, Vasudevanpillai Biju

Chemistry A European Journal, **2020**, *26*, 9.

List of Presentations

1. Kinetic Studies of Singlet Oxygen Sensing using a Coumarin Conjugated Anthracene and 9-Methylanthracene (Poster).
   Devika Sasikumar, Ken-ichi Yuyama, Yuta Takano, Vasudevanpillai Biju
   19th RIES-HOKUDAI International Symposium, 2018 (**First prize**).
2. Steady-state Spectroscopic Studies of the Kinetics of Singlet Oxygen Sensing by 9-Substituted Anthracene Derivatives (Oral presentation).
   Devika Sasikumar, Yuta Takano, Ken-ichi Yuyama, Vasudevanpillai Biju
   99th CSJ Annual Meeting, 2019.
3. Photosensitized generation of singlet oxygen by Rose Bengal and its reaction with 9-substituted Anthracene (Poster).
   Devika Sasikumar, Ken-ichi Yuyama, Yuta Takano, Vasudevanpillai Biju
   Toukiken, Chemical-based Science Association Hokkaido branch Winter research recital and presentation, 2019.
4. Activated reaction of singlet oxygen trapped in an electron donor-acceptor system (Oral presentation).
   Devika Sasikumar, Reiko Kohara, Ken-ichi Yuyama, Yuta Takano, Vasudevanpillai Biju

   Kakiken, Chemical-based Science Association Hokkaido branch summer research recital and presentation, 2019.

5. Activated reaction of singlet oxygen trapped in an electron donor-acceptor system (Poster).
   Devika Sasikumar, Yuta Takano, Morihiko Hamada, Ken-ichi Yuyama, Yasuhiro Kobori, Vasudevanpillai Biju
   The Japanese Photochemistry Association Annual Meeting, 2019.
6. Photoinduced Betaine Generation for Efficient Photothermal Energy Conversion (Poster).
   Devika Sasikumar, Yuta Takano, Vasudevanpillai Biju
   20th RIES-HOKUDAI International Symposium, 2019.

7. Acridinium-Based Electron Donor- Acceptor Dyad for Efficient Photothermal Energy Conversion (Poster).
   Devika Sasikumar, Yuta Takano, Vasudevanpillai Biju
   2019 International Symposium of RIES-CEFMS.